PHYSICS-BASED GROUND MOTION SIMULATION OF THE 2020 SAMOS EARTHQUAKE

A THESIS SUBMITTED TO
THE GRADUATE SCHOOL OF NATURAL AND APPLIED SCIENCES
OF
MIDDLE EAST TECHNICAL UNIVERSITY

BY

YİĞİT URHAN

IN PARTIAL FULFILLMENT OF THE REQUIREMENTS
FOR
THE DEGREE OF MASTER OF SCIENCE
IN
CIVIL ENGINEERING

SEPTEMBER 2022

Approval of the thesis:

PHYSICS-BASED GROUND MOTION SIMULATION OF THE 2020 SAMOS EARTHQUAKE

submitted by **YİĞİT URHAN** in partial fulfillment of the requirements for the degree of **Master of Science in Civil Engineering Department, Middle East Technical University** by,

Prof. Dr. Halil Kalıpçılar
Dean, Graduate School of **Natural and Applied Sciences** _____

Prof. Dr. Erdem Canbay
Head of Department, **Civil Engineering** _____

Prof. Dr. Ayşegül Askan Gündoğan
Supervisor, **Civil Engineering, METU** _____

Examining Committee Members:

Prof. Dr. Murat Altuğ Erberik
Civil Engineering, METU _____

Prof. Dr. Ayşegül Askan Gündoğan
Civil Engineering, METU _____

Assoc. Prof. Dr. Gülüm Tanırcan
Earthquake Engineering, Boğaziçi University _____

Assist. Prof. Dr. Karin Şeşetyan
Earthquake Engineering, Boğaziçi University _____

Assoc. Prof. Dr. Mustafa Kerem Koçkar
Civil Engineering, Hacettepe University _____

Date: 02.09.2022

I hereby declare that all information in this document has been obtained and presented in accordance with academic rules and ethical conduct. I also declare that, as required by these rules and conduct, I have fully cited and referenced all material and results that are not original to this work.

Name, Surname: Yiğit Urhan

Signature :

ABSTRACT

PHYSICS-BASED GROUND MOTION SIMULATION OF THE 2020 SAMOS EARTHQUAKE

Urhan, Yiğit
M.S., Department of Civil Engineering
Supervisor: Prof. Dr. Ayşegül Askan Gündoğan

September 2022, 118 pages

In this thesis, low-frequency ground motions of the 2020 Samos Earthquake at selected ground motion stations are simulated using the spectral element method. For this purpose, rigorous mathematical derivation of the classical wave equation is presented first. Next, the spatiotemporal discretisation scheme involved in finite element and spectral element methods are derived. Then, a velocity model is constructed based on the velocity profiles provided by AFAD. For the source model, moment tensor solution of the Samos Earthquake is utilised with a Gaussian source time function, since the event is located at far distances from the studied stations admitting point source model. Finally, comparison of synthetic records with the observed data is presented and then station-wise comparison of ground motion parameters is made.

Keywords: spectral element method, finite element method, physics-based, deterministic, ground motion simulations, elastic wave propagation

ÖZ

2020 SAMOS DEPREMİ YER HAREKETİNİN FİZİK TABANLI BENZEŞTİRİLMESİ

Urhan, Yiğit
Yüksek Lisans, İnşaat Mühendisliği Bölümü
Tez Yöneticisi: Prof. Dr. Ayşegül Askan Gündoğan

Eylül 2022 , 118 sayfa

Bu tez kapsamında, 2020 Samos Depremi'nin yaratmış olduğu düşük frekanslı yer hareketleri, bölgede seçilen istasyonlar üzerinde spektral eleman yöntemi kullanılarak benzeştirilmiştir. Bunun için, ilk adımda dalga denkleminin detaylı matematiksel türetimi gösterilmiş, bir sonraki adımda ise elde edilen dalga denkleminin sonlu eleman ve spektral eleman metodlarıyla uzay-zamansal olarak ayrıştırılması sunulmuştur. Ardından, AFAD üzerinden elde edilen verilerle bölgeye ait bir dalga hız profili üretilmiştir. Kaynak modeli için, depremin seçilen istasyonlardan uzaklığı göz önüne alınarak nokta kaynak modeli uygulanmış olup, Samos Depremi'ne ait sismik moment tensör çözümü ile Gauss kaynak-zaman fonksiyonu kullanılmıştır. Son olarak, üretilen sentetik kayıtlarla gözlenmiş verilerin kıyaslaması, belirli istasyonlar için sunulmuş ve seçilen her bir istasyon için yer hareketi parametreleri kıyaslanmıştır.

Anahtar Kelimeler: spektral eleman yöntemi, sonlu eleman yöntemi, fizik-tabanlı, deterministik, yer hareketi benzeşimleri, elastik dalga yayılımı

To my late grandfather

Burhan Urhan

ACKNOWLEDGMENTS

I would like to express my deepest gratitude to my thesis advisor Prof. Dr. Ayşegül Askan Gündoğan, who is the most productive and hardworking person I have ever met in my life, for her boundless trust and faith in me and the extraordinary freedom she has granted me throughout my thesis study. Despite her extreme workload, she has always been available and never stopped providing regular guidance.

I would like to thank the examining comitee members Prof. Dr. Murat Altuğ Erberik, Assoc. Prof. Dr. Gülüm Tanırcan, Assoc. Prof. Dr. Mustafa Kerem Koçkar, and Assist. Prof. Dr. Karin Şeşetyan for their constructive criticism, interest, help, and patience during my thesis defense.

I would like to thank Assoc. Prof. Dr. Serdar Göktepe, without whom I would have never been able to build the foundation of computational mechanics that I now have, for his continuous support, invaluable comments, and, most importantly, for his time in academic discussions we had.

I would also like to thank my very close friend Mehmet Türkezer, for his support and concern during difficult days and our everlasting friendship. Despite studying in different branches of civil engineering, the scientific discussions we had significantly contributed to my knowledge on soil mechanics.

I am very grateful to my mother Adviye Urhan for her endless support and tremendous effort to help me work comfortably and for unconditional love. I am also highly thankful to my father Mustafa Urhan and my uncle Ercan Urhan for their priceless moral support and unconditional love and trust.

Finally, I would particularly like to thank my brother Tan Altar Urhan, for always being by my side and always being able to cheer me up. His passion and absolute dedication to music inspired me every time I felt down and helped me a lot to motivate myself. Without him, the thesis writing process would have been very distressing.

TABLE OF CONTENTS

LIST OF TABLES

TABLES

LIST OF FIGURES

FIGURES

CHAPTER 1

INTRODUCTION

1.1 General

Among catastrophic disasters, earthquakes comprise the most devastating ones that have left cataclysmic impacts on many civilizations throughout history. The Great Lisbon earthquake of 1755 constitutes a prominent example of such an event considering its influence on eminent philosophers of the enlightenment era and the development of modern seismology [1]. Immanuel Kant [2], a central figure in the European Enlightenment whose comprehensive works on various philosophical topics made him one of the most influential philosophers, attempted to describe the driving mechanism of earthquakes systematically. Although his explanations are not legitimate, it would not be inaccurate to regard his work as the beginning of modern seismology. Considering Kant's work on the Great Lisbon earthquake of 1755 as the breakthrough event in the development of contemporary seismology, the chronological evolution of the science of seismology is concisely presented by Ben-Menahem [3] describing proceedings of 1755's aftermath.

Given the tectonic setting of Turkey, a historical perspective of major earthquakes also immediately shows the severity of the situation in Turkey. A decade after the 1755 Lisbon earthquake, a severe earthquake shook Istanbul in 1766 that even caused a tsunami, killed thousands of people, and damaged terrifically the city [4]. The Great Erzincan earthquake of 1939, and the Golcuk earthquake, followed by the Duzce earthquake of 1999, are tragic incidents that occurred in the last few decades. In this regard, considering the potential of severe destruction, a comprehensive study of earthquakes requiring interdisciplinary collaboration is necessary to understand their

nature better and develop systematic approaches to mitigate the adverse effects caused by earthquakes.

Fortunately, with the immense contributions of a myriad of scientists, many of whose contributions are honored in [3], the nature and the causes of earthquakes are now better understood. In addition, thanks to advancements in computer technology and computer science providing numerous novel algorithms, simulations of earthquakes in a computer environment are possible, enabling engineers and scientists to perform scenario earthquakes leading to a robust, systematized approach, so-called the ground motion simulation methodology.

Although the incorporation of heterogeneity and anisotropy in the classical wave theory is possible, this requires intensive efforts to handle complex geometries composed of different materials, which is often the case in geodynamic problems. Henceforth, this necessitates the ground motion simulation studies providing numerical solutions in favor of an analytic solution. The ground motion simulation methodology involves an accurate representation of the topography, source mechanism, and seismic parameters of a region under interest. Then, with the employment of numerical solution techniques, a representative solution is obtained for that region. In achieving this, ground motion simulation approaches are divided into three groups, namely deterministic methods, stochastic methods, and hybrid methods. In this thesis, deterministic ground motion simulation methods will be followed.

1.2 Historical Development of Classical Wave Theory

Deterministic methodologies rely upon the numerical solution to the classical wave equation. Therefore, it would be wise first to give a brief, concise historical review of the development of classical wave theory to gain insight into the intrinsic properties of wave motion. In [5], a neat study of the history of classical wave theory may be found along with the translated version of original papers contributing to the wave theory. Table 1.1 depicts the chronological progress made by numerous scientists respectively. Nevertheless, it would be enlightening to briefly mention the first attempts in describing the motion made by Aristotle and then Galileo's remarkable contribu-

tion to the perception of motion that radically changed the study of mechanics. The classical wave equation is essentially the consequence of the law of conservation of linear momentum stemming from the translation symmetry, or as given in [6], homogeneity of space. The concept of conservation of linear momentum dates back to Aristotle, who erroneously relates an object's velocity with the applied force on it. He did not consider friction as a force and hence drew the wrong conclusion regarding the motion. An interested reader may like to delve into [7] for the mathematical formulation of Aristotle's Law of Motion and its consequences. After Aristotle, Galileo made a breakthrough in the history of classical mechanics with his works on falling bodies that laid the foundation of classical mechanics and put an end to the Aristotelian view of motion by correcting Aristotle's Law of Motion [8]. He concluded that all bodies fall from the same height at equal times, an implicit statement of the principle of inertia that would be known later as Newton's first law of motion. Of course, Table 1.1 includes only scientists central to the development of the classical wave theory. For a more comprehensive historical background, the masterwork of A.E.H Love [9] is strongly recommended to the interested reader. Further, his astonishing piece [10] regarding geodynamics covers the wave propagation problem on a planetary scale. In addition, for the mathematical developments accompanying the classical wave theory, the reader may refer to [11].

1.3 Literature Review on Deterministic Methods

Deterministic methodologies in ground motion simulation studies often cover various numerical solution schemes in solving the wave equation unless the problem under consideration permits an analytical solution. In rather simple geometries, where spatial and material heterogeneities are not too much involved, an analytical solution to the wave equation is also possible. In the case of elasticity, the wave equation can be readily solved analytically if the source is rather simple. In cases where the source involves complexities, an integral formulation might be obtained, maintaining the analyticity of the solution. [12], [13], [14] provides a rigorous mathematical treatment of the subject, including the geometrical ray theory permitting an analytical solution to the wave equation in vertically heterogeneous domains. However, most of the

Table 1.1: Contributions to the development of classical elastic wave theory. Table is adapted from [5]

Year	Contributor	Major contribution in this volume
1678	Robert Hooke 1635–1703	Hooke derived the equations of motion for a spring and relations between stress and strain for a linear elastic solid, forming the underpinning of the theory of wave propagation. **Hooke's law.**
1827	Claude L. M. H. Navier 1785–1836	Navier extended the work of Hooke to deal with elastic bodies, expressing the equations of vibrational motion in terms of displacements and Poisson's elastic parameters. **Navier equation.**
1828	Augustin-Louis Cauchy 1789–1857	Cauchy expanded on the properties of both elastic and nonelastic bodies, expressing wave propagation in terms of stress and strain, thus generalizing Hooke's law. **Cauchy equation of motion.**
1839	George Green 1793–1841	Prior to Green, the elastic wave theory was represented in terms of the interaction of individual molecules. By introducing the notion of the strain energy function, Green fundamentally changed representation of the theory and permitted the generalization of existing concepts of wave propagation to the anisotropic case (the prior molecular descriptions held only for isotropic media). In so doing, Green correctly predicted the existence of the 21 independent elastic constants (Cauchy's previous formulation permitted only 15). **Strain-energy function.**
1845	George G. Stokes 1819–1903	Stokes expanded on the work of Poisson to show that P-waves were purely compressional and that S-waves were purely rotational and determined their velocities in terms of elastic constants. Stokes also developed the equations for fluid motion, giving rise to the **Navier-Stokes equations**.
1855	William Thomson, Lord Kelvin 1824–1907	Kelvin made the connection between thermodynamics and elastic wave propagation, relating the conversion of mechanical to thermal energy. He also determined the relations between strain and heat flow. **Thermoelasticity.**
1877	Elwin B. Christoffel 1829–1900	Christoffel characterized propagation of the wave surface in anisotropic media. Starting from his work on shock fronts in liquids, he extended those analyses to elastic media. **Christoffel equation.**

Table 1.1 (Cont'd): Contributions to the development of classical elastic wave theory. Table is adapted from [5].

Year	Contributor	Major contribution in this volume
1678	Robert Hooke 1635–1703	Hooke derived the equations of motion for a spring and relations between stress and strain for a linear elastic solid, forming the underpinning of the theory of wave propagation. **Hooke's law.**
1827	Claude L. M. H. Navier 1785–1836	Navier extended the work of Hooke to deal with elastic bodies, expressing the equations of vibrational motion in terms of displacements and Poisson's elastic parameters. **Navier equation.**
1828	Augustin-Louis Cauchy 1789–1857	Cauchy expanded on the properties of both elastic and nonelastic bodies, expressing wave propagation in terms of stress and strain, thus generalizing Hooke's law. **Cauchy equation of motion.**
1839	George Green 1793–1841	Prior to Green, the elastic wave theory was represented in terms of the interaction of individual molecules. By introducing the notion of the strain energy function, Green fundamentally changed representation of the theory and permitted the generalization of existing concepts of wave propagation to the anisotropic case (the prior molecular descriptions held only for isotropic media). In so doing, Green correctly predicted the existence of the 21 independent elastic constants (Cauchy's previous formulation permitted only 15). **Strain-energy function.**
1845	George G. Stokes 1819–1903	Stokes expanded on the work of Poisson to show that P-waves were purely compressional and that S-waves were purely rotational and determined their velocities in terms of elastic constants. Stokes also developed the equations for fluid motion, giving rise to the **Navier-Stokes equations**.
1855	William Thomson, Lord Kelvin 1824–1907	Kelvin made the connection between thermodynamics and elastic wave propagation, relating the conversion of mechanical to thermal energy. He also determined the relations between strain and heat flow. **Thermoelasticity.**
1877	Elwin B. Christoffel 1829–1900	Christoffel characterized propagation of the wave surface in anisotropic media. Starting from his work on shock fronts in liquids, he extended those analyses to elastic media. **Christoffel equation.**

time, such simplistic cases are not realistic, and hence numerical solutions are often performed. The Finite Difference Time-Domain Method (FDTDM), Discrete Wave Number Method (DWNM), Theoretical Green's Function Method (DGFM), Finite Element Method (FEM), Spectral Element Method (SEM), and Boundary Element Method (BEM) are primary methodologies followed in wave propagation literature. FDTDM, FEM, SEM, and BEM are based on the spatiotemporal discretization of the classical wave equation. In FDTDM, the strong form of the wave equation discretized both spatially and temporally employing a finite-difference scheme (e.g., Furumura and Chen [15], Moczo et al. [16], Moczo et al. [17], Moczo et al. [18], Moczo, Kristek, and Halada [19], Frankel and Vidale [20], Frankel [21], Yomogida and Etgen [22], Aochi and Dupros [23], Aochi, Durand, and Douglas [24], Virieux [25], Oprsal and Zahradnik [26], Sato, Graves, and Somerville, [27], Aoi et al. [28], Aoi and Fujiwara [29], Graves [30], Tanırcan [31], Şeşetyan [32]). Unlike FDTDM, in FEM (e.g., Bielak, Ghattas, and Kim [33], Etienne et al. [34], Li et al. [35], Toshinawa and Ohmachi, [36], Bao et al. [37], Moczo et al. [38]) and SEM (Cohen, Joly, and Tordjman [39], Priolo, Carcione, and Seriani [40], Seriani and Priolo [41], Komatitsch and Vilotte [42], Komatitsch and Tromp [43], Komatitsch and Tromp [44], Komatitsch, Coutel, and Mora [45], , Komatitsch et al. [46], Komatitsch et al. [47], Komatitsch, Barnes, and Tromp [48], Michéa and Komatitsch [49], Di Michele et al. [50], Casarotti et al. [51], Chaljub et al. [52]) the weak form of the wave equation is first obtained and then discretized in space by dividing the whole domain of interest into finite subdomains. Then, the resulting semi-discrete form is numerically integrated in time to arrive at an approximate time-domain solution. Although the procedure is identical in both methods, the difference in names originates from the selection of numerical quadrature in approximation to integrals involved and of basis functions. Whilst in BEM (e.g., Kawase [53], Luco, Wong, and De Barros [54], Pedersen, Sánchez-Sesma, and Campillo [55]), only the boundary of the domain is discretized instead. However, BEM requires the knowledge of the fundamental solution to the governing differential equation of the problem under consideration. DWNM (e.g., Bouchon and Aki [56]), TGFM (e.g., Bouchon [57], Hisada [58], Chen and Zhang [59]), and EGFM (e.g., Hartzell [60], Irikura [61]) on the other hand depend upon the construction of Green's functions to achieve a solution superimposing impulse responses.

Most of the applications in Turkey involve empirical and stochastic methods. There is a gap in the literature regarding deterministic strong ground motion simulation studies on Turkey, except for a few studies (Tanırcan [31], Özmen, Karimzadeh and Askan [62], Şahin et al. [63]).

1.4 Objective

The main objective of this thesis is to simulate the low frequency content of the 2020 October Samos earthquake at selected stations located in İzmir. As a first attempt to deterministically model the earthquake, a point source model is simulated with spectral elements used in spatial discretization. An initial 3D velocity model is constructed based on 1D velocity models at the strong ground motion stations in İzmir operated by AFAD.

1.5 Scope of the Thesis

In Chapter 2, the derivation of the classical elastic wave equation is presented. In the first part, mathematical descriptions of motion and deformation are given. In addition, the deformation gradient, a fundamental geometric mapping tool of continuum mechanics, is introduced to develop finite deformation theory from which the small deformation theory for elastic wave equation is derived. In the second part, the derivation of the Cauchy stress theorem is given in detail, followed by the derivation of conservation laws of continuum physics. Furthermore, particular emphasis is made on the consequences of the entropy imbalance in modeling dissipative media. Next, the classical elastic wave equation for an isotropic infinite homogeneous media is derived from the variational principles. Finally, the derivation of the analytical solution to the wave equation is performed in detail.

In Chapter 3, spatiotemporal discretization of the wave equation is presented. In the first step, weak formulation of the wave equation is performed, and then the mathematical description of the Galerkin FEM discretization scheme is given. In the next step, the isoparametric formulation of the discretized elements is performed. Then,

numerical integration schemes, Gauss-Legendre quadrature, and Gauss-Legendre-Lobatto quadrature are described. Finally, temporal discretization of the semi-discrete wave equation via Newmark's β method is performed.

In Chapter 4, numerical simulations of the 2020 Samos earthquake are presented as an application of the spectral element method. In the first part, background information on the event and the study area is highlighted. In the second part, the SPECFEM3D Cartesian Package (https://geodynamics.org) employed in the simulations is introduced, and the main parameters modified within the package are described. In the next step, numerical details of the simulations, along with the incorporated earthquake source and velocity models, are summarized. Finally, strong ground motion characteristics of the 2020 Samos earthquake recordings at selected stations are presented, and a comparison of observed data against numerical results is made at these stations.

In Chapter 5, a summary of the thesis is given first. Then, the main findings of the thesis are presented. Finally, several points that should be further investigated in future studies are proposed.

1.6 Further Reading

For precise development of the theory, the masterwork of Aki and Richards [12] is referred. To compensate the mathematical difficulty, Roach [64], Erdélyi [65], Watanabe [66] by is recommended to reader. Pujol [13] might be a good choice to accompany [12] as well. Another astonishingly comprehensive work might be found in [14] by Ben-Menahem and Singh, investigating almost all aspects of the wave propagation problem analytically. Classics by Achenbach [67] and Rayleigh [68]-[69] are strongly recommended to be able to gain a solid understanding of the physics of vibrating bodies along with Love's masterpiece [9]. To have an intuitive grasp of classical and analytical mechanics, [6], [7], [70], [71], [72] by the great physicists Feynman, Landau, Susskind, and Lanczos is referred. In addition, Helmholtz [73] would be an interesting resource for studying musical vibrations from a mathematical point of view. To comprehend their knowledge further, [74], [75], [76], [77], [78],

[79], and [80] would be suitable than enough to grasp the fundamentals of wave propagation in general, possibly coupled non-linear, setting. In that case, [81], and [82] might be useful to develop an intuition regarding the entropy constituting the second law of thermodynamics and often studied in the development of constitutive theories. For purely axiomatic formulation of the entropy and the second law of thermodynamics [83] is referred. Furthermore, [84] would provide extensive acquaintance of tensor algebra and tensor calculus, fundamental mathematical tools in continuum mechanics. For the generic implementation of FEM, [85], [86], and [87] would provide the reader with the necessary background for further advancement and familiarity with literature. Lastly, to gain a fundamental understanding regarding the general framework of the computational earthquake engineering [88] is referred.

CHAPTER 2

CLASSICAL WAVE THEORY

2.1 Kinematics

In the development of classical wave theory, a precise description of kinematics is needed in the first place to have a solid foundation on which the theory is to be built. In continuum physics, kinematics characterizes how a material body continuously deforms geometrically. By a material body, it is meant that set $\mathscr{B}$ composed of infinitely many material points $\mathcal{P} \in \mathcal{B}$ where $\mathcal{B}$ is the region occupying geometrical positions of three-dimensional Euclidian space $\mathbb{R}^3$. In addition, the configuration of the body $\mathscr{B}$ can be described by bijective mapping $\boldsymbol{\chi}$ such that for a given particular point $\mathcal{P} \in \mathscr{B}$ there is a unique material point in a region $\mathcal{B} \subset \mathbb{R}^3$ occupied by $\mathcal{P}$ at a given time t. That is,

$$\boldsymbol{\chi}_t : \begin{cases} \mathscr{B} \mapsto \mathcal{B}_t \in \mathbb{R}^3 \\ \mathcal{P} \in \mathscr{B} \mapsto \boldsymbol{x}_t = \boldsymbol{\chi}_t(\mathcal{P}) \in \mathcal{B}_t \end{cases} \tag{2.1}$$

where subscript t denotes configurations parametrized by time. Following this definition, the motion of the body $\mathscr{B}$ might be thought of as sequential configurations in space into which $\mathscr{B}$ evolves in time given by the bijective mapping $\boldsymbol{\chi}_t$. This mathematical abstraction of motion provides one with a tool to keep a record of material points $\mathcal{P}$ and allows for an arbitrary choice of reference configuration relative to which a given motion is to be characterized as long as bijectivity is preserved. Armed with the bijective mapping $\boldsymbol{\chi}$ and in the light of the concept of motion set forth, now an accurate prescription to deformation that a continuous body, whether solid or fluid, undergoes can be given. Let us first give a mathematical definition of the reference configuration. If the body $\mathscr{B}$ is identified at time t_0 relative to which the deformation

is to be measured, it is called the reference configuration given by $\boldsymbol{\chi}$,

$$\boldsymbol{\chi}_{t_0} : \begin{cases} \mathscr{B} \mapsto \mathcal{B} \in \mathbb{R}^3 \\ \mathcal{P} \in \mathscr{B} \mapsto \boldsymbol{X} = \boldsymbol{\chi}_{t_0}(\mathcal{P}) \in \mathcal{B} \end{cases} \tag{2.2}$$

where $\boldsymbol{X}$ denotes material coordinates that each material point $\mathcal{P} \in \mathscr{B}$ occupies in the reference body $\mathcal{B}$. In a like manner, the current configuration into which eventually the reference body $\mathcal{B}$ evolves might be defined to completely characterize the motion of $\mathscr{B}$. If the current configuration of $\mathscr{B}$ at time t is denoted as $\mathscr{S} \coloneqq \boldsymbol{\chi}_t$, current coordinates occupied by a material point $\mathcal{P}$ as $\boldsymbol{x}$, (2.1) becomes

$$\boldsymbol{\chi}_t : \begin{cases} \mathscr{B} \mapsto \mathscr{S} \in \mathbb{R}^3 \\ \mathcal{P} \in \mathscr{B} \mapsto \boldsymbol{x} = \boldsymbol{\chi}_t(\mathcal{P}) \in \mathscr{S} \end{cases} \tag{2.3}$$

(2.2), (2.3), enable one to associate each material point $\mathcal{P}$ in a physical body $\mathscr{B} \subset \mathbb{R}^3$ with the reference coordinates $\boldsymbol{X} \in \mathcal{B}$ and the spatial coordinates $\boldsymbol{x} \in \mathscr{S}$, respectively, in both configurations. Hence, the nonlinear deformation map $\boldsymbol{\varphi}_t(\boldsymbol{X}) = \boldsymbol{\varphi}(\boldsymbol{X}, t)$ can be introduced.

$$\boldsymbol{\varphi}_t(\boldsymbol{X}) : \begin{cases} \mathcal{B} \mapsto \mathscr{S} \in \mathbb{R}^3 \\ \boldsymbol{X} \in \mathcal{B} \mapsto \boldsymbol{x} = \boldsymbol{\varphi}_t(\boldsymbol{X}) = \boldsymbol{\chi}_t \circ \boldsymbol{\chi}_{t_0}^{-1}(\boldsymbol{X}) \end{cases} \tag{2.4}$$

to directly relate the reference configuration $\mathcal{B}$ with the spatial configuration $\mathscr{S}$ at a given time $t \in \mathbb{R}^+$. It is essential to notice that one may take advantage of the inherent flexibility of choice of reference configuration due to its arbitrariness. Henceforth, one may select a reference configuration such that $\mathscr{B}$ and $\mathcal{B}$ coincides, making $\boldsymbol{\chi}(\boldsymbol{X}, t) \equiv \boldsymbol{\varphi}(\boldsymbol{X}, t)$ equivalent to each other, and therefore eliminates the additional need for a transformation between reference and current configurations. Nevertheless, the general description set forth will be followed as it would depict a general picture, distinguishing the physical body from a rather abstract notion of configuration space.

Before moving on to kinematic and geometric quantities describing the motion and deformation, it would be useful to briefly remark upon the necessary requirement for bijectivity. Since it is conjectured that the deformation map $\boldsymbol{\varphi}_t(\boldsymbol{X})$ is bijective, it

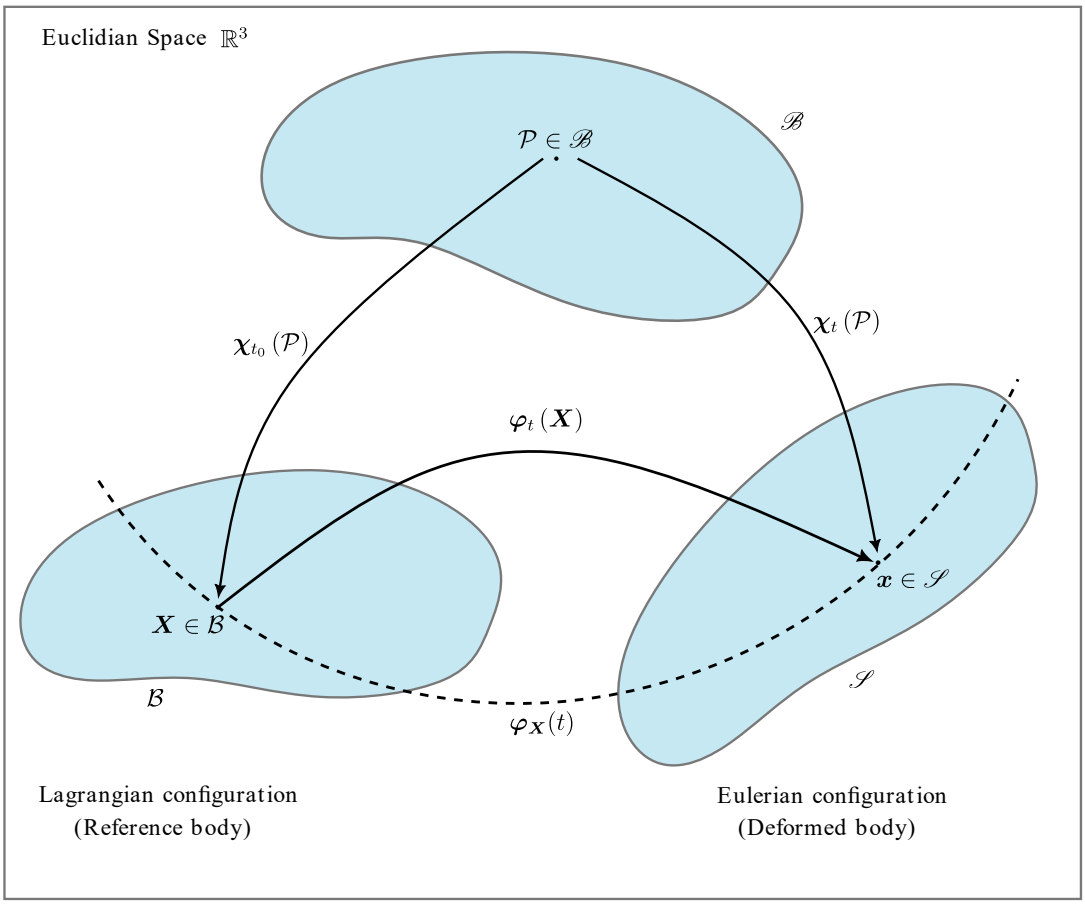

Figure 2.1: Schematic illustration of motion in Euclidian space $\mathbb{R}^3$. Dashed lines represent the path traversed by a material point initially at reference coordinate $\boldsymbol{X}$. Subscript $\boldsymbol{X}$ indicates that $\boldsymbol{\varphi}(\boldsymbol{X}, t)$ continuously maps a fixed material point of body $\mathcal{B}$ to current configuration for each time $t \in \mathbb{R}^+$ expressed by $\boldsymbol{\varphi}_{\boldsymbol{X}}(t)$, whereas subscript t signifies that mapping takes place at a specific time instant t giving the current configuration of the reference body $\mathcal{B}$ given by $\boldsymbol{\varphi}_t(\boldsymbol{X})$.

must, then, as well be inverted, giving the inverse deformation map,

$$\boldsymbol{\varphi}_t^{-1}(\boldsymbol{x}) : \begin{cases} \mathscr{S} \mapsto \mathcal{B} \in \mathbb{R}^3 \\ \boldsymbol{x} \in \mathcal{B} \mapsto \boldsymbol{X} = \boldsymbol{\varphi}_t^{-1}(\boldsymbol{x}) = \boldsymbol{\chi}_{t_0} \circ \boldsymbol{\chi}_t^{-1}(\boldsymbol{x}) \end{cases} \tag{2.5}$$

For such a bijective mapping to exist, the Jacobian of the transformation must be positive-definite.

$$J \coloneqq \det \boldsymbol{\nabla}_{\boldsymbol{X}} \boldsymbol{\varphi}_t(\boldsymbol{X}) > 0 \tag{2.6}$$

The positive-definiteness of the Jacobian ensures that different material points cannot occupy the same spatial point in the current configuration and guarantees the self-impenetrability of the body. The direct consequence of this condition is that a given set of material points possessing the boundary $\partial\mathcal{B}$ of reference body $\mathcal{B}$ convects with the material boundary for all time t, implying that any material point $\mathcal{P} \in \partial\mathcal{B}$ restricted to move along the boundary of the body $\partial\mathscr{S}$ maintaining the configuration $\mathscr{S}$. This leads to the fact that any material point occupying the interior body cannot cross the boundary throughout the motion.

2.1.1 Fundamental Kinematic Quantities Associated with Motion

There are three fundamental fields associated with a given motion that a material body possesses, namely, displacement field, velocity field, and acceleration field. However, the definition of motion introduced in Section 2.1 leads to two different descriptions of a given physical field. The former is called the material, also known as Lagrangian, description, and the latter is called the spatial, or Eulerian, description. In the former, a material particle identified at the position $\boldsymbol{X} \in \mathcal{B}$ in the reference configuration is used to describe a physical field defined on the body, whereas the latter uses the spatial location $\boldsymbol{x} \in \mathscr{S}$ that the material point now occupies in the current configuration describing the same physical field while convecting with the body. Hence, the material velocity and the material acceleration can be defined as

$$\boldsymbol{V}(\boldsymbol{X}, t) \coloneqq \frac{\mathrm{d}\boldsymbol{\varphi}_{\boldsymbol{X}}(t)}{\mathrm{d}t} = \frac{\partial \boldsymbol{\varphi}(\boldsymbol{X}, t)}{\partial t} \tag{2.7}$$

$$\boldsymbol{A}(\boldsymbol{X}, t) \coloneqq \frac{\mathrm{d}\boldsymbol{V}_{\boldsymbol{X}}(t)}{\mathrm{d}t} = \frac{\partial \boldsymbol{V}(\boldsymbol{X}, t)}{\partial t} \tag{2.8}$$

Denoting the quantities that are the spatial counterparts of the material description with lower case letters, the spatial description of velocity and the acceleration are

then given by,

$$\boldsymbol{v}(\boldsymbol{x},t) \coloneqq \boldsymbol{V}\big(\boldsymbol{\varphi}_t^{-1}(\boldsymbol{x}),t\big) = \boldsymbol{V}_t(\boldsymbol{X}) \circ \boldsymbol{\varphi}_t^{-1}(\boldsymbol{x}) \tag{2.9}$$

$$\boldsymbol{a}(\boldsymbol{x},t) \coloneqq \boldsymbol{A}\big(\boldsymbol{\varphi}_t^{-1}(\boldsymbol{x}),t\big) = \boldsymbol{A}_t(\boldsymbol{X}) \circ \boldsymbol{\varphi}_t^{-1}(\boldsymbol{x}) \tag{2.10}$$

Figure 2.1 depicts both descriptions. It is crucial to notice that both descriptions describe the same field but with parameterization of $\boldsymbol{X}$ in the former and with $\boldsymbol{x}$ in the latter. Hence, the presence of two descriptions leads to the question of how to relate the material and the spatial time derivatives of a given physical field, such as the acceleration field given by (2.8), (2.10). This brings out the notion of the material time derivative of a spatial field, the temporal change in a given field experienced by the observer convecting with the body but identified at the position $\boldsymbol{X} \in \mathcal{B}$ in the reference configuration. To give a mathematical definition, let us consider a scalar spatial field

$$f(\boldsymbol{x},t) : \boldsymbol{\varphi_t}(\mathcal{B}) \times \mathbb{R}^+ \mapsto \mathbb{R} \tag{2.11}$$

Then, the material time derivative of $f(\boldsymbol{x},t)$ yields,

$$\dot{f}(\boldsymbol{x},t) = \frac{\partial f(\boldsymbol{x},t)}{\partial t}\Big|_{\boldsymbol{x}} + \boldsymbol{\nabla}_{\boldsymbol{x}} f(\boldsymbol{x},t) \cdot \boldsymbol{v} \tag{2.12}$$

where the first term at the right hand side represents the local temporal change of $f(\boldsymbol{x},t)$ at the current configuration, whereas the second term gives the convective rate of change of $f(\boldsymbol{x},t)$ body experiences during the motion. A consequence of the existence of the material time derivative of spatial field is that one can perform the time derivative operation in the current configuration even without knowing the reference configuration of the material body. Otherwise, one would need to invert the mapping $\boldsymbol{\varphi}(\boldsymbol{X},t)$ to obtain spatial coordinates of the material body to perform ordinary time derivative in the spatial coordinates.

Remark: *In the development of classical wave theory, deformations involved are considered to be small so that the reference and spatial descriptions of associated physical fields coincide. However, to have a profound understanding, it would be beneficial for one to comprehend the definition of motion in this fashion. Moreover, transformations regarding deformations would also be helpful to have a better understanding of isoparametric formulation given in Chapter 3.*

In fact, once the displacement field is known, the velocity and acceleration fields

can be found on the fly by consecutive differentiation with respect to time. By displacement field, it is understood that the relative deformation that a material body undergoes measuring how much distortion the body experiences with respect to the reference configuration. In mathematical terms, if a material point located at $\boldsymbol{X} \in \mathcal{B}$ in the reference configuration is mapped to the coordinate $x = \boldsymbol{\varphi}_t(\boldsymbol{X}) \in \mathscr{S}$ in the current configuration, then the displacement field can be defined as a vector-valued function $\boldsymbol{u}(\boldsymbol{x}, t) : \boldsymbol{\varphi}_t(\mathcal{B}) \times \mathbb{R}^+ \mapsto \mathbb{R}^3$ such that

$$\boldsymbol{u}(\boldsymbol{x}, t) \coloneqq \boldsymbol{x}(\boldsymbol{X}, t) - \boldsymbol{X} \tag{2.13}$$

where the reference coordinate $\boldsymbol{X}$ is fixed and hence independent of time. The displacement field is closely related to the fundamental geometric map deformation gradient, already given by (2.6), $\boldsymbol{F}(\boldsymbol{X}, t) \coloneqq \boldsymbol{\nabla}_{\boldsymbol{X}} \boldsymbol{\varphi}_t(\boldsymbol{X})$. To understand the meaning of the deformation gradient $\boldsymbol{F}(\boldsymbol{X}, t)$, it might be convenient first to examine the homogeneous deformation case in which the deformation gradient tensor is constant. That means all material points in a given material deform in the same way. Mathematically, if a vector $\boldsymbol{Z} = \boldsymbol{Y} - \boldsymbol{X}$ identified in the reference configuration deforms into its spatial counterpart $\boldsymbol{z} = \boldsymbol{\varphi}_t(\boldsymbol{Y}) - \boldsymbol{\varphi}_t(\boldsymbol{X})$, the following equality holds.

$$\boldsymbol{F} \underbrace{(\boldsymbol{Y} - \boldsymbol{X})}_{\boldsymbol{Z}} = \underbrace{\boldsymbol{\varphi}_t(\boldsymbol{Y}) - \boldsymbol{\varphi}_t(\boldsymbol{X})}_{\text{spatial vector } \boldsymbol{z}} \tag{2.14}$$

Pure and simple shear deformations are immediate examples of such deformations. Now, let us generalize the homogeneous deformation concept so that an arbitrary deformation can as well be represented by $\boldsymbol{F}(\boldsymbol{X}, t)$. Suppose a material point $\boldsymbol{X} + \Delta\boldsymbol{X}$ is located in the small neighborhood of material point $\boldsymbol{X}$. Then, mapping both material coordinates via $\boldsymbol{\varphi}_t$ would give,

$$\boldsymbol{X} \longmapsto \boldsymbol{\varphi}_t(\boldsymbol{X}) \qquad \text{and} \qquad \boldsymbol{X} + \Delta\boldsymbol{X} \longmapsto \boldsymbol{\varphi}_t(\boldsymbol{X} + \Delta\boldsymbol{X}) \tag{2.15}$$

The spatial vector constructed by the expression $\boldsymbol{\varphi}_t(\boldsymbol{X} + \Delta\boldsymbol{X}) - \boldsymbol{\varphi}_t(\boldsymbol{X})$ can be recast

into Gatéaux differential as $o(\|\Delta \boldsymbol{X}\|) \to 0$, yielding

$$\begin{aligned}\underbrace{\boldsymbol{\varphi}_t(\boldsymbol{X}+\Delta\boldsymbol{X})-\boldsymbol{\varphi}_t(\boldsymbol{X})}_{\text{spatial vector } \boldsymbol{z}} &= \frac{\mathrm{d}}{\mathrm{d}\epsilon}[\boldsymbol{\varphi}_t(\boldsymbol{X}+\epsilon\Delta\boldsymbol{X})]\Big|_{\epsilon=0} \\ &= \frac{\mathrm{d}}{\mathrm{d}\epsilon}\big[\boldsymbol{\varphi}_t(\boldsymbol{X})+\epsilon\boldsymbol{\nabla}_{\boldsymbol{X}}\boldsymbol{\varphi}_t(\boldsymbol{X})\Delta\boldsymbol{X}+o\big(\epsilon^2\big)\big]\Big|_{\epsilon=0} \\ &= \boldsymbol{\nabla}_{\boldsymbol{X}}\boldsymbol{\varphi}_t(\boldsymbol{X})\cdot\Delta\boldsymbol{X} \\ &= \underbrace{\boldsymbol{\nabla}_{\boldsymbol{X}}\boldsymbol{\varphi}_t(\boldsymbol{X})}_{\boldsymbol{F}}\cdot\underbrace{(\boldsymbol{X}+\Delta\boldsymbol{X}-\boldsymbol{X})}_{\boldsymbol{Z}} \end{aligned} \tag{2.16}$$

The interpretation of (2.16) is critical to realize the connection between a homogeneous and an arbitrary deformation. It follows that an arbitrary deformation is locally homogeneous that maps material vectors to spatial vectors in a point-wise manner. To make this interpretation (Figure 2.2), let us assume a material body and let $\boldsymbol{\chi}_{t_0}(\vartheta)$ and $\boldsymbol{\chi}_t(\vartheta)$ be material and spatial curves parameterized by $\vartheta \in \mathbb{R}$ on $\mathcal{B}$ and $\mathscr{S}$ respectively. Then, the tangent vector to the material curve drawn at $\boldsymbol{X} = \boldsymbol{\chi}_{t_0}(\vartheta)$ is mapped onto spatial configuration, denoting the material tangent vector $\boldsymbol{T}$ and the spatial counterpart $\boldsymbol{t}$, as follows.

$$\begin{aligned}\boldsymbol{t} = \frac{\mathrm{d}\boldsymbol{\chi}_t(\vartheta)}{\mathrm{d}\vartheta} = \frac{\mathrm{d}\boldsymbol{\varphi_t}\circ\boldsymbol{\chi}_{t_0}(\vartheta)}{\mathrm{d}\vartheta} &= \frac{\partial\boldsymbol{\varphi}_t}{\partial\boldsymbol{\chi}_{t_0}}\cdot\frac{\mathrm{d}\boldsymbol{\chi}_{t_0}}{\mathrm{d}\vartheta}\Big|_{\boldsymbol{X}=\boldsymbol{\chi}_{t_0}(\vartheta)} \\ &= \underbrace{\boldsymbol{\nabla}_{\boldsymbol{X}}\boldsymbol{\varphi}_t(\boldsymbol{X})}_{\boldsymbol{F}}\cdot\boldsymbol{T}\end{aligned} \tag{2.17}$$

Then, by (2.17), a general definition to deformation gradient $\boldsymbol{F}(\boldsymbol{X},t)$ might be given.

$$\boldsymbol{F}(\boldsymbol{X},t):\begin{cases} T_X\mathcal{B} \longmapsto T_x\mathscr{S} \\ \boldsymbol{T} \longmapsto \boldsymbol{t} = \boldsymbol{F}\cdot\boldsymbol{T}\end{cases} \tag{2.18}$$

where $T_X\mathcal{B}$ is the material tangent space $T_x\mathscr{S}$ is the spatial tangent space.

Having obtained the deformation gradient $\boldsymbol{F}(\boldsymbol{X},t)$ which would serve as a mean to represent an arbitrary deformation that a material body possibly undergoes, the deformation measures, namely stretch and strain tensors, can be introduced. Since, in general, a given displacement field is not uniform, these deformation measures represent the local displacement intensity at a given point relative to the reference configuration. Let us first introduce the stretch, the ratio of the distorted local tangent vector $\boldsymbol{dx}$ in the spatial configuration to the length of the material counterpart $\boldsymbol{dX}$.

$$\frac{\|\,\boldsymbol{dx}\,\|}{\|\boldsymbol{dX}\|} = \frac{\sqrt{\boldsymbol{dx}\,\cdot\,\boldsymbol{dx}}}{\sqrt{\boldsymbol{dX}\cdot\boldsymbol{dX}}} \tag{2.19}$$

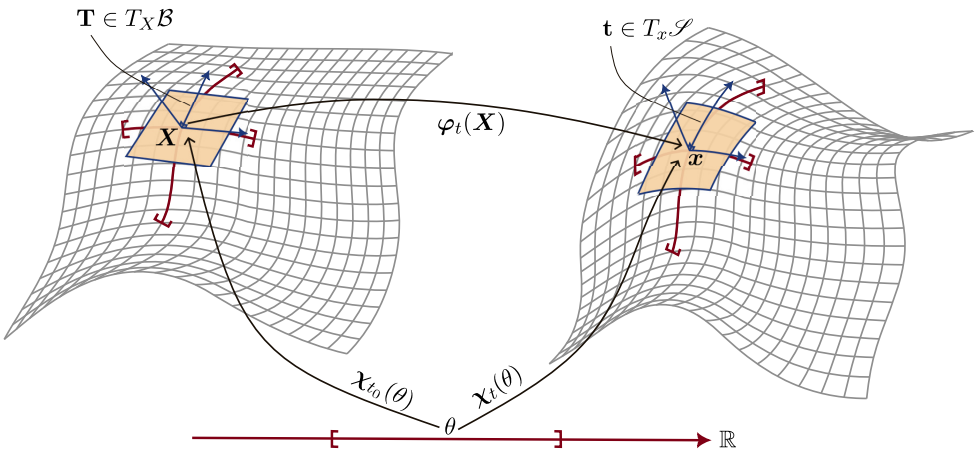

Figure 2.2: Schematic illustration of fundamental geometric mappings, namely the tangent map and the normal map as a measure of deformation.

Inserting (2.17) into (2.19) and selecting the length of the reference vector as unity, i.e., $\|\boldsymbol{dX}\| = 1$,

$$\begin{aligned}\sqrt{\boldsymbol{dx} \cdot \boldsymbol{dx}} &= \sqrt{\boldsymbol{F}\boldsymbol{dX} \cdot \boldsymbol{F}\boldsymbol{dX}} \\ &= \sqrt{\boldsymbol{dX} \cdot \boldsymbol{F}^T\boldsymbol{F}\boldsymbol{dX}} \\ &= \sqrt{\boldsymbol{dX} \cdot \boldsymbol{C}\boldsymbol{dX}}\end{aligned} \tag{2.20}$$

where $\boldsymbol{C} := \boldsymbol{F}^T\boldsymbol{F}$ is the right Cauchy-Green tensor, measuring the stretch in terms of material coordinates. The spatial counterpart of the right Cauchy-Green tensor is the left Cauchy-Green tensor that computes the stretch in terms of spatial coordinates by selecting $\|\boldsymbol{dx}\| = 1$. However, in small deformation theory, these two measures coincide; therefore, an explicit definition will not be given. The right Cauchy-Green tensor allows us to compare the squared lengths of the two tangent vectors additively, which is very handy in small deformation theory when the ratio of two vectors is too close to unity. Let us choose a local material vector having unit length $\|\boldsymbol{dX}\| = 1$. Then,

$$\begin{aligned}\boldsymbol{dx} \cdot \boldsymbol{dx} - \boldsymbol{dX} \cdot \boldsymbol{dX} &= \boldsymbol{F}\boldsymbol{dX} \cdot \boldsymbol{F}\boldsymbol{dX} - \boldsymbol{dX} \cdot \boldsymbol{dX} \\ &= \boldsymbol{dX} \cdot \boldsymbol{F}^T\boldsymbol{F}\boldsymbol{dX} - \boldsymbol{dX} \cdot \boldsymbol{dX} \\ &= \boldsymbol{dX} \cdot \left(\boldsymbol{F}^T\boldsymbol{F} - \mathbf{1}\right) \cdot \boldsymbol{dX} \\ &= \boldsymbol{dX} \cdot 2\boldsymbol{E} \cdot \boldsymbol{dX}\end{aligned} \tag{2.21}$$

where the Green-Lagrange Strain Tensor $\boldsymbol{E}$ is defined as

$$\boldsymbol{E} \coloneqq \frac{1}{2}\big(\boldsymbol{F}^T\boldsymbol{F} - \mathbf{1}\big) = \frac{1}{2}(\boldsymbol{C} - \mathbf{1}) \tag{2.22}$$

The factor of two in (2.21) is due to the symmetry of the tensor $\boldsymbol{F}^T\boldsymbol{F} - \mathbf{1}$. Since the stretch is being measured, there is no contribution coming from rigid body rotation, which is the skew-symmetric part of the tensor $\boldsymbol{F}^T\boldsymbol{F} - \mathbf{1}$. However, since it is already symmetric, the skew-symmetric part vanishes identically. Consequently, all contribution comes from the symmetric part giving the factor of two.

$$\begin{aligned}\mathrm{sym}\big(\boldsymbol{F}^T\boldsymbol{F} - \mathbf{1}\big) &= \frac{1}{2}\Big[\big(\boldsymbol{F}^T\boldsymbol{F} - \mathbf{1}\big) + \big(\boldsymbol{F}^T\boldsymbol{F} - \mathbf{1}\big)^T\Big] \\ &= \boldsymbol{E} + \boldsymbol{E}^T = 2\boldsymbol{E}\end{aligned} \tag{2.23}$$

The Green-Lagrange Strain Tensor can be rewritten in terms of the displacement field, taking the gradient of (2.13) with respect to material coordinates.

$$\boldsymbol{\nabla u} = \boldsymbol{\nabla}_{\boldsymbol{X}}\boldsymbol{\varphi}_t(\boldsymbol{X}) - \mathbf{1} = \boldsymbol{F} - \mathbf{1} \tag{2.24}$$

Inserting into (2.22), the Green-Lagrange Strain Tensor can be recast into the following form.

$$\begin{aligned}\boldsymbol{E} &= \frac{1}{2}\Big[(\boldsymbol{\nabla u} + \mathbf{1})^T(\boldsymbol{\nabla u} + \mathbf{1}) - \mathbf{1}\Big] \\ &= \frac{1}{2}\big[\boldsymbol{\nabla u} + \boldsymbol{\nabla u}^T + \boldsymbol{\nabla u}^T\boldsymbol{\nabla u}\big]\end{aligned} \tag{2.25}$$

In the case of small deformations, i.e., $\|\boldsymbol{\nabla u}\| \ll 1$, the last term in (2.25) becomes negligible, and the Green-Lagrange Strain tensor reduces to the infinitesimal strain tensor $\boldsymbol{\varepsilon}$ often used in the geometrically linear theory of solid mechanics. To demonstrate this, the Green-Lagrange Strain Tensor might be linearized about the reference configuration.

$$\boldsymbol{\varepsilon} \coloneqq \mathrm{sym}(\boldsymbol{\nabla u}) = \mathrm{Lin}\boldsymbol{E}\Big|_{\boldsymbol{F}=\mathbf{1}} = \tilde{\boldsymbol{E}} + (\boldsymbol{F} - \mathbf{1}) : \frac{\partial \boldsymbol{E}}{\partial \boldsymbol{F}}\Big|_{\boldsymbol{F}=\mathbf{1}} \tag{2.26}$$

Introducing the indicial notation and recognizing that $\tilde{\boldsymbol{E}} \coloneqq \boldsymbol{E}(\boldsymbol{F} = \mathbf{1}) = \mathbf{0}$, (2.26)

is computed as

$$\begin{aligned}
\varepsilon_{ij} &= (F_{ij} - \delta_{ij})\frac{\partial E_{ij}}{\partial F_{pq}} \\
&= \frac{1}{2}[F_{ij}\delta_{kp}\delta_{iq}F_{kj} + F_{ij}F_{ki}\delta_{kp}\delta_{jq} - \delta_{ij}\delta_{kp}\delta_{iq}F_{kj} - \delta_{ij}F_{ki}\delta_{kp}\delta_{jq}] \\
&= \frac{1}{2}[F_{ij}\delta_{kp}\delta_{iq}\delta_{kj} + F_{ij}\delta_{ki}\delta_{kp}\delta_{jq} - \delta_{ij}\delta_{kp}\delta_{iq}\delta_{kj} - \delta_{ij}\delta_{ki}\delta_{kp}\delta_{jq}] \\
&= \frac{1}{2}[F_{qp} + F_{pq} - \delta_{qp} - \delta_{pq}] \\
&= \frac{1}{2}\big[\boldsymbol{F}^T - \mathbf{1} + \boldsymbol{F} - \mathbf{1}\big] \\
&= \text{sym}(\boldsymbol{\nabla u})
\end{aligned} \tag{2.27}$$

yielding the small strain tensor $\boldsymbol{\varepsilon}$ which completes the proof. To complete the discussion, transformations of an infinitesimal volume and an area element on a given material body will be shown. Let us start from volume transformation and let dV and dv denote infinitesimal volume elements constructed by the scalar triple product of local tangent vectors

$$\boldsymbol{dX}_{i=1,2,3} \in T_X\mathcal{B} \qquad \text{and} \qquad \boldsymbol{dx}_{i=1,2,3} \in T_x\mathscr{S} \tag{2.28}$$

where the scalar triple products of these vectors are defined as

$$dV \coloneqq \boldsymbol{dX}_1 \cdot (\boldsymbol{dX}_2 \times \boldsymbol{dX}_3) \qquad \text{and} \qquad dv \coloneqq \boldsymbol{dx}_1 \cdot (\boldsymbol{dx}_2 \times \boldsymbol{dx}_3) \tag{2.29}$$

Incorporating the deformation gradient in the latter

$$\begin{aligned}
dv &= \boldsymbol{F}\boldsymbol{dX}_1 \cdot (\boldsymbol{F}\boldsymbol{dX}_2 \times \boldsymbol{F}\boldsymbol{dX}_3) \\
&= \det(\boldsymbol{F})\, \boldsymbol{dX}_1 \cdot (\boldsymbol{dX}_2 \times \boldsymbol{dX}_3) \\
&= \det(\boldsymbol{F})dV
\end{aligned} \tag{2.30}$$

where we already introduced the Jacobian $J \coloneqq \det \boldsymbol{\nabla}_{\boldsymbol{X}}\boldsymbol{\varphi}_t(\boldsymbol{X}) = \det(\boldsymbol{F})$. Hence, recalling the restriction on the value of J, the volume transformation can be defined as follows.

$$J : \begin{cases} \mathbb{R}^+ \longmapsto \mathbb{R}^+ \\ dV \longmapsto dv = \det(\boldsymbol{F})dV \end{cases} \tag{2.31}$$

In a similar manner, let dA and da denote infinitesimal area elements defined by the reference and spatial area normals

$$\boldsymbol{N}dA \coloneqq \boldsymbol{dX}_2 \times \boldsymbol{dX}_3 \qquad \text{and} \qquad \boldsymbol{n}da \coloneqq \boldsymbol{dx}_2 \times \boldsymbol{dx}_3 \tag{2.32}$$

Then, inserting (2.32) into (2.29) would yield

$$\begin{aligned} \boldsymbol{dx}_1 \cdot \boldsymbol{n} da &= \boldsymbol{F} \boldsymbol{dX}_1 \cdot \boldsymbol{n} da \\ &= \boldsymbol{dX}_1 \cdot \boldsymbol{F}^T \boldsymbol{n} da = J \boldsymbol{dX}_1 \cdot \boldsymbol{N} dA \end{aligned} \tag{2.33}$$

Using the latter equality, we get

$$\boldsymbol{dX}_1 \cdot \left[\boldsymbol{F}^T \boldsymbol{n} da - J \boldsymbol{N} dA \right] = 0 \tag{2.34}$$

for arbitrary $\boldsymbol{dX}_1$. Consequently the area transformation relation can be found by solving (2.34) for $\boldsymbol{n}da$

$$\boldsymbol{n} da = J \boldsymbol{F}^{-T} \boldsymbol{N} dA \tag{2.35}$$

where $J\boldsymbol{F}^{-T}$ maps area normal $\boldsymbol{N}$ in the reference configuration on to the spatial counterpart $\boldsymbol{n}$. Taking the norm of both sides would then give the areal Jacobian

$$da = \jmath \, dA \quad \text{where } \jmath \coloneqq J \| \boldsymbol{F}^{-T} \boldsymbol{N} \| \tag{2.36}$$

where the area normals are unit vectors.

Having completely defined the fundamental kinematic quantities and geometric tools that are necessary for the development of the classical wave theory, let us move on to the dynamics part to relate motion with forces to observe their effects on motion. In the remaining part of this chapter, deformations are considered to be small such that the reference and the spatial descriptions coincide.

2.2 Cauchy's Stress Theorem

In rigid body dynamics, the motion is not accompanied by deformations and is composed solely of a combination of rigid body translation and rotation in space. However, oftentimes, as long as the characteristic length scale is not too large and the material body is not infinitely rigid, which is the case in most engineering problems, rigid body approximation is inadequate since deformations taking place during the motion come to be pronounced, which in turn creates internal stresses. Therefore, it is necessary to establish a mathematical representation of internal stresses in the first place. Let us consider a material body $\mathcal{B}$, and suppose that a part of $\mathcal{B}$ is cut denoted with $\mathcal{B}_p$ along with its boundary $\partial\mathcal{B}_p$. Moreover, if the body is under the action

of external forces, internal forces are developed throughout the body, transferred as stress fluxes, generating a traction vector on the boundary $\partial\mathcal{B}_p$ of the cut part $\mathcal{B}_p$. This traction is called stress traction vector $\boldsymbol{t}$ or Cauchy stress traction vector, that is, the force measured per unit deformed surface area. It is essential to notice that the stress traction vector is defined with respect to deformed configuration.

The stress traction vector associates with Cauchy's stress tensor $\boldsymbol{\sigma}$ via Cauchy's Stress Theorem given by

$$\boldsymbol{t}(\boldsymbol{x}, t, \boldsymbol{n}) = \boldsymbol{\sigma}(\boldsymbol{x}, t) \cdot \boldsymbol{n} \tag{2.37}$$

where $\boldsymbol{\sigma}$ denotes a symmetric second order tensor field, the Cauchy stress tensor, $\boldsymbol{n}$ denotes the surface normal on which the traction vector $\boldsymbol{t}$ is acting. An important observation regarding Cauchy's Stress Theorem is that it encapsulates Newton's action-reaction principle. That is,

$$\begin{aligned} \boldsymbol{t}(\boldsymbol{x}, t, -\boldsymbol{n}) &= -\boldsymbol{\sigma}(\boldsymbol{x}, t) \cdot \boldsymbol{n} \\ &= -\boldsymbol{t}(\boldsymbol{x}, t,) \end{aligned} \tag{2.38}$$

for all unit vector $\boldsymbol{n}$. To prove the Cauchy Stress Theorem, let us first consider a representation of the stress tensor $\boldsymbol{\sigma}$. Imagine a small cube aligned with a background cartesian bases $\boldsymbol{e_{i=1,2,3}}$ such that surface normals are parallel to cartesian bases. Moreover, consider a traction vector $\boldsymbol{t^{(i)}} = \boldsymbol{t}(\boldsymbol{x}, t, \boldsymbol{e_i})$ associated with each surface normal. Then, on each face, $\boldsymbol{t^{(i)}}$ can be decomposed into its components, that is,

$$\boldsymbol{t^{(1)}} = \sigma_{11}\boldsymbol{e_1} + \sigma_{21}\boldsymbol{e_2} + \sigma_{31}\boldsymbol{e_3} \tag{2.39a}$$

$$\boldsymbol{t^{(2)}} = \sigma_{12}\boldsymbol{e_1} + \sigma_{22}\boldsymbol{e_2} + \sigma_{32}\boldsymbol{e_3} \tag{2.39b}$$

$$\boldsymbol{t^{(3)}} = \sigma_{13}\boldsymbol{e_1} + \sigma_{23}\boldsymbol{e_2} + \sigma_{33}\boldsymbol{e_3} \tag{2.39c}$$

Following (2.39a), (2.39b), (2.39c) the Cauchy stress tensor $\boldsymbol{\sigma}$ would be considered as both mathematical and physical object into which complete information regarding surface tractions are embedded since any traction vector can be constructed by superposing traction vectors constituting the stress tensor $\boldsymbol{\sigma}$. Now, consider an arbitrary surface depicted in Figure 2.3. Assume also that there is a traction vector $\boldsymbol{t}^{(n)}$ acting on the surface ABC and a body force $\rho\boldsymbol{b}$ is present acting downwards on the body.

Then, by conservation of linear momentum, the following equation can be written.

$$\boldsymbol{t}^{(\boldsymbol{n})}\Delta S + \boldsymbol{t}^{(\boldsymbol{-1})}\Delta S_1 + \boldsymbol{t}^{(\boldsymbol{-2})}\Delta S_2 + \boldsymbol{t}^{(\boldsymbol{-3})}\Delta S_3 - \rho\boldsymbol{b}\Delta V = \rho\boldsymbol{a}\Delta V \tag{2.40}$$

where ΔV denotes the volume of the tetrahedron. In addition, realizing the relationship between surface areas,

$$\Delta S_1 = \Delta S n_1, \quad \Delta S_2 = \Delta S n_2, \quad \Delta S_3 = \Delta S n_3 \tag{2.41}$$

and incorporating (2.38), (2.41); (2.40) can be recast into following form.

$$\boldsymbol{t}^{(\boldsymbol{n})} - \boldsymbol{t}^{(\boldsymbol{1})}n_1 - \boldsymbol{t}^{(\boldsymbol{2})}n_2 - \boldsymbol{t}^{(\boldsymbol{3})}n_3 = \rho(\boldsymbol{a}+\boldsymbol{b})\frac{\Delta V}{\Delta S} \tag{2.42}$$

If we let the tetrahedron shrink isotropically, i.e. keeping point O and the surface normal $\boldsymbol{n}$ fixed, in the limit

$$\lim_{\Delta S, \Delta V \to 0} = \rho(\boldsymbol{a}+\boldsymbol{b})\frac{\Delta V}{\Delta S} = 0 \tag{2.43}$$

leading to

$$\boldsymbol{t}^{(\boldsymbol{n})} = \boldsymbol{t}^{(\boldsymbol{1})}n_1 + \boldsymbol{t}^{(\boldsymbol{2})}n_2 + \boldsymbol{t}^{(\boldsymbol{3})}n_3 \tag{2.44}$$

Finally, introducing the stress tensor $\boldsymbol{\sigma}$ into (2.44), we would finally prove the Cauchy Stress Theorem.

$$\begin{aligned} \boldsymbol{t}^{(\boldsymbol{n})} &= n_1\boldsymbol{e_1}\cdot\boldsymbol{\sigma} + n_2\boldsymbol{e_2}\cdot\boldsymbol{\sigma} + n_3\boldsymbol{e_3}\cdot\boldsymbol{\sigma}n_3 \\ &= \boldsymbol{n}\cdot\boldsymbol{\sigma} = \boldsymbol{\sigma}\cdot\boldsymbol{n} \end{aligned} \tag{2.45}$$

where in the latter the symmetry property of $\boldsymbol{\sigma} = \boldsymbol{\sigma}^T$ is utilized.

Having obtained the stress tensor $\boldsymbol{\sigma}(\boldsymbol{x}, t)$, deformations can now be linked to internal forces via constitutive equations governing the response of the material body, which will be discussed in the forthcoming section.

2.3 Conservation Laws of Continuum Mechanics

Consider the cutout part $\mathcal{B}_p$ of the material body $\mathcal{B}$ along with its boundary $\partial\mathcal{B}_p$. Recalling the self-impenetrability restriction imposed by the positive-definiteness of J, the motion of the body $\mathcal{B}$ can be equally represented by the cut part $\mathcal{B}_p$. Then, to

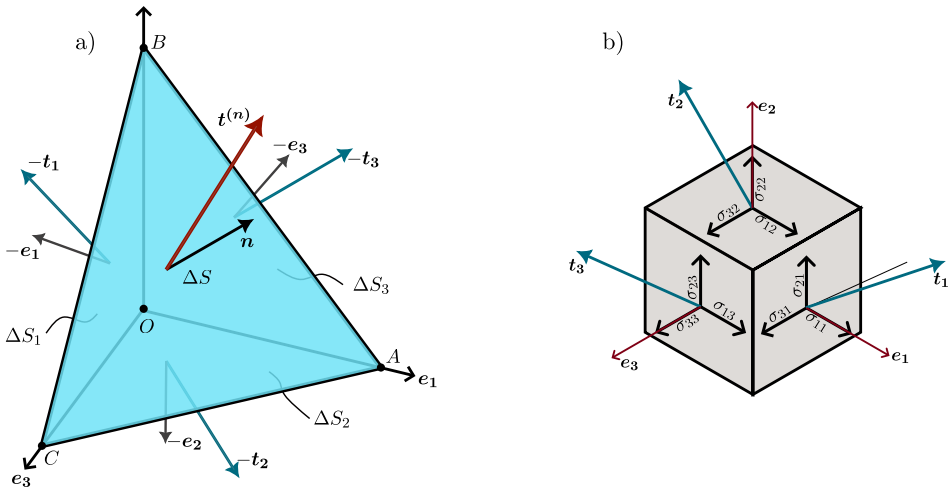

Figure 2.3: Schematic illustration of Cauchy's stress theorem. a) depicts an arbitrary surface having an area normal $\boldsymbol{n}$ on which the traction force is acting $\boldsymbol{t}^{(n)}$, while b) represents projections of traction forces on planes with normals parallel to cartesian coordinate bases $e_{i=1,2,3}$ constituting the Cauchy Stress Tensor.

characterize the state of motion, the following fundamental physical quantities might be identified on $\mathcal{B}_p$

i. Mass	$m \coloneqq \int_{\mathcal{B}_p} \rho dV$	(2.46a)
ii. Linear Momentum	$\boldsymbol{I} \coloneqq \int_{\mathcal{B}_p} \rho \boldsymbol{v} dV$	(2.46b)
iii. Angular momentum	$\boldsymbol{L} \coloneqq \int_{\mathcal{B}_p} \boldsymbol{r} \times \rho \boldsymbol{v} dV$	(2.46c)
iv. Kinetic Energy	$K \coloneqq \int_{\mathcal{B}_p} \frac{1}{2} \rho \boldsymbol{v} \cdot \boldsymbol{v} dV$	(2.46d)
v. Internal Energy	$E \coloneqq \int_{\mathcal{B}_p} \rho e dV$	(2.46e)
vi. Entropy	$H \coloneqq \int_{\mathcal{B}_p} \rho \eta dV$	(2.46f)
vii. Entropy Production	$\Gamma \coloneqq \int_{\mathcal{B}_p} \rho \gamma dV$	(2.46g)

where the fields $\rho(\boldsymbol{x}, t)$, $\boldsymbol{v}(\boldsymbol{x}, t)$, $\boldsymbol{u}(\boldsymbol{x}, t)$, $e(\boldsymbol{x}, t)$, $\eta(\boldsymbol{x}, t)$, and $\gamma(\boldsymbol{x}, t)$ represent the density, velocity, displacement, internal energy per unit mass, entropy per unit mass, and entropy production per unit mass, respectively. These are the physical fields

associated with the state of the body in the thermomechanical framework. However, these field variables depend upon the very nature of the problem under consideration, and subsequently, one might need to introduce additional field variables dictated by the problem.

Unless the body $\mathcal{B}$ is in an inertial state, that is, in a state of constant translational motion, and unless the internal state of $\mathcal{B}$ is stationary, there have to be external sources affecting the state of the body $\mathcal{B}$, and hence the state of the cut part $\mathcal{B}_p$. Restricting ourselves to a thermomechanical framework, and without loss of generality, these external sources might be classified into two types, namely mechanical sources and thermal sources. Both sources manifest themselves as surface and body loads, the former being the stress traction vector $\boldsymbol{t}(\boldsymbol{x}, t)$ and the heat flux $h(\boldsymbol{x}, t)$, and the latter being the mass-specific body force $\boldsymbol{b}(\boldsymbol{x}, t)$ and the mass-specific heat source $(\boldsymbol{x}, t)$. The physical quantities attributed to these loads that are acting on $\mathcal{B}_p$ are

$$\text{i. Mechanical Force} \qquad \boldsymbol{F} \coloneqq \int_{\mathcal{B}_p} \rho \boldsymbol{b} dV + \int_{\partial \mathcal{B}_p} \boldsymbol{t} dA \tag{2.47a}$$

$$\text{ii. Mechanical Couple} \qquad \boldsymbol{M} \coloneqq \int_{\mathcal{B}_p} \boldsymbol{r} \times \rho \boldsymbol{b} dV + \int_{\partial \mathcal{B}_p} \boldsymbol{r} \times \boldsymbol{t} dA \tag{2.47b}$$

$$\text{iii. Mechanical Power} \qquad P \coloneqq \int_{\mathcal{B}_p} \rho \boldsymbol{b} \cdot \boldsymbol{v} dV \int_{\partial \mathcal{B}_p} \boldsymbol{t} \cdot \boldsymbol{v} dA \tag{2.47c}$$

$$\text{iv. Thermal Power} \qquad Q \coloneqq \int_{\mathcal{B}_p} \rho r dV - \int_{\partial \mathcal{B}_p} h dA \tag{2.47d}$$

$$\text{v. Entropy Power} \qquad S \coloneqq \int_{\mathcal{B}_p} \rho \frac{r}{\theta} dV - \int_{\partial \mathcal{B}_p} \frac{h}{\theta} dA \tag{2.47e}$$

with $\theta(\boldsymbol{x}, t)$ being the temperature field. Inevitably, then, the question of how to establish an interrelationship between the state variables and the external loads disturbing the state would be raised. The answer lies in the conservation laws of continuum mechanics, along with the entropy imbalance constituting the 2$^{\text{nd}}$ law of thermody-

namics, given by the following relations.

i. Conservation of Mass	$\dfrac{\mathrm{d}m}{\mathrm{d}t} = 0$	(2.48a)
ii. Conservation of Linear Momentum	$\dfrac{\mathrm{d}\boldsymbol{I}}{\mathrm{d}t} = \boldsymbol{F}$	(2.48b)
iii. Conservation of Angular Momentum	$\dfrac{\mathrm{d}\boldsymbol{L}}{\mathrm{d}t} = \boldsymbol{M}$	(2.48c)
iv. Conservation of Energy	$\dfrac{\mathrm{d}}{\mathrm{d}t}(K+E) = P+Q$	(2.48d)
v. Entropy Imbalance	$\dfrac{\mathrm{d}H}{\mathrm{d}t} = \Gamma + S \geq 0$	(2.48e)

Let us investigate each case incorporating (2.46a)-(2.47e) into (2.48a)-(2.48e). In what follows, the Gauss Theorem, which relates surface integrals to volume integrals, will be utilized when necessary to obtain a global expression governing the state of $\mathcal{B}_p$.

2.3.1 Conservation of Mass

$$\frac{\mathrm{d}m}{\mathrm{d}t} = \frac{\mathrm{d}}{\mathrm{d}t}\int_{\mathcal{B}_p} \rho dV = \int_{\mathcal{B}_p} \dot{\rho} dV = 0 \tag{2.49}$$

Applying the principle of localization

$$\lim_{\mathcal{B}_p \to dV} \int_{\mathcal{B}_p} \dot{\rho}\ dV = 0 \tag{2.50}$$

yields the local form of the conservation of mass

$$\boxed{\dot{\rho} = 0} \tag{2.51}$$

2.3.2 Conservation of Linear Momentum

$$\frac{\mathrm{d}}{\mathrm{d}t}\int_{\mathcal{B}_p} \rho \boldsymbol{v}\ dV = \int_{\mathcal{B}_p} (\dot{\rho}\boldsymbol{v} + \rho\dot{\boldsymbol{v}})\ dV = \int_{\mathcal{B}_p} \rho \boldsymbol{b}\ dV + \int_{\partial\mathcal{B}_p} \boldsymbol{t}\ dA \tag{2.52}$$

Utilizing Cauchy's stress theorem on the surface traction $\boldsymbol{t}$ and then applying the Gauss theorem on the resultant surface integral term would yield

$$\int_{\partial\mathcal{B}_p} \boldsymbol{t}\ dA \overset{Cauchy}{=} \int_{\partial\mathcal{B}_p} \boldsymbol{\sigma}\cdot\boldsymbol{n}\ dA \overset{Gauss}{=} \int_{\mathcal{B}_p} \boldsymbol{\nabla}\cdot\boldsymbol{\sigma}\ dV \tag{2.53}$$

Finally, insertion of the conservation of mass given by (2.51) along with (2.53) gives,

$$\int_{\mathcal{B}_p} \rho \dot{\boldsymbol{v}} \; dV = \int_{\mathcal{B}_p} \rho \boldsymbol{b} \; dV + \int_{\mathcal{B}_p} \boldsymbol{\nabla} \cdot \boldsymbol{\sigma} \; dV \tag{2.54}$$

Then, through the principle of localization

$$\lim_{\mathcal{B}_p \to dV} \int_{\mathcal{B}_p} (\rho \dot{\boldsymbol{v}} - \rho \boldsymbol{b} - \boldsymbol{\nabla} \cdot \boldsymbol{\sigma}) \; dV = \boldsymbol{0} \tag{2.55}$$

we get the local form of the conservation of linear momentum, which governs the classical wave equation

$$\boxed{\rho \dot{\boldsymbol{v}} = \rho \ddot{\boldsymbol{u}} = \rho \boldsymbol{b} + \boldsymbol{\nabla} \cdot \boldsymbol{\sigma}} \tag{2.56}$$

2.3.3 Conservation of Angular Momentum

$$\frac{\mathrm{d}}{\mathrm{d}t} \int_{\mathcal{B}_p} \boldsymbol{r} \times \rho \boldsymbol{v} \; dV = \int_{\mathcal{B}_p} \boldsymbol{r} \times \rho \boldsymbol{b} \; dV + \int_{\partial \mathcal{B}_p} \boldsymbol{r} \times \boldsymbol{t} \; dA \tag{2.57}$$

where $\boldsymbol{r} = \boldsymbol{x} + \boldsymbol{x_0}$ represents the position vector emanating from an arbitrary origin obtained by shifting the origin of the reference coordinate system by a constant vector $\boldsymbol{x_0}$. This time, the transformation of the surface integral term is rather more involved than the previous part due to cross product term. Let us first express the surface integral term in indicial notation.

$$\int_{\partial \mathcal{B}_p} \boldsymbol{r} \times \boldsymbol{t} \; dA = \int_{\partial \mathcal{B}_p} \epsilon_{ijk} r_j t_k \; dA = \int_{\partial \mathcal{B}_p} \epsilon_{ijk} r_j \sigma_{kp} n_p \; dA \tag{2.58}$$

where we introduce the Levi-Civita symbol defined by

$$\epsilon_{ijk} = \begin{cases} 0, & \text{if } i = j, \text{ or } j = k, \text{ or } k = i \\ +1, & \text{for even permutation of } i, j, k; \text{ i.e. } (123,\ 231,\ 312) \\ -1, & \text{for odd permutation of } i, j, k; \quad \text{i.e. } (132,\ 213,\ 321) \end{cases} \tag{2.59}$$

implying cyclic-order property, that is, $\epsilon_{ijk} = \epsilon_{jki} = \epsilon_{kij} = -\epsilon_{ikj} = -\epsilon_{jik} = -\epsilon_{kji}$.

Then, applying the Gauss theorem on the latter would eventually give

$$\begin{aligned}
\int_{\partial\mathcal{B}_p} \epsilon_{ijk} r_j \sigma_{kp} n_p \; dA &= \int_{\mathcal{B}_p} \frac{\partial}{\partial x_p}(\epsilon_{ijk} r_j \sigma_{kp} n_p) \; dV \\
&= \int_{\mathcal{B}_p} \left[\epsilon_{ijk} \delta_{jp} \sigma_{kp} + \epsilon_{ijk} r_j \frac{\partial \sigma_{kp}}{\partial x_p} \right] dV \\
&= \int_{\mathcal{B}_p} \epsilon_{ijk} \sigma_{kj} \; dV + \int_{\mathcal{B}_p} \epsilon_{ijk} r_j \frac{\partial \sigma_{kp}}{\partial x_p} \; dV \\
&= \int_{\mathcal{B}_p} \epsilon_{ikj} \sigma_{kj} \; dV + \int_{\mathcal{B}_p} \epsilon_{ijk} r_j \frac{\partial \sigma_{kp}}{\partial x_p} \; dV \\
&= \int_{\mathcal{B}_p} -\boldsymbol{\epsilon} : \boldsymbol{\sigma} \; dV + \int_{\mathcal{B}_p} \boldsymbol{r} \times \boldsymbol{\nabla} \cdot \boldsymbol{\sigma} \; dV
\end{aligned} \tag{2.60}$$

where in the latter cyclic-order property of the Levi-Civita symbol is introduced. Moreover, by expanding the time derivative over the integral on left hand side and inserting (2.51), we would get

$$\begin{aligned}
\frac{\mathrm{d}}{\mathrm{d}t} \int_{\mathcal{B}_p} \boldsymbol{r} \times \rho \boldsymbol{v} \; dV &= \int_{\mathcal{B}_p} (\dot{\boldsymbol{r}} \times \rho \boldsymbol{v} + \boldsymbol{r} \times \dot{\rho} \boldsymbol{v} + \boldsymbol{r} \times \rho \dot{\boldsymbol{v}}) \; dV \\
&= \int_{\mathcal{B}_p} \boldsymbol{v} \times \rho \boldsymbol{v} \; dV + \int_{\mathcal{B}_p} \boldsymbol{r} \times \dot{\rho} \boldsymbol{v} \; dV + \int_{\mathcal{B}_p} \boldsymbol{r} \times \rho \dot{\boldsymbol{v}} \; dV \\
&= \int_{\mathcal{B}_p} \boldsymbol{r} \times \rho \dot{\boldsymbol{v}} \; dV = \int_{\mathcal{B}_p} \boldsymbol{r} \times \rho \ddot{\boldsymbol{u}} \; dV
\end{aligned} \tag{2.61}$$

using the cross product identity $\boldsymbol{v} \times \boldsymbol{v} = \boldsymbol{0}$. Finally, combining all terms

$$\int_{\mathcal{B}_p} \boldsymbol{r} \times (\rho \ddot{\boldsymbol{u}} - \rho \boldsymbol{b} - \boldsymbol{\nabla} \cdot \boldsymbol{\sigma}) \; dV + \int_{\mathcal{B}_p} \boldsymbol{\epsilon} : \boldsymbol{\sigma} \; dV = \boldsymbol{0} \tag{2.62}$$

Realizing further in (2.62) that the first integral corresponds to the conservation of linear momentum and hence vanishes, the principle of localization on (2.62) yields

$$\lim_{\mathcal{B}_p \to dV} \int_{\mathcal{B}_p} \boldsymbol{\epsilon} : \boldsymbol{\sigma} = \boldsymbol{0} \;\; \rightsquigarrow \;\; \boldsymbol{\epsilon} \cdot \boldsymbol{\sigma} = \boldsymbol{0} \tag{2.63}$$

implying, with the insertion of (2.59), that

$$\epsilon_{123}(\sigma_{23} - \sigma_{32}) = 0 \;\rightsquigarrow\; \sigma_{23} = \sigma_{32} \tag{2.64a}$$

$$\epsilon_{231}(\sigma_{31} - \sigma_{13}) = 0 \;\rightsquigarrow\; \sigma_{31} = \sigma_{13} \tag{2.64b}$$

$$\epsilon_{312}(\sigma_{12} - \sigma_{21}) = 0 \;\rightsquigarrow\; \sigma_{12} = \sigma_{21} \tag{2.64c}$$

leading us to the conclusion that as long as there are no body moments analogous to body forces, the stress tensor $\boldsymbol{\sigma}$ is always symmetric, obligated by the conservation of angular momentum. In other words, the net moment caused by external forces is

counterbalanced by the moment produced by the inertia force, while internal couples balance out each other.

$$\boxed{\boldsymbol{\sigma} = \boldsymbol{\sigma}^T} \tag{2.65}$$

However, it is important to observe that presence of body moments distorts the symmetricity of the stress tensor $\boldsymbol{\sigma}$ prohibiting (2.65).

2.3.4 Conservation of Energy

$$\frac{\mathrm{d}}{\mathrm{d}t}\int_{\mathcal{B}_p}\left(\frac{1}{2}\rho\boldsymbol{v}\cdot\boldsymbol{v}+\rho e\right)dV = \int_{\mathcal{B}_p}\rho\boldsymbol{b}\cdot\boldsymbol{v}\,dV + \int_{\partial\mathcal{B}_p}\boldsymbol{t}\cdot\boldsymbol{v}\,dA + \int_{\mathcal{B}_p}\rho r\,dV - \int_{\partial\mathcal{B}_p} h\,dA \tag{2.66}$$

Analogous to preceding cases, let us first concentrate on the surface integral terms. The second term representing the power expended by traction forces might be recast into the following form, recalling the commutativity of the scalar product operator and exploiting the symmetry of $\boldsymbol{\sigma}$.

$$\int_{\partial\mathcal{B}_p}\boldsymbol{v}\cdot\boldsymbol{t}\;dA = \int_{\partial\mathcal{B}_p}\boldsymbol{v}\cdot\boldsymbol{\sigma}\cdot\boldsymbol{n}\;dA = \int_{\partial\mathcal{B}_p}\boldsymbol{\sigma}\boldsymbol{v}\cdot\boldsymbol{n}\;dA = \int_{\mathcal{B}_p}\boldsymbol{\nabla}\cdot(\boldsymbol{\sigma}\boldsymbol{v})\;dV \tag{2.67}$$

The latter might be expanded to what follows.

$$\int_{\partial\mathcal{B}_p}\boldsymbol{\nabla}\cdot(\boldsymbol{\sigma}\boldsymbol{v})\;dV = \int_{\partial\mathcal{B}_p}(\boldsymbol{\nabla}\cdot\boldsymbol{\sigma})\boldsymbol{v}\;dV + \int_{\partial\mathcal{B}_p}\boldsymbol{\sigma}:\boldsymbol{\nabla}\boldsymbol{v}\;dV \tag{2.68}$$

In (2.68), the term $\boldsymbol{\nabla}\boldsymbol{v}$ is called the velocity gradient, additive decomposition of which gives the rate of deformation tensor, so-called strain rate tensor in small deformation theory, $\dot{\boldsymbol{\varepsilon}}$ and the spin tensor $\dot{\boldsymbol{\omega}}$, respectively. That is,

$$\begin{aligned}\frac{\mathrm{d}}{\mathrm{d}t}\boldsymbol{\nabla}\boldsymbol{u} = \boldsymbol{\nabla}\dot{\boldsymbol{u}} = \boldsymbol{\nabla}\boldsymbol{v} &= \frac{1}{2}\big(\boldsymbol{\nabla}\boldsymbol{u}+\boldsymbol{\nabla}\boldsymbol{u}^T\big)+\frac{1}{2}\big(\boldsymbol{\nabla}\boldsymbol{u}-\boldsymbol{\nabla}\boldsymbol{u}^T\big)\\ &= \mathrm{sym}\boldsymbol{\nabla}\boldsymbol{v}+\mathrm{skw}\boldsymbol{\nabla}\boldsymbol{v}\\ &= \dot{\boldsymbol{\varepsilon}}+\dot{\boldsymbol{\omega}}\end{aligned} \tag{2.69}$$

where the rotation tensor $\boldsymbol{\omega} \coloneqq \mathrm{skw}\boldsymbol{\nabla}\boldsymbol{u}$ obtained from the skew-symmetric part of the deformation tensor corresponds to rigid body rotation. This suggests that there must be no contribution to internal energy from the spin tensor $\dot{\boldsymbol{\omega}}$. Let us show that this is

indeed the case by exploiting the symmetry of $\boldsymbol{\sigma}$.

$$\begin{aligned}\boldsymbol{\sigma} : \boldsymbol{\nabla v} &= \frac{1}{2}\big(\boldsymbol{\sigma} : \boldsymbol{\nabla v} + \boldsymbol{\sigma} : \boldsymbol{\nabla v}^T\big) + \frac{1}{2}\big(\boldsymbol{\sigma} : \boldsymbol{\nabla v} - \boldsymbol{\sigma} : \boldsymbol{\nabla v}^T\big) \\ &= \frac{1}{2}\big(\boldsymbol{\sigma} : \boldsymbol{\nabla v} + \boldsymbol{\sigma} : \boldsymbol{\nabla v}^T\big) + \frac{1}{2}\Big(\boldsymbol{\sigma} : \boldsymbol{\nabla v} - (\boldsymbol{\nabla v} : \boldsymbol{\sigma})^T\Big) \\ &= \frac{1}{2}\big(\boldsymbol{\sigma} : \boldsymbol{\nabla v} + \boldsymbol{\sigma} : \boldsymbol{\nabla v}^T\big) \\ &= \boldsymbol{\sigma} : \boldsymbol{\nabla v} = \boldsymbol{\sigma} : \dot{\boldsymbol{\varepsilon}} \end{aligned} \tag{2.70}$$

where in the second step, the transpose operation applies on a scalar quantity hence leaving the term in parentheses unchanged. Furthermore, the commutativity of the double contraction operator is also utilized, details of which will be given in the next section. Next, let us consider the heat flux term. Introducing the heat flux vector $\boldsymbol{q}$ via Cauchy's theorem and applying Gauss theorem to transform surface integral to volume integral, we get

$$\int_{\partial\mathcal{B}_p} h \; dA = \int_{\partial\mathcal{B}_p} \boldsymbol{q} \cdot \boldsymbol{n} \; dA = \int_{\mathcal{B}_p} \boldsymbol{\nabla} \cdot \boldsymbol{q} \; dV \tag{2.71}$$

Lastly, performing the time derivative operation in (2.66) and substituting (2.51)

$$\begin{aligned}\frac{\mathrm{d}}{\mathrm{d}t}\int_{\mathcal{B}_p}\left(\frac{1}{2}\rho\boldsymbol{v}\cdot\boldsymbol{v} + \rho e\right) dV &= \int_{\mathcal{B}_p}\frac{1}{2}\dot{\rho}\boldsymbol{v}\cdot\boldsymbol{v}\, dV + \int_{\mathcal{B}_p}\rho\boldsymbol{v}\cdot\dot{\boldsymbol{v}} + \int_{\mathcal{B}_p}\dot{\rho}e\, dV + \int_{\mathcal{B}_p}\rho\dot{e}\, dV \\ &= \int_{\mathcal{B}_p}\rho\boldsymbol{v}\cdot\dot{\boldsymbol{v}}\; dV + \int_{\mathcal{B}_p}\rho\dot{e}\; dV \end{aligned} \tag{2.72}$$

Inserting (2.70), (2.71), and (2.72), (2.66) can be recast into following form.

$$\int_{\mathcal{B}_p} \boldsymbol{v}\cdot(\rho\dot{\boldsymbol{v}} - \boldsymbol{\nabla}\cdot\boldsymbol{\sigma} - \rho\boldsymbol{b})\; dV + \int_{\mathcal{B}_p}(\rho\dot{e} - \boldsymbol{\sigma} : \dot{\boldsymbol{\varepsilon}} + \boldsymbol{\nabla}\cdot\boldsymbol{q})\; dV = 0 \tag{2.73}$$

Noting that the first term vanishes due to the conservation of linear momentum given by (2.56) and invoking the principle of localization

$$\lim_{\mathcal{B}_p\to dV}\int_{\mathcal{B}_p}(\rho\dot{e} - \boldsymbol{\sigma} : \dot{\boldsymbol{\varepsilon}} + \boldsymbol{\nabla}\cdot\boldsymbol{q})\; dV = 0 \tag{2.74}$$

the local form of conservation of energy read as follows.

$$\boxed{\rho\dot{e} = \boldsymbol{\sigma} : \dot{\boldsymbol{\varepsilon}} + \rho r - \boldsymbol{\nabla}\cdot\boldsymbol{q}} \tag{2.75}$$

2.3.5 Entropy Imbalance

$$\frac{\mathrm{d}}{\mathrm{d}t}\int_{\mathcal{B}_p}\rho\eta dV = \int_{\mathcal{B}_p}\rho\gamma dV + \int_{\mathcal{B}_p}\rho\frac{r}{\theta}dV - \int_{\partial\mathcal{B}_p}\frac{h}{\theta}dA \geq 0 \tag{2.76}$$

Let us first transform the surface integral into volume integral by applying the Gauss theorem on (2.76)

$$\begin{aligned}\int_{\partial\mathcal{B}_p}\frac{h}{\theta}dA=\int_{\partial\mathcal{B}_p}\frac{\boldsymbol{q}\cdot\boldsymbol{n}}{\theta}dA&=\int_{\partial\mathcal{B}_p}\frac{q_in_i}{\theta}dA\\&=\int_{\mathcal{B}_p}\frac{\partial}{\partial x_i}\Big(\frac{q_i}{\theta}\Big)dV\\&=\int_{\mathcal{B}_p}\frac{1}{\theta}\frac{\partial q_i}{\partial x_i}dV-\int_{\mathcal{B}_p}\frac{1}{\theta^2}q_i\frac{\partial\theta}{\partial x_i}dV\\&=\int_{\mathcal{B}_p}\frac{1}{\theta}\boldsymbol{\nabla}\boldsymbol{q}dV-\int_{\mathcal{B}_p}\frac{1}{\theta^2}\boldsymbol{q}\cdot\boldsymbol{\nabla}\theta dV\end{aligned}\tag{2.77}$$

Inserting (2.77) into (2.76) along with the conservation of mass equality given in (2.51) then would yield

$$\int_{\mathcal{B}_p}\rho\dot{\eta}dV=\int_{\mathcal{B}_p}\rho\gamma dV+\int_{\mathcal{B}_p}\rho\frac{r}{\theta}dV-\int_{\mathcal{B}_p}\frac{1}{\theta}\boldsymbol{\nabla}\cdot\boldsymbol{q}dV+\int_{\mathcal{B}_p}\frac{1}{\theta^2}\boldsymbol{q}\cdot\boldsymbol{\nabla}\theta dV\tag{2.78}$$

Applying the principle of localization on (2.78) gives

$$\lim_{\mathcal{B}_p\to dV}\int_{\mathcal{B}_p}\left(\rho\dot{\eta}-\rho\gamma-\rho\frac{r}{\theta}+\frac{1}{\theta}\boldsymbol{\nabla}\cdot\boldsymbol{q}-\frac{1}{\theta^2}\boldsymbol{q}\cdot\boldsymbol{\nabla}\theta\right)=0\tag{2.79}$$

Rearranging (2.79) and combining with the first law of thermodynamics, that is the conservation of energy given by (2.75), would eventually yield the entropy imbalance constituting the second law of thermodynamics.

$$\boxed{\rho\gamma=\rho\dot{\eta}-\frac{1}{\theta}(\rho\dot{e}-\boldsymbol{\sigma}:\dot{\boldsymbol{\varepsilon}})-\frac{1}{\theta^2}\boldsymbol{q}\cdot\boldsymbol{\nabla}\theta\geq 0}\tag{2.80}$$

The entropy imbalance principle states that the internal entropy production cannot be negative which puts a strong restriction on the evolution of a physical state, which is not the case for the first law as it tells about only the current physical state of a given system. Hence, it enables one to construct thermodynamically admissible material, or so-called constitutive equations a priori satisfying the entropy imbalance law. To demonstrate this, let us modify the entropy imbalance law given by (2.80) expression to have a better understanding. Let $\mathscr{D}$ be the mass-specific dissipation defined as

$$\rho\mathscr{D}\coloneqq\rho\theta\gamma\geq 0\tag{2.81}$$

where θ is the absolute temperature, i.e. $\theta>0$. Then, multiplying both sides of (2.80) and employing (2.81), the Clausius-Duhem Inequality (CDI) is obtained.

$$\rho\mathscr{D}=\rho\theta\dot{\eta}-\left(\rho\dot{e}-\boldsymbol{\sigma}:\dot{\boldsymbol{\varepsilon}}-\frac{1}{\theta}\boldsymbol{q}\cdot\boldsymbol{\nabla}\theta\right)\geq 0\tag{2.82}$$

The Clausius-Duhem Inequality can additively be splitted into local $\mathscr{D}_{\text{loc}}$ and conductive $\mathscr{D}_{\text{con}}$ terms.

$$\rho\mathscr{D}_{\text{loc}} \coloneqq \boldsymbol{\sigma} : \dot{\boldsymbol{\varepsilon}} - \rho\dot{e} + \rho\theta\dot{\eta} \geq 0 \tag{2.83}$$

$$\rho\mathscr{D}_{\text{con}} \coloneqq -\frac{1}{\theta}\boldsymbol{q} \cdot \boldsymbol{\nabla}\theta \geq 0 \tag{2.84}$$

where the former is called Clausius-Planck Inequality (CPI) and the latter is called Fourier Inequality (FI). The decomposition of CDI into CPI and FI puts firmer restriction that requires (2.83), (2.84) to be satisfied, exploiting decoupled mechanism of the local and conductive dissipation phenomena. As it can be observed from (2.83), local dissipation depends upon the temporal change of the state variables, whereas the conductive term depends on the absolute temperature gradient involving the non-local transport phenomenon. On the other hand, the dependence of CPI on the temporal change of the entropy is not suitable to arrive at a material equation for solids as it would be very challenging to control entropy as an independent state variable for a given material. Hence, rather than using the entropy as an independent state variable, the absolute temperature θ can alternatively be used by introducing Helmholtz's Free Energy Ψ via the Legendre transformation of the internal energy e that shifts the dependency on entropy η to the absolute temperature θ.

$$\Psi \coloneqq e - \theta\eta \tag{2.85}$$

Inserting (2.85) into (2.83), we would obtain the modified Clausius-Planck Inequality.

$$\begin{aligned}
\rho\mathscr{D}_{\text{loc}} &= \boldsymbol{\sigma} : \dot{\boldsymbol{\varepsilon}} - \rho\dot{e} + \rho\theta\dot{\eta} \geq 0 \\
&= \boldsymbol{\sigma} : \dot{\boldsymbol{\varepsilon}} - \rho\dot{\big(\overline{\Psi + \theta\eta}\big)} + \rho\theta\dot{\eta} \geq 0 \\
&= \boldsymbol{\sigma} : \dot{\boldsymbol{\varepsilon}} - \rho\dot{\Psi} - \rho\dot{\theta}\eta \geq 0
\end{aligned} \tag{2.86}$$

With the modified Clausius-Planck Inequality given by (2.86), the initial-boundary value problem (IBVP) for wave propagation in a dissipative thermoinelastic medium with thermal coupling can be formulated through the introduction of the set of internal state variables $\boldsymbol{\mathcal{I}}$,

$$\boldsymbol{\mathcal{I}} \coloneqq \big\{(\boldsymbol{\alpha}_1, \boldsymbol{\alpha}_2, \ldots, \boldsymbol{\alpha}_n) \in \mathbb{R}^n \times \mathbb{R}^m \ldots \times \mathbb{R}^k \mid \rho\mathscr{D}_{\text{loc}} \geq 0\big\} \tag{2.87}$$

with $\boldsymbol{\alpha}_i$ corresponding to ith generalized internal variable vector, while n, m, and k are positive integers denoting the dimension of the corresponding internal variable

vector. The overall state of the medium, then, can be described by the state variables

$$\text{State}(\boldsymbol{x}, t) = \{\boldsymbol{\varepsilon}(\boldsymbol{x}, t), \theta(\boldsymbol{x}, t), \boldsymbol{\mathcal{I}}(\boldsymbol{x}, t)\} \tag{2.88}$$

where

$\boldsymbol{\varepsilon}(\boldsymbol{x}, t)$: the total strain tensor (external),

$\theta(\boldsymbol{x}, t)$: the absolute temperature field (external),

$\boldsymbol{\mathcal{I}}(\boldsymbol{x}, t)$: the set of internal state variables (internal).

By the principle of equipresence, which states that the material equations should depend on the same set of variables, the Helmholtz free energy function takes the form $\Psi = \hat{\Psi}(\boldsymbol{\varepsilon}, \theta, \boldsymbol{\mathcal{I}})$. Then, the modified CPI in (2.86) takes the following form.

$$\rho \mathscr{D}_{\text{loc}} = \boldsymbol{\sigma} : \dot{\boldsymbol{\varepsilon}} - \rho \Big[\partial_{\boldsymbol{\varepsilon}} \hat{\Psi} : \dot{\boldsymbol{\varepsilon}} + \rho \partial_{\theta} \hat{\Psi} \dot{\theta} + \partial_{\boldsymbol{\mathcal{I}}} \hat{\Psi} \bullet \dot{\boldsymbol{\mathcal{I}}} + \dot{\theta} \eta \Big] \geq 0 \tag{2.89}$$

where $(\bullet)$ represents the generalized inner product operator. Rearranging (2.89) yields the general form of the local dissipation $\rho \mathscr{D}_{\text{loc}}$.

$$\rho \mathscr{D}_{\text{loc}} = \Big[\boldsymbol{\sigma} - \rho \partial_{\boldsymbol{\varepsilon}} \hat{\Psi} \Big] : \dot{\boldsymbol{\varepsilon}} - \Big[\rho \partial_{\theta} \hat{\Psi} + \rho \eta \Big] \dot{\theta} - \rho \partial_{\boldsymbol{\mathcal{I}}} \hat{\Psi} \bullet \dot{\boldsymbol{\mathcal{I}}} \geq 0 \tag{2.90}$$

In accordance with Coleman's exploitation method [89], which states that $\rho \mathscr{D}_{\text{loc}}$ should hold for arbitrary rates $\dot{\boldsymbol{\varepsilon}}$ and $\dot{\theta}$ to a priori satisfy the second law of thermodynamics, the first and the second terms of (2.90) should vanish identically. Thus, by introducing the set of thermodynamical variables conjugate to the set of internal state variables

$$\boldsymbol{\mathcal{F}} \coloneqq \Big\{ (\boldsymbol{\beta}_1, \boldsymbol{\beta}_2, \ldots, \boldsymbol{\beta}_n) \in \mathbb{R}^n \times \mathbb{R}^m \ldots \times \mathbb{R}^k \mid \rho \mathscr{D}_{\text{loc}} = \boldsymbol{\mathcal{F}} \bullet \dot{\boldsymbol{\mathcal{I}}} \geq 0 \Big\} \tag{2.91}$$

the stress tensor $\boldsymbol{\sigma}$ and the entropy field η can be expressed as follows.

$$\Big[\boldsymbol{\sigma} - \rho \partial_{\boldsymbol{\varepsilon}} \hat{\Psi} \Big] \rightsquigarrow \boldsymbol{\sigma} = \rho \partial_{\boldsymbol{\varepsilon}} \hat{\Psi} \quad \text{and} \quad \Big[\eta + \partial_{\theta} \hat{\Psi} \Big] \rightsquigarrow \eta = -\partial_{\theta} \hat{\Psi} \tag{2.92}$$

Insertion of (2.91) into (2.86), and introducing the material evolution equation describing the evolution of internal variables $\dot{\boldsymbol{\mathcal{I}}} \coloneqq \boldsymbol{\Sigma} = \hat{\boldsymbol{\Sigma}}(\dot{\boldsymbol{\varepsilon}}, \boldsymbol{\varepsilon}, \boldsymbol{\mathcal{I}}, \theta)$ depending upon the state given by (2.88) and the total strain rate, would eventually yield the general form of the local material dissipation.

$$\rho \mathscr{D}_{\text{loc}} = -\rho \partial_{\boldsymbol{\mathcal{I}}} \hat{\Psi} \bullet \dot{\boldsymbol{\mathcal{I}}} = \boldsymbol{\mathcal{F}} \bullet \hat{\boldsymbol{\Sigma}}(\dot{\boldsymbol{\varepsilon}}, \boldsymbol{\varepsilon}, \boldsymbol{\mathcal{I}}, \theta) \geq 0 \tag{2.93}$$

Table 2.1: The IBVP of thermally coupled wave propagation in thermoinelastic medium

IBVP of Thermally Coupled Wave Propagation in Thermoinelastic Medium

1. Balance Equations

Linear Momentum	$\rho\ddot{\boldsymbol{u}} = \boldsymbol{\nabla}\cdot\boldsymbol{\sigma} + \rho\boldsymbol{b}$
Energy	$\rho\dot{e} = \boldsymbol{\sigma} : \dot{\boldsymbol{\varepsilon}} + \rho r - \boldsymbol{\nabla}\cdot\boldsymbol{q}$

2. Constitutive Equations

Stress Field	$\boldsymbol{\sigma} = \rho\partial_{\boldsymbol{\varepsilon}}\hat{\Psi}(\boldsymbol{\varepsilon}, \boldsymbol{\mathcal{I}}, \theta)$
Entropy Field	$\eta = -\partial\hat{\Psi}(\boldsymbol{\varepsilon}, \boldsymbol{\mathcal{I}}, \theta)$
Thermodynamic Force	$\boldsymbol{\mathcal{F}} = -\rho\partial_{\boldsymbol{\mathcal{I}}}\hat{\Psi}(\boldsymbol{\varepsilon}, \boldsymbol{\mathcal{I}}, \theta)$
Evolution Equations	$\dot{\boldsymbol{\mathcal{I}}} = \boldsymbol{\Sigma}(\dot{\boldsymbol{\varepsilon}}, \hat{\boldsymbol{\varepsilon}}, \boldsymbol{\mathcal{I}}, \theta)$
Heat Flux	$\boldsymbol{q} = \hat{\boldsymbol{q}}\Big(\dot{\theta}, \theta, \boldsymbol{\nabla}\theta\Big)$ (FI)

3. Boundary Conditions

Displacement	$\boldsymbol{u} = \bar{\boldsymbol{u}}$	on	$\partial\mathcal{B}_{\boldsymbol{u}}$
Traction	$\boldsymbol{t} = \bar{\boldsymbol{t}} = \boldsymbol{\sigma}\boldsymbol{n}$	on	$\partial\mathcal{B}_{\boldsymbol{t}}$
Temperature	$\theta = \bar{\theta}$	on	$\partial\mathcal{B}_{\theta}$
Heat Flux	$h = \bar{h}$	on	$\partial\mathcal{B}_{h}$

4. Initial Conditions

Displacement	$\boldsymbol{u}(\boldsymbol{x}, t_0) = \boldsymbol{u}_0(\boldsymbol{x})$	in	$\mathcal{B}$
Velocity	$\boldsymbol{v}(\boldsymbol{x}, t_0) = \boldsymbol{v}_0(\boldsymbol{x})$	in	$\mathcal{B}$
Temperature	$\theta(\boldsymbol{x}, t_0) = \theta_0(\boldsymbol{x})$	in	$\mathcal{B}$

In Table 2.1, boundary $\partial\mathcal{B}$ of $\mathcal{B}$ is decomposed into four distinct sets on which the displacement field $\boldsymbol{u}$, the temperature field θ, the stress traction $\boldsymbol{t}$, and the heat flux h are prescribed respectively.

$\partial\mathcal{B}_{\boldsymbol{u}}$: on which the displacement field $\boldsymbol{u}$ is prescribed (Dirichlet BCs)

$\partial\mathcal{B}_{\theta}$: on which the temperature field θ is prescribed (Dirichlet BCs)

$\partial\mathcal{B}_{\boldsymbol{t}}$: on which the stress traction $\boldsymbol{t}$ is prescribed (Neumann BCs)

$\partial\mathcal{B}_{h}$: on which the heat flux h is prescribed (Neumann BCs)

It is essential to note that the Dirichlet and Neumann boundaries are disjoint, that is, they cannot simultaneously be prescribed on a boundary. The mathematical statement of this observation is as follows.

$$\partial\mathcal{B} = (\partial\mathcal{B}_{\boldsymbol{u}} \cup \partial\mathcal{B}_{\boldsymbol{t}}) \cup (\partial\mathcal{B}_{\theta} \cup \partial\mathcal{B}_{h}) \tag{2.94}$$

$$\partial\mathcal{B}_{\boldsymbol{u}} \cap \partial\mathcal{B}_{t} = \varnothing \qquad \text{and} \qquad \partial\mathcal{B}_{\theta} \cap \partial\mathcal{B}_{h} = \varnothing \tag{2.95}$$

This concludes the discussion on conservation laws and on the thermodynamical aspects of constitutive modeling. In the following section, classical elastic wave theory will be discussed and the analytical solution to the 3D wave propagation problem through isotropic elastic medium extending to infinity will be derived starting from the formulation of the balance of linear momentum utilizing variational principles. Derivations involved

2.4 Elastic Wave Equation

The general form of the wave equation given in Table 2.1 can be reduced to classical elastic wave equation that has an analytical solution provided that the following assumptions hold.

i. There is no heat transfer ($\boldsymbol{\nabla} \cdot \boldsymbol{q} \approx 0$), i.e., the deformation takes place at very high rate,

ii. There is no energy dissipation, i.e., the medium is perfectly elastic,

iii. Thermoelastic heating is negligible,

iv. The medium is isotropic, homogeneous and infinite,

v. There is no heat source present ($\rho r = 0$),

vi. The response of the medium is time-invariant, i.e., LTI system.

With the above assumptions, the classical wave equation can be obtained directly from Table 2.1. However, to obtain a deeper insight, the balance of linear momentum (2.75) will be derived from the variational principles [72]. The physical interpretation of the principle can be found in [71], [72], and [90]. In addition, the fundamentals of the calculus of variations can be found in [91].

2.4.1 Principle of Stationary Action

Let S denotes the action of the system and δS denotes the first variation of the action, respectively. Then, the principle of stationary action states that the system is in dynamic equilibrium when the first variation δS of the system vanishes.

$$\begin{aligned}\delta S &= \int_{t_1}^{t_2} [L(\boldsymbol{x}, \boldsymbol{u} + \epsilon\delta\boldsymbol{u}, \dot{\boldsymbol{u}} + \epsilon\delta\dot{\boldsymbol{u}}, \text{sym}(\boldsymbol{\nabla u} + \epsilon\boldsymbol{\nabla}\delta\boldsymbol{u})) - L(\boldsymbol{x}, \boldsymbol{u}, \dot{\boldsymbol{u}}, \text{sym}(\boldsymbol{\nabla u}))]dt \\ &= \int_{t_1}^{t_2} \frac{\mathrm{d}}{\mathrm{d}\epsilon}[L(\boldsymbol{x}, \boldsymbol{u} + \epsilon\delta\boldsymbol{u}, \dot{\boldsymbol{u}} + \epsilon\delta\dot{\boldsymbol{u}}, \text{sym}(\boldsymbol{\nabla u} + \epsilon\boldsymbol{\nabla}\delta\boldsymbol{u}))]\Big|_{\epsilon=0} dt \\ &= \int_{t_1}^{t_2} \left(\frac{\partial L}{\partial \boldsymbol{u}} \cdot \delta\boldsymbol{u} + \frac{\partial L}{\partial \dot{\boldsymbol{u}}} \cdot \delta\dot{\boldsymbol{u}} + \frac{\partial L}{\partial \boldsymbol{\varepsilon}} : \boldsymbol{\nabla}\delta\boldsymbol{u}\right) dt \end{aligned} \tag{2.96}$$

In (2.96), the virtual velocity and the virtual strain fields $\delta\dot{\boldsymbol{u}}$, $\text{sym}(\boldsymbol{\nabla u})$ are present in addition to the virutal displacement field. Therefore, both the time derivative and the gradient operator are required to be shifted by applying integration by parts on (2.96). That is,

$$\int_{t_1}^{t_2} \left(\frac{\partial L}{\partial \boldsymbol{u}} \cdot \delta\boldsymbol{u} + \frac{\partial}{\partial t}\left[\frac{\partial L}{\partial \dot{\boldsymbol{u}}} \cdot \delta\boldsymbol{u}\right] - \frac{\partial}{\partial t}\frac{\partial L}{\partial \dot{\boldsymbol{u}}} \cdot \delta\boldsymbol{u} + \boldsymbol{\nabla} \cdot \left[\frac{\partial L}{\partial \boldsymbol{\varepsilon}} \cdot \delta\boldsymbol{u}\right] - \boldsymbol{\nabla} \cdot \frac{\partial L}{\partial \boldsymbol{\varepsilon}} \cdot \delta\boldsymbol{u}\right) dt \tag{2.97}$$

where (2.97) can be recast into the following form.

$$\int_{t_1}^{t_2} dt\left(\frac{\partial L}{\partial \boldsymbol{u}} - \frac{\partial}{\partial t}\frac{\partial L}{\partial \dot{\boldsymbol{u}}} - \boldsymbol{\nabla} \cdot \frac{\partial L}{\partial \boldsymbol{\varepsilon}}\right) \cdot \delta\boldsymbol{u} + \int_{t_1}^{t_2} \boldsymbol{\nabla} \cdot \left[\frac{\partial L}{\partial \boldsymbol{\varepsilon}} \cdot \delta\boldsymbol{u}\right] dt + \left[\frac{\partial L}{\partial \dot{\boldsymbol{u}}} \cdot \delta\boldsymbol{u}\right]\Bigg|_{t=t_1}^{t=t_2} \tag{2.98}$$

In (2.96), (2.97), and (2.98) L denotes the Lagrangian or action function for a given differential volume element and given by (2.99)

$$L = K - \Pi \tag{2.99}$$

where K is the kinetic energy and $\Pi \coloneqq \Pi_{int} + \Pi_{ext}$ is the total potential energy due to internal and external forces.

$$K = \iiint_V \frac{1}{2}\rho \dot{\boldsymbol{u}} \cdot \dot{\boldsymbol{u}} dV \quad \text{and} \quad \Pi = \iiint_V \hat{\Psi}(\boldsymbol{\varepsilon}) dV - \iiint_V \rho \boldsymbol{b} \cdot \boldsymbol{u} dV - \oiint_{\partial V} \bar{\boldsymbol{t}} \cdot \boldsymbol{u} dA \tag{2.100}$$

Inserting the above expressions into variational formulation would yield the differential form of the equation of motion, the conservation of linear momentum principle.

$$\delta S = \int_{t_1}^{t_2} dt \left[\iiint_V dV \left(\rho \boldsymbol{b} - \rho \ddot{\boldsymbol{u}} + \boldsymbol{\nabla} \cdot \frac{\partial \hat{\Psi}}{\partial \varepsilon} \right) + \oiint_{\partial V} dA \left(\bar{\boldsymbol{t}} - \frac{\partial \hat{\Psi}}{\partial \boldsymbol{\varepsilon}} \cdot \boldsymbol{n} \right) \right] \cdot \delta \boldsymbol{u} \tag{2.101}$$

(2.101) gives the stationary action principles and always be fulfilled whenever δS vanishes. Since the virtual displacement field can take arbitrary values, the terms in brackets in (2.101) must vanish accordingly. Hence, recognizing $\partial_{\boldsymbol{\varepsilon}} \hat{\Psi}$ is the Cauchy stress tensor $\boldsymbol{\sigma}$, which will be shown in the subsequent section, (2.101) would yield the strong form of the local form of the conservation of linear momentum law.

2.4.2 Elastic Wave Equation For Isotropic, Homogeneous and Infinite Media

Having established the governing differential equation for the displacement field $\boldsymbol{u}(\boldsymbol{x}, t)$, the wave equation for an isotropic and infinitely homogeneous medium can be written by introducing the following Helmholtz Free Energy $\hat{\Psi}(\boldsymbol{\varepsilon})$ into the balance equation given in Table 2.2.

$$\Psi = \hat{\Psi}(\boldsymbol{\varepsilon}) = \frac{\lambda}{2} \text{tr}^2(\boldsymbol{\varepsilon}) + \mu \boldsymbol{\varepsilon} : \boldsymbol{\varepsilon} \tag{2.102}$$

In the above equation $\text{tr}(\bullet)$ is the trace operator and defined as, employing Einstein summation convention, $\text{tr}(\boldsymbol{A}) \coloneqq A_{kk}$. Similarly, double contraction operator $(\bullet) : (\bullet)$ is defined for an arbitrary tensors $\boldsymbol{A}$ and $\boldsymbol{B}$ as follows.

$$\boldsymbol{A} : \boldsymbol{B} \coloneqq \text{tr}\big(\boldsymbol{A}\boldsymbol{B}^T\big) = \boldsymbol{A}\boldsymbol{B}^T : \boldsymbol{1} = A_{ik} B_{jk} \delta_{ij} = A_{ik} B_{ik} \tag{2.103}$$

Table 2.2: The formulation of the IBVP of elastodynamics

Elastodynamics

1. Balance Equations

   Linear Momentum $\quad \rho\ddot{\boldsymbol{u}} = \boldsymbol{\nabla} \cdot \boldsymbol{\sigma} + \rho\boldsymbol{b}$

2. Constitutive Equations

   Stress Field $\quad \boldsymbol{\sigma} = \partial_{\boldsymbol{\varepsilon}} \hat{\Psi}(\boldsymbol{\varepsilon})$

3. Boundary Conditions

   Displacement $\quad \boldsymbol{u} = \bar{\boldsymbol{u}} \quad$ on $\quad \partial V_u$

   Traction $\quad \boldsymbol{t} = \bar{\boldsymbol{t}} = \boldsymbol{\sigma}\boldsymbol{n} \quad$ on $\quad \partial V_t$

4. Initial Conditions

   Displacement $\quad \boldsymbol{u}(\boldsymbol{x}, t_0) = \boldsymbol{u}_0(\boldsymbol{x}) \quad$ in $\quad V$

   Velocity $\quad \boldsymbol{v}(\boldsymbol{x}, t_0) = \boldsymbol{v}_0(\boldsymbol{x}) \quad$ in $\quad V$

Now, expression for the stress field can be found as follows.

$$\begin{aligned}\boldsymbol{\sigma} = \frac{\partial \Psi}{\partial \boldsymbol{\varepsilon}} &= \frac{\lambda}{2}\frac{\partial \text{tr}^2(\boldsymbol{\varepsilon})}{\partial \text{tr}(\boldsymbol{\varepsilon})}\frac{\partial \text{tr}(\boldsymbol{\varepsilon})}{\partial \boldsymbol{\varepsilon}} + \mu\frac{\partial \boldsymbol{\varepsilon}}{\partial \boldsymbol{\varepsilon}} : \boldsymbol{\varepsilon} + \mu\boldsymbol{\varepsilon} : \frac{\partial \boldsymbol{\varepsilon}}{\partial \boldsymbol{\varepsilon}} \\ &= \lambda \text{tr}(\boldsymbol{\varepsilon})\frac{\partial \varepsilon_{kk}}{\partial \varepsilon_{ij}} + \mu\frac{\partial \varepsilon_{pq}}{\partial \varepsilon_{ij}}\varepsilon_{pq} + \mu\varepsilon_{pq}\frac{\partial \varepsilon_{pq}}{\partial \varepsilon_{ij}} \\ &= \lambda \text{tr}(\boldsymbol{\varepsilon})\delta_{ki}\delta_{kj} + 2\mu\delta_{pi}\delta_{qj}\varepsilon_{pq} \\ &= \lambda \text{tr}(\boldsymbol{\varepsilon})\delta_{ij} + 2\mu\varepsilon_{ij} \\ &= \lambda \text{tr}(\boldsymbol{\varepsilon})\mathbf{1} + 2\mu\boldsymbol{\varepsilon}\end{aligned} \tag{2.104}$$

In order to be able to take the divergence of the stress field, the last equation should be rewritten in terms of the displacement field. That is,

$$\boldsymbol{\sigma} = \lambda \text{tr}(\text{sym}(\boldsymbol{\nabla u}))\mathbf{1} + 2\mu\, \text{sym}(\boldsymbol{\nabla u}) \tag{2.105}$$

where

$$\text{sym}(\boldsymbol{\nabla u}) \coloneqq \frac{1}{2}\left[\boldsymbol{\nabla u} + \boldsymbol{\nabla u}^T\right] \quad \text{and} \quad \text{tr}(\text{sym}(\boldsymbol{\nabla u})) = \text{tr}(\boldsymbol{\nabla u}) \tag{2.106}$$

The latter equality can be derived as follows.

$$\begin{aligned}\text{tr}(\text{sym}\boldsymbol{\nabla u}) &= \frac{1}{2}\left[\boldsymbol{\nabla u} : \mathbf{1} + \boldsymbol{\nabla u}^T : \mathbf{1}\right] \\ &= \frac{1}{2}\left[\frac{\partial u_i}{\partial x_j}\delta_{ij} + \frac{\partial u_j}{\partial x_i}\delta_{ij}\right] \\ &= \frac{\partial u_i}{\partial x_i} = \boldsymbol{\nabla} \cdot \boldsymbol{u} = \text{tr}(\boldsymbol{\nabla u})\end{aligned} \tag{2.107}$$

Then, taking the divergence of the stress field yields

$$\begin{aligned}\boldsymbol{\nabla} \cdot \boldsymbol{\sigma} = \frac{\partial \sigma_{ij}}{\partial x_j} &= \lambda\frac{\partial}{\partial x_j}\left[\frac{\partial u_k}{\partial x_k}\right]\delta_{ij} + \mu\frac{\partial}{\partial x_j}\left[\frac{\partial u_i}{\partial x_j} + \frac{\partial u_j}{\partial x_i}\right] \\ &= \lambda\frac{\partial}{\partial x_i}\frac{\partial u_k}{\partial x_k} + \mu\frac{\partial}{\partial x_j}\frac{\partial u_i}{\partial x_j} + \mu\frac{\partial}{\partial x_j}\frac{\partial u_j}{\partial x_i} \\ &= (\lambda + \mu)\frac{\partial}{\partial x_i}\frac{\partial u_j}{\partial x_j} + \mu\frac{\partial}{\partial x_j}\frac{\partial u_i}{\partial x_j} \\ &= (\lambda + \mu)\boldsymbol{\nabla}\boldsymbol{\nabla} \cdot \boldsymbol{u} + \mu\boldsymbol{\nabla} \cdot \boldsymbol{\nabla u}\end{aligned} \tag{2.108}$$

Finally, governing differential equation for the elastic wave equation can be obtained.

$$\boxed{\rho\ddot{\boldsymbol{u}} = (\lambda + \mu)\boldsymbol{\nabla}\boldsymbol{\nabla} \cdot \boldsymbol{u} + \mu\boldsymbol{\nabla} \cdot \boldsymbol{\nabla u} + \rho\boldsymbol{b}} \tag{2.109}$$

2.4.3 Lamé's Solution

Analytical solution to wave equation can be achieved by invoking Lamé's Theorem, which requires decomposition of the displacement field into divergence-free and curl-free parts utilizing Helmholtz's Decomposition Theorem introducing scalar potential $\phi(\boldsymbol{x},t)$ and vector potential $\boldsymbol{\psi}(\boldsymbol{x},t)$. Then, the displacement field $\boldsymbol{u}(\boldsymbol{x},t)$ can be represented as $\boldsymbol{u}(\boldsymbol{x},t) = \boldsymbol{\nabla}\phi + \boldsymbol{\nabla}\times\boldsymbol{\psi}$. Before inserting the displacement expression into the wave equation, introducing the identity $\boldsymbol{\nabla}\times\boldsymbol{\nabla}\times\boldsymbol{A} = \boldsymbol{\nabla}\boldsymbol{\nabla}\cdot\boldsymbol{A} - \boldsymbol{\nabla}\cdot\boldsymbol{\nabla}\boldsymbol{A}$ is useful to be able to split the wave equation into two independent IBVP. The proof is as follows.

$$\begin{aligned}
\boldsymbol{\nabla}\times\boldsymbol{\nabla}\times\boldsymbol{A} = \boldsymbol{\nabla}\times\left(\epsilon_{ijk}\frac{\partial A_k}{\partial x_j}\right) &= \epsilon_{ipq}\epsilon_{ijk}\frac{\partial}{\partial x_q}\frac{\partial A_k}{\partial x_j} \\
&= [\delta_{pj}\delta_{qk} - \delta_{pk}\delta_{qj}]\frac{\partial}{\partial x_q}\frac{\partial A_k}{\partial x_j} \\
&= \delta_{qk}\frac{\partial}{\partial x_q}\frac{\partial A_k}{\partial x_j}\delta_{pj} - \delta_{qj}\frac{\partial}{\partial x_q}\frac{\partial A_k}{\partial x_j}\delta_{pk} \\
&= \frac{\partial}{\partial x_p}\frac{\partial A_k}{\partial x_k} - \frac{\partial}{\partial x_j}\frac{\partial A_p}{\partial x_j} \\
&= \boldsymbol{\nabla}\boldsymbol{\nabla}\cdot\boldsymbol{A} - \boldsymbol{\nabla}\cdot\boldsymbol{\nabla}\boldsymbol{A} \qquad (2.110)
\end{aligned}$$

Recasting the wave equation would, then, yield

$$\boxed{\rho\ddot{\boldsymbol{u}} = (\lambda+2\mu)\boldsymbol{\nabla}\boldsymbol{\nabla}\cdot\boldsymbol{u} - \mu\boldsymbol{\nabla}\times\boldsymbol{\nabla}\times\boldsymbol{u} + \rho\boldsymbol{b}} \qquad (2.111)$$

Decomposing the displacement and external force fields as $\boldsymbol{u}(\boldsymbol{x},t) = \boldsymbol{\nabla}\phi + \boldsymbol{\nabla}\times\boldsymbol{\psi}$ and $\rho\boldsymbol{b} = \boldsymbol{\nabla}\Phi + \boldsymbol{\nabla}\times\boldsymbol{\Psi}$, respectively, recasting (2.111) by inserting (2.110) and utilizing the Lamé's Theorem would yield two independent scalar and vector wave differential equations.

$$\rho\Big(\boldsymbol{\nabla}\ddot{\phi} + \boldsymbol{\nabla}\times\ddot{\boldsymbol{\psi}}\Big) = \boldsymbol{\nabla}(\boldsymbol{\nabla}\cdot\boldsymbol{\nabla}\phi) + \mu\boldsymbol{\nabla}\times\boldsymbol{\nabla}\cdot\boldsymbol{\nabla}\boldsymbol{\psi} + \boldsymbol{\nabla}\Phi + \boldsymbol{\nabla}\times\boldsymbol{\Psi} \qquad (2.112)$$

Rearranging (2.112) yields the differential equations for the displacement potential.

$$\boldsymbol{\nabla}\ddot{\phi} - \alpha^2\boldsymbol{\nabla}(\boldsymbol{\nabla}\cdot\boldsymbol{\nabla}\phi) - \frac{1}{\rho}\boldsymbol{\nabla}\Phi + \boldsymbol{\nabla}\times\ddot{\boldsymbol{\psi}} - \beta^2\boldsymbol{\nabla}\times\boldsymbol{\nabla}\cdot\boldsymbol{\nabla}\boldsymbol{\psi} - \frac{1}{\rho}\boldsymbol{\nabla}\times\boldsymbol{\Psi} = 0 \qquad (2.113)$$

Exploiting the distributive property of $\boldsymbol{\nabla}(\bullet)$ and $\boldsymbol{\nabla}\times(\bullet)$ operators, (2.113) further reduced to following form.

$$\boldsymbol{\nabla}\left(\ddot{\phi} - \alpha^2\boldsymbol{\nabla}^2\phi - \frac{1}{\rho}\Phi\right) + \boldsymbol{\nabla}\times\left(\ddot{\boldsymbol{\psi}} - \beta^2\boldsymbol{\nabla}^2\boldsymbol{\psi} - \frac{1}{\rho}\boldsymbol{\Psi}\right) = 0 \qquad (2.114)$$

(2.114) can be satisfied unless terms in parentheses do not vanish. Hence, two uncoupled partial differential equations are obtained.

$$\boxed{\ddot{\phi} = \alpha^2 \boldsymbol{\nabla}^2 \phi + \frac{1}{\rho}\Phi \qquad \text{and} \qquad \ddot{\boldsymbol{\psi}} = \beta^2 \boldsymbol{\nabla}^2 \boldsymbol{\psi} + \frac{1}{\rho}\boldsymbol{\Psi}} \tag{2.115}$$

where $\alpha^2 = (\lambda + 2\mu)/\rho$ denotes the squared speed of dilatational waves and $\beta^2 = \mu/\rho$ denotes the squared speed of the transverse or shear waves. In order to be able to solve for the scalar and vector potentials, Green's function $\mathfrak{G}(\boldsymbol{x}, t)$ might be found as a first step. Then, assuming that the response of the medium is time-invariant and linear, the superposition of shifted impulse responses under a given external source would yield the solution. To illustrate this, let $\mathfrak{I}(\boldsymbol{x}, t) = \delta(\boldsymbol{x})\delta(t)$ be isotropic, i.e. spherically symmetric, force field so that the directionality of the source is immaterial. Then,

$$\ddot{\mathfrak{G}} = \alpha^2 \boldsymbol{\nabla}^2 \mathfrak{G} + \delta(\boldsymbol{x})\delta(t) \tag{2.116}$$

On the other hand, the external force field can be rewritten by distributing throughout the domain and distributing in time utilizing Dirac distribution.

$$\Phi(\boldsymbol{x}, t) = \int_{-\infty}^{\infty} d\tau \iiint_V \Phi(\boldsymbol{\xi}, \tau)\delta(\boldsymbol{x} - \boldsymbol{\xi})\delta(t - \tau) dV(\boldsymbol{\xi}) \tag{2.117}$$

Inserting the latter equation into the differential equation for scalar potential,

$$\ddot{\phi} = \alpha^2 \boldsymbol{\nabla}^2 \phi + \frac{1}{\rho} \int_{-\infty}^{\infty} d\tau \iiint_V \Phi(\boldsymbol{\xi}, \tau)\delta(\boldsymbol{x} - \boldsymbol{\xi})\delta(t - \tau) dV(\boldsymbol{\xi}) \tag{2.118}$$

Lastly, inserting the former into the last equation,

$$\ddot{\phi} = \alpha^2 \boldsymbol{\nabla}^2 \phi + \frac{1}{\rho} \int_{-\infty}^{\infty} d\tau \iiint_V \Phi(\boldsymbol{\xi}, \tau)\Big[\ddot{\mathfrak{G}}(\boldsymbol{x}, t; \boldsymbol{\xi}, \tau) - \alpha^2 \boldsymbol{\nabla}^2 \mathfrak{G}(\boldsymbol{x}, t; \boldsymbol{\xi}, \tau)\Big] dV(\boldsymbol{\xi}) \tag{2.119}$$

Noting that the gradient and the time derivative are taken with respect to receiver coordinates and time, i.e. $\boldsymbol{x}$ and t, the following expression is obtained.

$$\left[\frac{\partial^2}{\partial t^2} - \alpha^2 \boldsymbol{\nabla}^2\right] \phi(\boldsymbol{x}, t) = \frac{1}{\rho}\left[\frac{\partial^2}{\partial t^2} - \alpha^2 \boldsymbol{\nabla}^2\right] \int_{-\infty}^{\infty} d\tau \iiint_V \Phi(\boldsymbol{\xi}, \tau)\mathfrak{G}(\boldsymbol{x}, t; \boldsymbol{\xi}, \tau) dV(\boldsymbol{\xi}) \tag{2.120}$$

Introducing the d'Alembert operator, or d'Alembertian $\Box_\alpha \coloneqq \partial_{tt} - \alpha^2 \boldsymbol{\nabla}^2$, and rearranging the last equality, the scalar potential can be expressed as the convolution of the source function with the Green's function.

$$\Box_\alpha \left[\phi(\boldsymbol{x}, t) - \frac{1}{\rho} \int_{-\infty}^{\infty} d\tau \iiint_V \Phi(\boldsymbol{\xi}, \tau)\mathfrak{G}(\boldsymbol{x}, t; \boldsymbol{\xi}, \tau) dV(\boldsymbol{\xi})\right] = 0 \tag{2.121}$$

To satisfy the above equality, the term in brackets must vanish. Hence,

$$\boxed{\phi(\boldsymbol{x},t)=\frac{1}{\rho}\int_{-\infty}^{\infty}d\tau\iiint_{V}\Phi(\boldsymbol{\xi},\tau)\mathfrak{G}(\boldsymbol{x},t;\boldsymbol{\xi},\tau)dV(\boldsymbol{\xi})} \tag{2.122}$$

2.4.4 Green's Function for the Scalar Wave Equation

The problem is now reduced to finding Green's function $\mathfrak{G}(\boldsymbol{x},t)$ for the scalar wave equation. Although the derivations are given in a detailed manner, the discussion of the theory of distributions are not presented here. [12], [13], [92] are referred for a detailed discussion of the theory of distributions and the Green's function.

Let us align background Cartesian coordinates such that the origin coincides with the source location. Hence, the position and time coordinates between source and receiver locations become simply $(\boldsymbol{x},t)$. Let us, further, take the spatial Fourier Transform of the scalar wave equation given that the spatial Fourier Transform of Green's function has the following form.

$$\mathscr{F}\{\mathfrak{G}(\boldsymbol{x},t)\}=\hat{\mathfrak{G}}(\boldsymbol{k},t)=\int_{-\infty}^{\infty}dx\int_{-\infty}^{\infty}dy\int_{-\infty}^{\infty}\mathfrak{G}(\boldsymbol{x},t)e^{-i(k_xx+k_yy+k_zz)}dz \tag{2.123}$$

where k_x,k_y,k_z denote the spatial angular frequencies, or angular wavenumbers propagating in x,y, and z directions respectively. Utilizing linearity of d'Alembertian $\square_\alpha$,

$$\begin{aligned}\mathscr{F}\left\{\frac{\partial^2\mathfrak{G}}{\partial t^2}-\alpha^2\boldsymbol{\nabla}^2\mathfrak{G}\right\}&=\frac{\partial^2}{\partial t^2}\mathscr{F}\{\mathfrak{G}(\boldsymbol{x},t)\}-\alpha^2\boldsymbol{\nabla}^2\mathscr{F}\{\mathfrak{G}(\boldsymbol{x},t)\}\\&=\frac{\partial^2\hat{\mathfrak{G}}(\boldsymbol{k},t)}{\partial t^2}-\alpha^2\boldsymbol{\nabla}^2\hat{\mathfrak{G}}(\boldsymbol{k},t)\end{aligned} \tag{2.124}$$

Laplacian of spatially transformed Green's function yields

$$\begin{aligned}\boldsymbol{\nabla}^2\hat{\mathfrak{G}}(\boldsymbol{k},t)&=\left(\frac{\partial^2}{\partial x^2}+\frac{\partial^2}{\partial y^2}+\frac{\partial^2}{\partial z^2}\right)\int_{-\infty}^{\infty}dx\int_{-\infty}^{\infty}dy\int_{-\infty}^{\infty}\mathfrak{G}(\boldsymbol{x},t)e^{-i(k_xx+k_yy+k_zz)}dz\\&=\left(i^2k_x^2+i^2k_y^2+i^2k_z^2\right)\int_{-\infty}^{\infty}dx\int_{-\infty}^{\infty}dy\int_{-\infty}^{\infty}\mathfrak{G}(\boldsymbol{x},t)e^{-i(k_xx+k_yy+k_zz)}dz\\&=-k^2\hat{\mathfrak{G}}(\boldsymbol{k},t)\end{aligned} \tag{2.125}$$

where $\boldsymbol{k}$ is the angular wavenumber vector for which the identity $k^2=k_x^2+k_y^2+k_z^2=\boldsymbol{k}\cdot\boldsymbol{k}$ holds. Then, recognizing that the Fourier Transform of spatial Dirac distribution yields unity resulting. That is,

$$\mathscr{F}\{\delta(\boldsymbol{x})\delta(t)\}=\int_{-\infty}^{\infty}dx\int_{-\infty}^{\infty}dy\int_{-\infty}^{\infty}\delta(\boldsymbol{x})\delta(t)e^{-i(k_xx+k_yy+k_zz)}dz=\delta(t) \tag{2.126}$$

The transformed scalar wave equation takes the form,

$$\frac{\partial^2 \hat{\mathfrak{G}}(\boldsymbol{k},t)}{\partial t^2} + k^2\alpha^2 \hat{\mathfrak{G}}(\boldsymbol{k},t) = \delta(t) \tag{2.127}$$

Assuming $\hat{\mathfrak{G}}(\boldsymbol{k},t)$ has the form $\hat{\mathfrak{G}}(\boldsymbol{k},t) = e^{\varkappa t}$, where $\varkappa$ is function of angular wavenumber vector $\boldsymbol{k}$, i.e. $\varkappa = \hat{\varkappa}(\boldsymbol{k})$, the above equation yields for $t \neq 0$

$$\left[\varkappa^2 + k^2\alpha^2\right] e^{\varkappa t} = 0 \tag{2.128}$$

which is an eigenvalue problem having eigenvalues $\varkappa_{1,2} = \pm ik\alpha$ and corresponding eigenfunctions $\hat{\mathfrak{G}}_1 = K_1 e^{ik\alpha t}$ and $\hat{\mathfrak{G}}_2 = K_2 e^{-ik\alpha t}$ with complex constants K_1, K_2. The superposition of two solutions would then give the solution. Since unknown constants are arbitrary complex numbers, K_2 might be taken as complex conjugate of K_1, that is, $K_2 = \overline{K}_1$ to utilize the identities

$$\cos x = \mathfrak{Re}\left\{e^{ix}\right\} = \frac{1}{2}\left[e^{ix} + e^{-ix}\right] \quad \text{and} \quad \sin x = \mathfrak{Im}\left\{e^{ix}\right\} = \frac{1}{2i}\left[e^{ix} - e^{-ix}\right] \tag{2.129}$$

Hence, solution becomes, with $K_1^{'} = \mathfrak{Re}\{K_1\}$ and $K_2^{'} = \mathfrak{Im}\{K_1\}$

$$\hat{\mathfrak{G}}(\boldsymbol{k},t) = K_1^{'} \cos k\alpha t + K_2^{'} \sin k\alpha t \qquad \forall t \in \mathbb{R}^+ \cup \{0\} \tag{2.130}$$

The last equality implies causality. That means the system or medium through which waves propagate cannot respond before the excitation due to source activity. In other words, the cause always antecedes the response of a system. Hence, $\hat{\mathfrak{G}}(\boldsymbol{x},t)$ is continuous at time $t = 0$, when the source is applied. Then,

$$\hat{\mathfrak{G}}(\boldsymbol{k},t) = K_2^{'} \sin k\alpha t \qquad \forall t \in \mathbb{R}^+ \cup \{0\} \tag{2.131}$$

To find the unknown $K_2^{'}$, let us integrate the transform wave equation over the interval $(t-\epsilon, t+\epsilon)$, around the small neighbourhood of $t = 0$.

$$\frac{\partial \hat{\mathfrak{G}}(\boldsymbol{k},t)}{\partial t}\Big|_{-\epsilon}^{+\epsilon} + k^2\alpha^2 \int_{-\epsilon}^{+\epsilon} \hat{\mathfrak{G}}(\boldsymbol{k},t)dt = 1 \tag{2.132}$$

Taking the limit as $\epsilon \to 0$, and noticing that $\hat{\mathfrak{G}}(\boldsymbol{k},t)$ is continuous at time $t = 0$, we would get

$$\lim_{\epsilon \to 0} \frac{\partial \hat{\mathfrak{G}}(\boldsymbol{k},t)}{\partial t}\Big|_{-\epsilon}^{+\epsilon} = 1 \tag{2.133}$$

implying discontinuity at time $t = 0$ manifesting itself as a unit jump. That means, the response of the system starts to evolve immediately after the source has been applied.

Therefore,

$$\boxed{\hat{\mathfrak{G}}(\boldsymbol{k},t)=\frac{\sin k\alpha t}{k\alpha};\quad \frac{\partial\hat{\mathfrak{G}}(\boldsymbol{k},t)}{\partial t}\Big|_{t=0}=k\alpha K_2^{'}=1;\quad K_2^{'}=\frac{1}{k\alpha}} \tag{2.134}$$

In the final step, to turn back to the spatial domain inverse Fourier transform is applied to the transformed equation.

$$\begin{aligned}\mathscr{F}^{-1}\Big\{\hat{\mathfrak{G}}(\boldsymbol{k},t)\Big\}=\mathfrak{G}(\boldsymbol{x},t)&=\frac{1}{(2\pi)^3}\int_{-\infty}^{\infty}dk_x\int_{-\infty}^{\infty}dk_y\int_{-\infty}^{\infty}\hat{\mathfrak{G}}(\boldsymbol{k},t)e^{i(k_xx+k_yy+k_zz)}dk_z\\&=\frac{1}{(2\pi)^3}\int_{-\infty}^{\infty}dk_x\int_{-\infty}^{\infty}dk_y\int_{-\infty}^{\infty}\hat{\mathfrak{G}}(\boldsymbol{k},t)e^{i\boldsymbol{k}\cdot\boldsymbol{x}}dk_z\end{aligned} \tag{2.135}$$

To be able to evaluate the triple integral, integral variables might be changed to spherical coordinates by defining a sphere having radial coordinate $|\boldsymbol{k}|$ and centered at $|\boldsymbol{k}|=0$, polar angle θ as the angle between radius vector $\boldsymbol{k}$ and position vector $\boldsymbol{x}$ directed along vertical axis such that $\boldsymbol{k}\cdot\boldsymbol{x}=|\boldsymbol{k}||\boldsymbol{x}||cos\theta$, and azimuthal angle φ. Then, differential volume element dV has to be modified to be uniquely mapped onto new coordinate space by $dV=dk_xdk_ydk_z=Jdkd\theta d\varphi$ where J is the Jacobian of the transformation given by $J=k^2\sin\theta dkd\theta d\varphi$.Inserting $\hat{\mathfrak{G}}(\boldsymbol{k},t)$ and changing variables along with the limits would yield

$$\mathfrak{G}(\boldsymbol{x},t)=\frac{1}{(2\pi)^2\alpha}\int_0^{\infty}\sin k\alpha t\,dk\int_0^{\pi}ke^{ik|\boldsymbol{x}|\cos\theta}\sin\theta d\theta \tag{2.136}$$

Integration with respect to polar angle θ along with the introduction of the trigonometric identities given in the preceding section

$$\begin{aligned}\mathfrak{G}(\boldsymbol{x},t)&=\frac{1}{(2\pi)^2\alpha}\int_0^{\infty}\sin k\alpha t\,dk\left[\frac{1}{i|\boldsymbol{x}|}e^{ik|\boldsymbol{x}|\cos\theta}\right]_{\theta=\pi}^{\theta=0}\\&=\frac{1}{(2\pi)^2\alpha|\boldsymbol{x}|}\int_0^{\infty}2\sin k|\boldsymbol{x}|\,\sin k\alpha t\,dk\\&=\frac{2}{(2\pi)^2\alpha|\boldsymbol{x}|}\int_0^{\infty}\frac{\left(e^{ik|\boldsymbol{x}|}-e^{-ik|\boldsymbol{x}|}\right)}{2i}\frac{\left(e^{ik\alpha t}-e^{-ik\alpha t}\right)}{2i}dk\\&=\frac{1}{(2\pi)^2\alpha|\boldsymbol{x}|}\int_0^{\infty}\left(\frac{e^{ik(|\boldsymbol{x}|-\alpha t)}+e^{-ik(|\boldsymbol{x}|-\alpha t)}}{2}-\frac{e^{ik(|\boldsymbol{x}|+\alpha t)}+e^{-ik(|\boldsymbol{x}|+\alpha t)}}{2}\right)dk\\&=\frac{1}{(2\pi)^2\alpha|\boldsymbol{x}|}\int_0^{\infty}[\cos k(|\boldsymbol{x}|-\alpha t)-\cos k(|\boldsymbol{x}|+\alpha t)]dk\end{aligned} \tag{2.137}$$

Let us investigate the Fourier Transform of $\delta(x-x_0)$ where x_0 is an arbitrary shift.

$$\mathscr{F}\{\delta(x-x_0)\}=\int_{-\infty}^{\infty}e^{-ikx}\delta(x-x_0)dx=e^{-ikx_0} \tag{2.138}$$

Now, if the Dirac Delta function is rewritten in terms of its Fourier Transform

$$\delta(x-x_0)=\frac{1}{2\pi}\int_{-\infty}^{\infty}e^{-ikx_0}e^{ikx}dk=\frac{1}{2\pi}\int_{-\infty}^{\infty}e^{ik(x-x_0)}dk \tag{2.139}$$

Since the source signal that we are dealing with is a real signal, taking the real part of the right hand side and using the evenness of the cosine function,

$$\delta(x-x_0)=\frac{1}{2\pi}\int_{-\infty}^{\infty}\mathfrak{Re}\left\{e^{ik(x-x_0)}\right\}dk=\frac{1}{\pi}\int_{0}^{\infty}\cos k(x-x_0)dk \tag{2.140}$$

The integral in the last equality turns out to be a summation of two shifted delta functions, namely, $\delta(|\boldsymbol{x}|-\alpha t)$ and $-\delta(|\boldsymbol{x}|+\alpha t)$. Hence, Green's function $\mathfrak{G}(\boldsymbol{x},t)$ is found as follows.

$$\mathfrak{G}(\boldsymbol{x},t)=\frac{1}{4\pi\alpha|\boldsymbol{x}|}[\delta(|\boldsymbol{x}|-\alpha t)-\delta(|\boldsymbol{x}|+\alpha t)] \tag{2.141}$$

It should be noted that the second delta function is always zero since the argument $|\boldsymbol{x}|+\alpha t$ is always positive as negative t values imply violation of the causality principle meaning that the response precedes its cause. Hence, utilizing the evenness and scaling properties of the delta function; i.e., $\delta(x)=\delta(-x)$ and $\delta(\alpha x)=\alpha^{-1}\delta(x)$

$$\boxed{\mathfrak{G}(\boldsymbol{x},t)=\frac{1}{4\pi\alpha}\frac{\delta(|\boldsymbol{x}|-\alpha t)}{|\boldsymbol{x}|}=\frac{1}{4\pi\alpha}\frac{\delta(\alpha t-|\boldsymbol{x}|)}{|\boldsymbol{x}|}=\frac{1}{4\pi\alpha^2}\frac{\delta\big(t-|\boldsymbol{x}|/\alpha\big)}{|\boldsymbol{x}|}} \tag{2.142}$$

Further generalization might be made by shifting source coordinates spatially by $\boldsymbol{\xi}$ and shifting in time by τ, yielding $\mathfrak{G}(\boldsymbol{x},t;\boldsymbol{\xi},\tau)$

$$\boxed{\mathfrak{G}(\boldsymbol{x},t;\boldsymbol{\xi},\tau)=\frac{1}{4\pi\alpha^2}\frac{\delta\big(t-\tau-|\boldsymbol{x}-\boldsymbol{\xi}|/\alpha\big)}{|\boldsymbol{x}-\boldsymbol{\xi}|}} \tag{2.143}$$

Having Green's function for the scalar potential at hand, a solution to elastic wave equation can be constructed systematically by first finding dyadic Green's function $\tilde{\mathfrak{G}}$ in which responses to unit impulses applied in each orthogonal direction are embedded. Then, the convolution of dyadic Green's function with an arbitrary concentrated force, possibly varying with time, would give the total displacement field $\boldsymbol{u}(\boldsymbol{x},t)$ at the observation point. Before moving on to the construction of dyadic Green's function, however, a solution to Poisson's equation, i.e. static solution of scalar potential given in equation, might be obtained to utilize Helmholtz's Decomposition in finding the source potentials Φ and $\boldsymbol{\Psi}$. Inserting the scalar Green's function into the scalar

potential equation,

$$\begin{aligned}\phi(\boldsymbol{x},t) &= \frac{1}{4\pi\alpha^2\rho}\int_{-\infty}^{\infty} d\tau \iiint_V \Phi(\boldsymbol{\xi},\tau)\frac{\delta\big(t-\tau-|\boldsymbol{x}-\boldsymbol{\xi}|/\alpha\big)}{|\boldsymbol{x}-\boldsymbol{\xi}|}dV(\boldsymbol{\xi}) \\ &= \frac{1}{4\pi\alpha^2\rho}\iiint_V \frac{\Phi\big(\boldsymbol{\xi},t-|\boldsymbol{x}-\boldsymbol{\xi}|/\alpha\big)}{|\boldsymbol{x}-\boldsymbol{\xi}|}dV(\boldsymbol{\xi}) \end{aligned} \tag{2.144}$$

If the scalar field is time independent, then the governing differential equation and its solution obtained by removing the time dependency from the above solution, have the following form.

$$\boldsymbol{\nabla}^2\phi = -\frac{1}{\alpha^2\rho}\Phi \quad \text{where } \phi(\boldsymbol{x}) = -\frac{1}{4\pi\alpha^2\rho}\iiint_V \frac{\Phi(\boldsymbol{\xi})}{|\boldsymbol{x}-\boldsymbol{\xi}|}dV(\boldsymbol{\xi}) \tag{2.145}$$

Let U, $\boldsymbol{V}$ be scalar and vector fields, and let $\boldsymbol{F}$ be a static source vector for the vector Poisson's equation $\boldsymbol{\nabla}^2\boldsymbol{W} = \boldsymbol{F}$, where $\boldsymbol{W}(\boldsymbol{x})$ is a static vector potential to be solved for. Utilizing the vector calculus identities, Poisson's equation can be transformed to $\boldsymbol{\nabla}\boldsymbol{\nabla}\cdot\boldsymbol{W} - \boldsymbol{\nabla}\times\boldsymbol{\nabla}\times\boldsymbol{W} = \boldsymbol{F}$. Then, defining $U \coloneqq \boldsymbol{\nabla}\cdot\boldsymbol{W}$ and $\boldsymbol{V} \coloneqq -\boldsymbol{\nabla}\times\boldsymbol{W}$, the source vector can be written as $\boldsymbol{\nabla}U + \boldsymbol{\nabla}\times\boldsymbol{V} = \boldsymbol{F}$. To find the vector potential $\boldsymbol{W}(\boldsymbol{x})$, solution to the scalar field with $\alpha^2\rho$ term taken as unity can be utilized as Laplacian operator $\boldsymbol{\nabla}^2$ in cartesian coordinates yields three independent differential equations for each coordinate, i.e. $\boldsymbol{\nabla}^2\boldsymbol{W} = \boldsymbol{\nabla}^2W_1\boldsymbol{e}_1 + \boldsymbol{\nabla}^2W_2\boldsymbol{e}_2 + \boldsymbol{\nabla}^2W_3\boldsymbol{e}_3 = F_1\boldsymbol{e}_1 + F_2\boldsymbol{e}_2 + F_3\boldsymbol{e}_3$. Therefore,

$$\boldsymbol{W}(\boldsymbol{x}) = -\frac{1}{4\pi}\iiint_V \frac{\boldsymbol{F}(\boldsymbol{\xi})}{|\boldsymbol{x}-\boldsymbol{\xi}|}dV(\boldsymbol{\xi}) \quad \text{or} \quad W_i(\boldsymbol{x}) = -\frac{1}{4\pi}\iiint_V \frac{F_i(\boldsymbol{\xi})}{|\boldsymbol{x}-\boldsymbol{\xi}|}dV(\boldsymbol{\xi}) \tag{2.146}$$

where $\forall i \in \{1,2,3\}$. Now, dyadic Green's function can be constructed by applying unit impulse in the direction of each cartesian coordinate sequentially. Let $\boldsymbol{F}(\boldsymbol{x},t) = \delta(t)\delta(\boldsymbol{x})\boldsymbol{e}_1$ be a unit impulse applied in x_1 direction. Then, the vector potential $\boldsymbol{W}(\boldsymbol{x},t)$ can be written as follows while noticing the decoupling of time and spatial coordinates.

$$\boldsymbol{W}(\boldsymbol{x},t) = -\frac{1}{4\pi}\iiint_V \frac{\delta(t)\delta(\boldsymbol{\xi})}{|\boldsymbol{x}-\boldsymbol{\xi}|}\boldsymbol{e}_1\,dV(\boldsymbol{\xi}) = -\frac{\delta(t)}{4\pi|\boldsymbol{x}|}\boldsymbol{e}_1 \tag{2.147}$$

Employing Helmholtz's Decomposition set forth in the preceding discussion, the source term $\boldsymbol{F}(\boldsymbol{x},t)$ can be additively decomposed into irrotational and solenoidal parts as $\boldsymbol{F}(\boldsymbol{x},t) = \boldsymbol{\nabla}\Phi + \boldsymbol{\nabla}\times\boldsymbol{\Psi}$ where $\Phi(\boldsymbol{x},t) = \boldsymbol{\nabla}\cdot\boldsymbol{W}$, and $\boldsymbol{\Psi}(\boldsymbol{x},t) = -\boldsymbol{\nabla}\times\boldsymbol{W}$. Using the vector potential expression $\boldsymbol{W}(\boldsymbol{x},t)$, the scalar source field $\Phi(\boldsymbol{x},t)$ is found as,

$$\Phi(\boldsymbol{x},t) = \boldsymbol{\nabla}\cdot\boldsymbol{W} = -\frac{\delta(t)}{4\pi}\frac{\partial}{\partial x_1}\frac{1}{|\boldsymbol{x}|} \tag{2.148}$$

Similarly, the vector source field $\boldsymbol{\Psi}(\boldsymbol{x},t)$ can be expressed as

$$\begin{aligned}\boldsymbol{\Psi}(\boldsymbol{x},t) = -\boldsymbol{\nabla}\times\boldsymbol{W} =& \epsilon_{ijk}\partial_j W_k \\ =& -\left(\frac{\partial W_3}{\partial x_2}-\frac{\partial W_2}{\partial x_3}\right)\boldsymbol{e}_1 - \left(\frac{\partial W_1}{\partial x_3}-\frac{\partial W_3}{\partial x_1}\right)\boldsymbol{e}_2 \\ & -\left(\frac{\partial W_2}{\partial x_1}-\frac{\partial W_1}{\partial x_2}\right)\boldsymbol{e}_3 \\ =& -\left(0,\, -\frac{\delta(t)}{4\pi}\frac{\partial}{\partial x_3}\frac{1}{|\boldsymbol{x}|},\, \frac{\partial}{\partial x_2}\frac{1}{|\boldsymbol{x}|}\right)\end{aligned} \tag{2.149}$$

Employing the solution of scalar potential field, the scalar and vector potential fields that are to be used to construct total displacement field $\boldsymbol{u}(\boldsymbol{x},t)$ would finally be obtained. To illustrate the solution steps, the scalar field will be used as the construction of vector potential follows identical steps but for each direction.

$$\phi(\boldsymbol{x},t) = -\frac{1}{(4\pi\alpha)^2\rho}\iiint_V \frac{\delta\big(t-|\boldsymbol{x}-\boldsymbol{\xi}|/\alpha\big)}{|\boldsymbol{x}-\boldsymbol{\xi}|}\frac{\partial}{\partial\xi_1}\frac{1}{|\boldsymbol{\xi}|}dV(\boldsymbol{\xi}) \tag{2.150}$$

The volume integral might be evaluated via potential theory. If the distance travelled by the waves throughout the volume $V(\boldsymbol{\xi})$, that is, $|\boldsymbol{x}-\boldsymbol{\xi}|$, during time interval τ is rewritten as $|\boldsymbol{x}-\boldsymbol{\xi}| = \alpha\tau$, the integral can be expressed as follows.

$$\begin{aligned}\phi(\boldsymbol{x},t) &= -\frac{1}{(4\pi\alpha)^2\rho}\int_0^\infty \frac{\delta(t-\tau)}{\alpha\tau}\alpha d\tau \oiint_S \frac{\partial}{\partial\xi_1}\frac{1}{|\boldsymbol{\xi}|}dS(\boldsymbol{\xi}) \\ &= -\frac{1}{(4\pi\alpha)^2\rho}\int_0^\infty \frac{\delta(t-\tau)}{\tau}d\tau \oiint_S \frac{\partial}{\partial\xi_1}\frac{1}{|\boldsymbol{\xi}|}dS(\boldsymbol{\xi})\end{aligned} \tag{2.151}$$

The surface integral can be taught of as finding the electric field acting on a fictitious electric charge in the $\boldsymbol{e}_1$ direction due to electric potential generated by distributed electric charges over a spherical surface. Similarly, this might be a gravitational field due to gravitational potential as well. Now, let us introduce the coordinate $\boldsymbol{\eta}$ at which the potential is to be calculated. Let us also introduce the distance to the surface $R \coloneqq |\boldsymbol{\xi}-\boldsymbol{\eta}|$ and the distance to the center of the sphere $r \coloneqq |\boldsymbol{x}-\xi|$, and let θ be the angle between the vectors $\boldsymbol{x}-\boldsymbol{\eta}$ and $\boldsymbol{x}-\boldsymbol{\xi}$. Then, the partial derivative operator can be taken outside the integral noticing that

$$\frac{\partial}{\partial\xi_1}\frac{1}{R} = \frac{\partial R^{-1}}{\partial R}\frac{\partial R}{\partial\xi_1} = -\frac{\partial R^{-1}}{\partial R}\frac{\partial R}{\partial\eta_1} = -\frac{\partial}{\partial\eta_1}\frac{1}{R} \tag{2.152}$$

Now, defining the infinitesimal surface area element as a shell element having thickness $\alpha\tau$ and average perimeter $2\pi\alpha\tau\sin\theta\, d\theta$, surface integral can be evaluated as follows.

$$-\frac{\partial}{\partial\eta_1}\oiint_S \frac{dS}{R} = -\frac{\partial}{\partial\eta_1}\left(2\pi\alpha^2\tau^2\int_0^\pi \frac{\sin\theta}{R}\,d\theta\right) \tag{2.153}$$

Furthermore, using the law of cosines, the relationship between R and θ is obtained to further transform the integral as the angle θ also depends on R.

$$R^2 = r^2 + \alpha^2\tau^2 - 2r\alpha\tau\cos\theta \qquad \text{and} \qquad 2R\,dR = 2r\alpha\tau\sin\theta\,d\theta \tag{2.154}$$

Inserting (2.154) into (2.153) and recasting,

$$-\frac{\partial}{\partial\eta_1}\left(\frac{2\pi\alpha\tau}{r}\int_{|r-\alpha t|}^{|r+\alpha t|} dR = \begin{cases} 4\pi\alpha\tau & \text{if } \tau > r/\alpha \\ \dfrac{4\pi\alpha^2\tau^2}{r} & \text{if } \tau < r/\alpha \end{cases}\right) \tag{2.155}$$

Since there is no dependency on the distance term inside the sphere there would be no net force acting on a particle as they cancel out each other. Therefore , the force component in the $\boldsymbol{e}_1$ direction while $\boldsymbol{\eta} \to \mathbf{0}$ can be written as,

$$-\frac{\partial}{\partial\eta_1}\frac{4\pi\alpha^2\tau^2}{r}\bigg|_{\boldsymbol{\eta}=\mathbf{0}} = 4\pi\alpha^2\tau^2\frac{\partial}{\partial x_1}\frac{1}{|\boldsymbol{x}|} \tag{2.156}$$

Inserting this into the scalar potential

$$\phi(\boldsymbol{x},t) = -\frac{1}{4\pi\rho}\left(\frac{\partial}{\partial x_1}\frac{1}{|\boldsymbol{x}|}\right)\int_0^{|\boldsymbol{x}|/\alpha}\tau\delta(t-\tau)d\tau \tag{2.157}$$

Similarly, the vector potential can be calculated as

$$\boldsymbol{\Psi}(\boldsymbol{x},t) = -\frac{1}{4\pi\rho}\left(0,\, -\frac{\partial}{\partial x_3}\frac{1}{|\boldsymbol{x}|},\, \frac{\partial}{\partial x_2}\frac{1}{|\boldsymbol{x}|}\right)\int_0^{|\boldsymbol{x}|/\beta}\tau\delta(t-\tau)d\tau \tag{2.158}$$

With the scalar and vector Lamé potentials at hand, the displacement field $\boldsymbol{u}(\boldsymbol{x},t)$ due to unit impulse directed along $\boldsymbol{e}_1$ direction, which constitutes the first column of the dyadic Green's function $\mathfrak{G}(\boldsymbol{x},t)$, can be found invoking Lamé's Theorem. That is,

$$\boldsymbol{u}(\boldsymbol{x},t) = \boldsymbol{\nabla}\phi + \boldsymbol{\nabla}\times\boldsymbol{\Psi} \tag{2.159}$$

In what follows, Leibniz integral rule is explicitly used, that is,

$$\frac{d}{dx}\left(\int_{h(x)}^{g(x)} f(\tau)d\tau\right) = f(g(x))g'(x) - f(h(x))h'(x) \tag{2.160}$$

Denoting the ith coordinate as x_i, the irrotational part of the displacement field is

given by

$$\begin{aligned}\boldsymbol{\nabla}\phi = &-\frac{1}{4\pi\rho}\left[\frac{\partial^2}{\partial x_1\partial x_1}\frac{1}{|\boldsymbol{x}|}\int_0^{|\boldsymbol{x}|/\alpha}\tau\delta(t-\tau)d\tau + \frac{|\boldsymbol{x}|}{\alpha^2}\frac{\partial|\boldsymbol{x}|}{\partial x_1}\frac{\partial}{\partial x_1}\frac{1}{|\boldsymbol{x}|}\delta\big(t-|\boldsymbol{x}|/\alpha\big)\right]\boldsymbol{e}_1\\ &-\frac{1}{4\pi\rho}\left[\frac{\partial^2}{\partial x_2\partial x_1}\frac{1}{|\boldsymbol{x}|}\int_0^{|\boldsymbol{x}|/\alpha}\tau\delta(t-\tau)d\tau + \frac{|\boldsymbol{x}|}{\alpha^2}\frac{\partial|\boldsymbol{x}|}{\partial x_2}\frac{\partial}{\partial x_1}\frac{1}{|\boldsymbol{x}|}\delta\big(t-|\boldsymbol{x}|/\alpha\big)\right]\boldsymbol{e}_2\\ &-\frac{1}{4\pi\rho}\left[\frac{\partial^2}{\partial x_3\partial x_1}\frac{1}{|\boldsymbol{x}|}\int_0^{|\boldsymbol{x}|/\alpha}\tau\delta(t-\tau)d\tau + \frac{|\boldsymbol{x}|}{\alpha^2}\frac{\partial|\boldsymbol{x}|}{\partial x_3}\frac{\partial}{\partial x_1}\frac{1}{|\boldsymbol{x}|}\delta\big(t-|\boldsymbol{x}|/\alpha\big)\right]\boldsymbol{e}_3\end{aligned} \tag{2.161}$$

Similarly, the solenoidal part of the displacement field is given by

$$\begin{aligned}\boldsymbol{\nabla}\times\boldsymbol{\Psi} = &-\frac{1}{4\pi\rho}\left[\frac{\partial^2}{\partial x_2\partial x_2}\frac{1}{|\boldsymbol{x}|}\int_0^{|\boldsymbol{x}|/\beta}\tau\delta(t-\tau)d\tau + \frac{|\boldsymbol{x}|}{\beta^2}\frac{\partial|\boldsymbol{x}|}{\partial x_2}\frac{\partial}{\partial x_2}\frac{1}{|\boldsymbol{x}|}\delta\big(t-|\boldsymbol{x}|/\beta\big)\right]\boldsymbol{e}_1\\ &-\frac{1}{4\pi\rho}\left[\frac{\partial^2}{\partial x_3\partial x_3}\frac{1}{|\boldsymbol{x}|}\int_0^{|\boldsymbol{x}|/\beta}\tau\delta(t-\tau)d\tau + \frac{|\boldsymbol{x}|}{\beta^2}\frac{\partial|\boldsymbol{x}|}{\partial x_3}\frac{\partial}{\partial x_3}\frac{1}{|\boldsymbol{x}|}\delta\big(t-|\boldsymbol{x}|/\beta\big)\right]\boldsymbol{e}_1\\ &+\frac{1}{4\pi\rho}\left[\frac{\partial^2}{\partial x_2\partial x_1}\frac{1}{|\boldsymbol{x}|}\int_0^{|\boldsymbol{x}|/\beta}\tau\delta(t-\tau)d\tau + \frac{|\boldsymbol{x}|}{\beta^2}\frac{\partial|\boldsymbol{x}|}{\partial x_1}\frac{\partial}{\partial x_2}\frac{1}{|\boldsymbol{x}|}\delta\big(t-|\boldsymbol{x}|/\beta\big)\right]\boldsymbol{e}_2\\ &+\frac{1}{4\pi\rho}\left[\frac{\partial^2}{\partial x_3\partial x_1}\frac{1}{|\boldsymbol{x}|}\int_0^{|\boldsymbol{x}|/\beta}\tau\delta(t-\tau)d\tau + \frac{|\boldsymbol{x}|}{\beta^2}\frac{\partial|\boldsymbol{x}|}{\partial x_1}\frac{\partial}{\partial x_3}\frac{1}{|\boldsymbol{x}|}\delta\big(t-|\boldsymbol{x}|/\beta\big)\right]\boldsymbol{e}_3\end{aligned} \tag{2.162}$$

To superimpose contributions from both parts, the integral term in the direction of the applied force can be further reduced by noticing the relationship

$$\frac{\partial^2}{\partial x_1\partial x_1}\frac{1}{|\boldsymbol{x}|} = \boldsymbol{\nabla}^2\frac{1}{|\boldsymbol{x}|} - \frac{\partial^2}{\partial x_2\partial x_2}\frac{1}{|\boldsymbol{x}|} - \frac{\partial^2}{\partial x_3\partial x_3}\frac{1}{|\boldsymbol{x}|} \quad \text{where } \boldsymbol{\nabla}^2\frac{1}{|\boldsymbol{x}|} = -4\pi\delta(\boldsymbol{x}) \tag{2.163}$$

The latter follows from Poisson's equation given in the preceding chapter in which Green's function, under the assumption of unit propagation speed and density, is found to be

$$\mathfrak{G}(\boldsymbol{x}) = -\frac{1}{4\pi}\frac{\delta(\boldsymbol{x})}{|\boldsymbol{x}|} \qquad \text{and} \qquad \boldsymbol{\nabla}^2\mathfrak{G}(\boldsymbol{x}) = \delta(\boldsymbol{x}) \tag{2.164}$$

Therefore, unless the radial distance to the receiver is not zero, the laplacian of the reciprocal of distance would always be zero. Hence, the contribution from the convolution integral due to applied force in $\boldsymbol{e}_1$ direction becomes

$$\begin{aligned}u_1^{I_\alpha^\beta} \coloneqq &-\frac{1}{4\pi\rho}\frac{\partial^2}{\partial x_1\partial x_1}\frac{1}{|\boldsymbol{x}|}\int_0^{|\boldsymbol{x}|/\alpha}\tau\delta(t-\tau)d\tau\\ &-\frac{1}{4\pi\rho}\left(\boldsymbol{\nabla}^2\frac{1}{|\boldsymbol{x}|} - \frac{\partial^2}{\partial x_1\partial x_1}\frac{1}{|\boldsymbol{x}|}\right)\int_0^{|\boldsymbol{x}|/\beta}\tau\delta(t-\tau)\end{aligned} \tag{2.165}$$

Recasting (2.165) employing (2.163)then yields the following.

$$u_1^{I_\alpha^\beta} = \frac{1}{4\pi\rho}\left(\frac{\partial^2}{\partial x_1 \partial x_1}\frac{1}{|\boldsymbol{x}|}\right)\int_{|\boldsymbol{x}|/\alpha}^{|\boldsymbol{x}|/\beta} \tau\delta(t-\tau)d\tau \tag{2.166}$$

Secondly, contributions from time-shifted delta distributions might also be put in a form that can be generalized for arbitrarily oriented sources. Let us consider the following derivative

$$\frac{\partial}{\partial x_1}\frac{1}{|\boldsymbol{x}|} = -\frac{1}{|\boldsymbol{x}|^2}\frac{\partial|\boldsymbol{x}|}{\partial x_1} \quad \text{where } \frac{\partial|\boldsymbol{x}|}{\partial x_1} = \frac{x_1}{|\boldsymbol{x}|} = \gamma_1 \tag{2.167}$$

where γ_1 is the direction cosine between the distance vector $\boldsymbol{x}$ and the coordinate axis x_1. It follows that

$$\frac{\partial|\boldsymbol{x}|}{\partial x_1}\frac{\partial|\boldsymbol{x}|}{\partial x_1} + \frac{\partial|\boldsymbol{x}|}{\partial x_2}\frac{\partial|\boldsymbol{x}|}{\partial x_2} + \frac{\partial|\boldsymbol{x}|}{\partial x_3}\frac{\partial|\boldsymbol{x}|}{\partial x_3} = \gamma_1^2 + \gamma_2^2 + \gamma_3^2 = 1 \tag{2.168}$$

Similar to the previous step, the latter equality can be written in terms of x_1 coordinate. That is,

$$\frac{\partial|\boldsymbol{x}|}{\partial x_2}\frac{\partial|\boldsymbol{x}|}{\partial x_2} + \frac{\partial|\boldsymbol{x}|}{\partial x_3}\frac{\partial|\boldsymbol{x}|}{\partial x_3} = 1 - \frac{\partial|\boldsymbol{x}|}{\partial x_1}\frac{\partial|\boldsymbol{x}|}{\partial x_1} \tag{2.169}$$

Inserting this expression into (2.159), contribution from the convolution integral in $\boldsymbol{e}_1$ direction becomes

$$\begin{aligned} u_1^{\delta_\alpha^\beta} \coloneqq\ & \frac{1}{4\pi\rho\alpha^2|\boldsymbol{x}|}\left(\frac{\partial|\boldsymbol{x}|}{\partial x_1}\frac{\partial|\boldsymbol{x}|}{\partial x_1}\right)\delta\big(t-|\boldsymbol{x}|/\alpha\big) \\ & + \frac{1}{4\pi\rho\beta^2|\boldsymbol{x}|}\left(1-\frac{\partial|\boldsymbol{x}|}{\partial x_1}\frac{\partial|\boldsymbol{x}|}{\partial x_1}\right)\delta\big(t-|\boldsymbol{x}|/\beta\big) \end{aligned} \tag{2.170}$$

Then, the total displacement field due to an impulsive force applied in $\boldsymbol{e}_1$ direction can be expressed as

$$\begin{aligned} \boldsymbol{u}(\boldsymbol{x},t) &= \boldsymbol{u}^{I_\alpha^\beta}(\boldsymbol{x},t) + \boldsymbol{u}^{\delta_\alpha^\beta}(\boldsymbol{x},t) \\ &= \left(u_1^{I_\alpha^\beta} + u_1^{\delta_\alpha^\beta}\right)\boldsymbol{e}_1 + \left(u_2^{I_\alpha^\beta} + u_2^{\delta_\alpha^\beta}\right)\boldsymbol{e}_2 + \left(u_3^{I_\alpha^\beta} + u_3^{\delta_\alpha^\beta}\right)\boldsymbol{e}_3 \end{aligned} \tag{2.171}$$

where components of the displacement field $\boldsymbol{u}(\boldsymbol{x},t)$ are given by

$$u_1(\boldsymbol{x},t) = u_1^{I_\alpha^\beta}(\boldsymbol{x},t) + u_1^{\delta_\alpha^\beta}(\boldsymbol{x},t) = \frac{1}{4\pi\rho}\left(\frac{\partial^2}{\partial x_1 \partial x_1}\frac{1}{|\boldsymbol{x}|}\right)\int_{|\boldsymbol{x}|/\alpha}^{|\boldsymbol{x}|/\beta} \tau\delta(t-\tau)d\tau + \frac{1}{4\pi\rho\alpha^2|\boldsymbol{x}|}\left(\frac{\partial|\boldsymbol{x}|}{\partial x_1}\frac{\partial|\boldsymbol{x}|}{\partial x_1}\right)\delta\big(t-|\boldsymbol{x}|/\alpha\big) + \frac{1}{4\pi\rho\beta^2|\boldsymbol{x}|}\left(1-\frac{\partial|\boldsymbol{x}|}{\partial x_1}\frac{\partial|\boldsymbol{x}|}{\partial x_1}\right)\delta\big(t-|\boldsymbol{x}|/\beta\big) \tag{2.172a}$$

$$u_2(\boldsymbol{x},t) = u_2^{I_\alpha^\beta}(\boldsymbol{x},t) + u_2^{\delta_\alpha^\beta}(\boldsymbol{x},t) = \frac{1}{4\pi\rho}\left(\frac{\partial^2}{\partial x_2 \partial x_1}\frac{1}{|\boldsymbol{x}|}\right)\int_{|\boldsymbol{x}|/\alpha}^{|\boldsymbol{x}|/\beta} \tau\delta(t-\tau)d\tau + \frac{1}{4\pi\rho\alpha^2|\boldsymbol{x}|}\left(\frac{\partial|\boldsymbol{x}|}{\partial x_2}\frac{\partial|\boldsymbol{x}|}{\partial x_1}\right)\delta\big(t-|\boldsymbol{x}|/\alpha\big) + \frac{1}{4\pi\rho\beta^2|\boldsymbol{x}|}\left(-\frac{\partial|\boldsymbol{x}|}{\partial x_2}\frac{\partial|\boldsymbol{x}|}{\partial x_1}\right)\delta\big(t-|\boldsymbol{x}|/\beta\big) \tag{2.172b}$$

$$u_3(\boldsymbol{x},t) = u_3^{I_\alpha^\beta}(\boldsymbol{x},t) + u_3^{\delta_\alpha^\beta}(\boldsymbol{x},t) = \frac{1}{4\pi\rho}\left(\frac{\partial^2}{\partial x_3 \partial x_1}\frac{1}{|\boldsymbol{x}|}\right)\int_{|\boldsymbol{x}|/\alpha}^{|\boldsymbol{x}|/\beta} \tau\delta(t-\tau)d\tau + \frac{1}{4\pi\rho\alpha^2|\boldsymbol{x}|}\left(\frac{\partial|\boldsymbol{x}|}{\partial 3_2}\frac{\partial|\boldsymbol{x}|}{\partial x_1}\right)\delta\big(t-|\boldsymbol{x}|/\alpha\big) + \frac{1}{4\pi\rho\beta^2|\boldsymbol{x}|}\left(-\frac{\partial|\boldsymbol{x}|}{\partial x_3}\frac{\partial|\boldsymbol{x}|}{\partial x_1}\right)\delta\big(t-|\boldsymbol{x}|/\beta\big) \tag{2.172c}$$

Introducing Kronecker's delta δ_{ij} and denoting δ_{i1} for the contribution in $\boldsymbol{e}_1$ direction, the displacement field can be written in a more compact form

$$\begin{aligned} u_i(\boldsymbol{x},t) &= u_i^{I_\alpha^\beta}(\boldsymbol{x},t) + u_i^{\delta_\alpha^\beta}(\boldsymbol{x},t) \\ &= \frac{1}{4\pi\rho}\left(\frac{\partial^2}{\partial x_i \partial x_1}\frac{1}{|\boldsymbol{x}|}\right)\int_{|\boldsymbol{x}/\alpha|}^{|\boldsymbol{x}|/\beta} \tau\delta(t-\tau)d\tau \\ &\quad + \frac{1}{4\pi\rho\alpha^2|\boldsymbol{x}|}\left(\frac{\partial|\boldsymbol{x}|}{\partial x_i}\frac{\partial|\boldsymbol{x}|}{\partial x_1}\right)\delta\big(t-|\boldsymbol{x}|/\alpha\big) \\ &\quad + \frac{1}{4\pi\rho\beta^2|\boldsymbol{x}|}\left(\delta_{i1}-\frac{\partial|\boldsymbol{x}|}{\partial x_i}\frac{\partial|\boldsymbol{x}|}{\partial x_1}\right)\delta\big(t-|\boldsymbol{x}|/\beta\big) \end{aligned} \tag{2.173}$$

This constitutes the first column of dyadic Green's function $\mathfrak{G}_{i1}$. Generalizing the direction through which the impulsive source is to be applied, and embedding the resulting displacement fields into the dyadic Green's function $\mathfrak{G}$, complete information regarding the displacement field resulting from an impulse applied in x_j direction can

be obtained.

$$\mathfrak{G}_{ij}(\boldsymbol{x},t) = \frac{1}{4\pi\rho}\left(\frac{\partial^2}{\partial x_i \partial x_j}\frac{1}{|\boldsymbol{x}|}\right)\int_{|\boldsymbol{x}/\alpha|}^{|\boldsymbol{x}|/\beta} \tau\delta(t-\tau)d\tau + \frac{1}{4\pi\rho\alpha^2|\boldsymbol{x}|}\left(\frac{\partial|\boldsymbol{x}|}{\partial x_i}\frac{\partial|\boldsymbol{x}|}{\partial x_j}\right)\delta\big(t-|\boldsymbol{x}|/\alpha\big) + \frac{1}{4\pi\rho\beta^2|\boldsymbol{x}|}\left(\delta_{ij}-\frac{\partial|\boldsymbol{x}|}{\partial x_i}\frac{\partial|\boldsymbol{x}|}{\partial x_j}\right)\delta\big(t-|\boldsymbol{x}|/\beta\big) \tag{2.174}$$

Evaluating the double gradient term using direction cosines γ_i and γ_j and Kronecker's delta δ_{ij}

$$\frac{\partial^2}{\partial x_i \partial x_j}\frac{1}{|\boldsymbol{x}|} = \frac{\partial}{\partial x_i}\left(\frac{\partial}{\partial|\boldsymbol{x}|}|\boldsymbol{x}|^{-1}\frac{\partial|\boldsymbol{x}|}{\partial x_j}\right) = \frac{\partial}{\partial x_i}\left(-|\boldsymbol{x}|^{-2}\frac{\partial|\boldsymbol{x}|}{\partial x_j}\right) \tag{2.175}$$

where the last equation is evaluated as

$$\frac{\partial}{\partial x_i}\left(-|\boldsymbol{x}|^{-2}\frac{\partial|\boldsymbol{x}|}{\partial x_j}\right) = -\left(\frac{\partial}{\partial x_i}|\boldsymbol{x}|^{-2}\right)\frac{\partial|\boldsymbol{x}|}{\partial x_j} - |\boldsymbol{x}|^{-2}\frac{\partial}{\partial x_i}\frac{\partial|\boldsymbol{x}|}{\partial x_j} \tag{2.176}$$

in which the first term on the right hand side is expressed as

$$-\left(\frac{\partial}{\partial x_i}|\boldsymbol{x}|^{-2}\right)\frac{\partial|\boldsymbol{x}|}{\partial x_j} = 2|\boldsymbol{x}|^{-3}\frac{\partial|\boldsymbol{x}|}{\partial x_i}\frac{\partial|\boldsymbol{x}|}{\partial x_j} = 2|\boldsymbol{x}|^{-3}\gamma_i\gamma_j \tag{2.177}$$

and similarly, the second term is given by

$$\begin{aligned} -|\boldsymbol{x}|^{-2}\frac{\partial}{\partial x_i}\frac{\partial|\boldsymbol{x}|}{\partial x_j} &= -|\boldsymbol{x}|^{-2}\frac{\partial}{\partial x_i}\left(\frac{x_j}{|\boldsymbol{x}|}\right) \\ &= -\frac{\partial x_j}{\partial x_i}|\boldsymbol{x}|^{-3} - |\boldsymbol{x}|^{-1}\frac{x_j}{|\boldsymbol{x}|}\frac{\partial}{\partial|\boldsymbol{x}|}|\boldsymbol{x}|^{-1}\frac{\partial|\boldsymbol{x}|}{\partial x_i} \end{aligned} \tag{2.178}$$

that can be rewritten

$$\begin{aligned} -|\boldsymbol{x}|^{-2}\frac{\partial}{\partial x_i}\frac{\partial|\boldsymbol{x}|}{\partial x_j} &= -|\boldsymbol{x}|^{-3}\delta_{ij} + |\boldsymbol{x}|^{-3}\frac{\partial|\boldsymbol{x}|}{\partial x_i}\frac{\partial|\boldsymbol{x}|}{\partial x_j} \\ &= |\boldsymbol{x}|^{-3}\gamma_i\gamma_j - |\boldsymbol{x}|^{-3}\delta_{ij} \end{aligned} \tag{2.179}$$

which leads to

$$\frac{\partial^2}{\partial x_i \partial x_j}\frac{1}{|\boldsymbol{x}|} = \frac{1}{|\boldsymbol{x}|^3}(3\gamma_i\gamma_j - \delta_{ij}) \tag{2.180}$$

Inserting (2.167), (2.180) into dyadic Green's function expression given by (2.174) would then yield the following.

$$\mathfrak{G}_{ij}(\boldsymbol{x},t) = \frac{1}{4\pi\rho}(3\gamma_i\gamma_j - \delta_{ij})\frac{1}{|\boldsymbol{x}|^3}\int_{|\boldsymbol{x}|/\alpha}^{|\boldsymbol{x}|/\beta}\tau\delta(t-\tau)d\tau + \frac{1}{4\pi\rho\alpha^2|\boldsymbol{x}|}\gamma_i\gamma_j\delta\big(t-|\boldsymbol{x}|/\alpha\big) + \frac{1}{4\pi\rho\beta^2|\boldsymbol{x}|}(\delta_{ij}-\gamma_i\gamma_j)\delta\big(t-|\boldsymbol{x}|/\beta\big) \tag{2.181}$$

In tensorial form, introducing tensor product operator $(\bullet) \otimes (\bullet)$ and denoting $\boldsymbol{\Gamma}$ as direction vector of $|\boldsymbol{x}|$, we would get

$$\begin{aligned}\boldsymbol{\mathfrak{G}}(\boldsymbol{x},t) = \frac{1}{4\pi\rho}(3\boldsymbol{\Gamma}\otimes\boldsymbol{\Gamma}-\mathbf{1})\frac{1}{|\boldsymbol{x}|^3}\int_{|\boldsymbol{x}|/\alpha}^{|\boldsymbol{x}|/\beta}\tau\delta(t-\tau)d\tau + \frac{1}{4\pi\rho\alpha^2|\boldsymbol{x}|}\boldsymbol{\Gamma}\otimes\boldsymbol{\Gamma}\delta\big(t-|\boldsymbol{x}|/\alpha\big)\\ + \frac{1}{4\pi\rho\beta^2|\boldsymbol{x}|}(\mathbf{1}-\boldsymbol{\Gamma}\otimes\boldsymbol{\Gamma})\delta\big(t-|\boldsymbol{x}|/\beta\big)\end{aligned} \tag{2.182}$$

The dyadic Green's function carries the complete information of the displacement field resulting from unit impulses applied in each direction. Hence, using linearity, a point force can be additively decomposed into its components each of which is oriented along the principle cartesian coordinate axis. Therefore, the total displacement field $\boldsymbol{u}(\boldsymbol{x},t)$ can be found by superposing contributions from each component, each of which is given by convolution in time with the Dirac distribution. Let $\boldsymbol{F}(\boldsymbol{x},t) = \boldsymbol{F}(t)\delta(\boldsymbol{x})$ be the point source varying with time located at $\boldsymbol{\xi} = \mathbf{0}$. Then,

$$\begin{aligned}u_i(\boldsymbol{x},t) &= \mathfrak{G}_{ij} * F_j\\ &= \frac{1}{4\pi\rho}(3\gamma_i\gamma_j-\delta_{ij})\frac{1}{|\boldsymbol{x}|^3}\int_{|\boldsymbol{x}|/\alpha}^{|\boldsymbol{x}|/\beta}\tau F_j(t-\tau)d\tau + \frac{1}{4\pi\rho\alpha^2|\boldsymbol{x}|}\gamma_i\gamma_j F_j\big(t-|\boldsymbol{x}|/\alpha\big)\\ &\quad + \frac{1}{4\pi\rho\beta^2|\boldsymbol{x}|}(\delta_{ij}-\gamma_i\gamma_j)F_j\big(t-|\boldsymbol{x}|/\beta\big)\end{aligned} \tag{2.183}$$

Recognizing that the integral in the dyadic Green's function in (2.182) yields a ramp function represented by Heaviside function $H\big(t-|\boldsymbol{x}|/\alpha\big) - H\big(t-|\boldsymbol{x}|/\beta\big)$ multiplied with time $t \in \big(|\boldsymbol{x}|/\alpha, |\boldsymbol{x}|/\beta\big)$, the displacement field can be written as a convolution in time.

$$\begin{aligned}\boldsymbol{u}(\boldsymbol{x},t) &= \boldsymbol{\mathfrak{G}} * \boldsymbol{F}\\ &= \frac{1}{4\pi\rho|\boldsymbol{x}|^3}(3\boldsymbol{\Gamma}\otimes\boldsymbol{\Gamma}-\mathbf{1})\boldsymbol{F}(t) * t\big[H\big(t-|\boldsymbol{x}|/\alpha\big) - H\big(t-|\boldsymbol{x}|/\beta\big)\big]\\ &\quad + \frac{1}{4\pi\rho\alpha^2|\boldsymbol{x}|}(\boldsymbol{\Gamma}\otimes\boldsymbol{\Gamma})\boldsymbol{F}(t) * \delta\big(t-|\boldsymbol{x}|/\alpha\big)\\ &\quad + \frac{1}{4\pi\rho\beta^2|\boldsymbol{x}|}(\mathbf{1}-\boldsymbol{\Gamma}\otimes\boldsymbol{\Gamma})\boldsymbol{F}(t) * \delta\big(t-|\boldsymbol{x}|/\beta\big)\end{aligned} \tag{2.184}$$

It is remarkable that (2.183) is identical to the solution given by Stokes [93] in which, however, the propagation of light through an elastic medium, called the luminiferous aether, is sought. (2.183), (2.184) can be modified to represent an earthquake source

$$\boldsymbol{f} = -\mathbf{M}\cdot\boldsymbol{\nabla}(\boldsymbol{x}-\boldsymbol{\xi})S(t) \tag{2.185}$$

which can be used to represent various seismic sources acting at a point [44]. In (2.185), **M** denotes the seismic moment tensor magnitude of which yields the seismic moment $\mathbf{M} : \mathbf{M} = M_0$. The seismic moment tensor **M** can be constructed via taking the Gatéaux derivative of (2.183) [12], [13]. Furthermore, $S(t)$ in (2.185) represents the source-time function of the seismic event.

CHAPTER 3

NUMERICAL DISCRETIZATION: FINITE AND SPECTRAL ELEMENT IMPLEMENTATION OF 3-D WAVE EQUATION

Analytical solution to classical wave equation requires tremendous and rigorous mathematical analysis and depends upon assumptions set forth in the preceding chapter. Therefore, obtaining a closed-form solution would not often be possible unless a substantial amount of idealizations are incorporated into the solution process. These made the utilization of numerical solution methods inevitable. Fortunately, with the advent of computer technology and remarkable developments in computer science, enabling us to perform large-scale computations in solving complex problems with great accuracy in a decent amount of time, there are now a vast variety of numerical schemes, e.g., FDM, FEM, BEM, DWNM, SEM to name a few, available in the literature to solve complex partial differential equations, among which FEM will be explained in what follows.

The formulation of the classical wave equation in $\mathbb{R}^3$ yields an initial-boundary value problem (IBVP) that depends both on the spatial variables $\boldsymbol{x}(x, y, z) \in \boldsymbol{\Omega}$ and the time variable $t \in \mathbb{R}_t$. If the problem is well-posed, i.e. satisfies the following properties,

i. a solution exists,

ii. that solution is unique,

iii. the solution changes continuously with changes in the initial conditions,

then it might be implemented by a stable numerical algorithm without a need for reformulation in order to be able to perform numerical solutions. The latter condition might be difficult to show for the wave propagation problem in an inelastic anisotropic

nonhomogeneous medium which requires rigorous mathematical treatment. However, proofs of the first and the second conditions can be found in Aki. Hence, at least, given the initial and boundary conditions the displacement field $\boldsymbol{u}(\boldsymbol{x}, t)$ can be determined uniquely permitting the implementation of FEM or other numerical schemes discussed.

In FEM, the spatial domain $\boldsymbol{\Omega}$ is discretized into finite subdomains $\boldsymbol{\Omega}^e \subset \boldsymbol{\Omega}$ such that $\boldsymbol{\Omega} = \bigcup_{e=1}^{n_{el}} \boldsymbol{\Omega}^e$ where n_{el} denotes the number of subdomains, the so-called finite elements, the spatial domain $\boldsymbol{\Omega}$ is to be partitioned. Then, the functional form of state variables describing the system is presumed within each subdomain. In this way, rather than solving the governing differential equation for an infinitesimal material volume to obtain continuous solution throughout the domain, solution that is of class C^k, that is, $k-$ times continuously differentiable where $k = 0$ in general, implying piecewise continuity on $\boldsymbol{\Omega}$, is obtained within each element $\boldsymbol{\Omega}^e$. Then, the overall solution is easily constructed by distributing the solutions found at sampling points via interpolation functions, or so-called shape functions, inside each subdomain. Having roughly described the conceptual framework of FEM, generic discretization steps of IBVP governing the wave equation might be given as follows:

i. Accurate description of the IBVP in its strong form;

ii. Construction of weak from via principle of stationary action or multiplication the strong form with test function;

iii. Spatial discretization of the weak form;

iv. Temporal discretization of the spatially discretized weak form;

v. Solving the system of algebraic equations.

Let us first describe the strong form of the wave equation. In what follows, the domain will be represented by the union of the internal domain with its boundary, i.e. $\bar{\boldsymbol{\Omega}} = \boldsymbol{\Omega} \cup \boldsymbol{\Gamma}$. Furthermore, the boundary $\boldsymbol{\Gamma}$ is allowed to have a decomposition such that $\boldsymbol{\Gamma} = \overline{\boldsymbol{\Gamma}_u \cup \boldsymbol{\Gamma}_t}$ and $\boldsymbol{\Gamma}_u \cap \boldsymbol{\Gamma}_t = \varnothing$. Finally, the time interval over which the solution is sought is denoted as open interval $]t_0, T[$ to differentiate the initial conditions at time $t_0 \in \mathbb{R}_t$. Having posed the strong form of the wave equation, the corresponding

Table 3.1: Strong formulation of the classical wave equation.

(S) *Strong form of the wave equation*

Given $\boldsymbol{f} : \boldsymbol{\Omega}\times]t_0,T[\mapsto \mathbb{R}^3$, $\bar{\boldsymbol{u}} : \boldsymbol{\Gamma_u}\times]t_0,T[\mapsto \mathbb{R}^3$, $\bar{\boldsymbol{t}} : \boldsymbol{\Gamma_t}\times]t_0,T[\mapsto \mathbb{R}^3$, $\boldsymbol{u}_0 : \boldsymbol{\Omega} \mapsto \mathbb{R}^3$ and $\boldsymbol{v}_0 : \boldsymbol{\Omega} \mapsto \mathbb{R}^3$, find $\boldsymbol{u}(\boldsymbol{x},t) : \bar{\boldsymbol{\Omega}} \times [t_0,T] \mapsto \mathbb{R}^3$ such that followings are satisfied.

1. Balance Equation

   Linear Momentum $\quad \boldsymbol{\nabla}\cdot\boldsymbol{\sigma} + \boldsymbol{f} = \rho\ddot{\boldsymbol{u}} \quad$ in $\quad \boldsymbol{\Omega}\times]t_0,T[$

2. Constitutive Equations

   Stress Field $\quad \boldsymbol{\sigma} = \partial_{\boldsymbol{\varepsilon}}\hat{\Psi}(\boldsymbol{\varepsilon})$

3. Boundary Conditions

   Displacement $\quad \boldsymbol{u} = \bar{\boldsymbol{u}} \quad$ on $\quad \boldsymbol{\Gamma_u}\times]t_0,T[$

   Traction $\quad \boldsymbol{t} = \bar{\boldsymbol{t}} = \boldsymbol{\sigma}\cdot\boldsymbol{n} \quad$ on $\quad \boldsymbol{\Gamma_t}\times]t_0,T[$

4. Initial Conditions

   Displacement $\quad \boldsymbol{u}(\boldsymbol{x},t_0) = \boldsymbol{u}_0(\boldsymbol{x}) \quad$ in $\quad \boldsymbol{\Omega}$

   Velocity $\quad \boldsymbol{v}(\boldsymbol{x},t_0) = \boldsymbol{v}_0(\boldsymbol{x}) \quad$ in $\quad \boldsymbol{\Omega}$

weak form (W) needs to be constructed as a second step. Let us consider (3.1), denoting the first variation of the action function.

$$\delta S = \int_{t_1}^{t_2} \left(\frac{\partial \mathcal{L}}{\partial \boldsymbol{u}} \cdot \delta \boldsymbol{u} + \frac{\partial \mathcal{L}}{\partial \dot{\boldsymbol{u}}} \cdot \delta \dot{\boldsymbol{u}} + \frac{\partial \mathcal{L}}{\partial \boldsymbol{\varepsilon}} : \boldsymbol{\nabla} \delta \boldsymbol{u} \right) dt \tag{3.1}$$

Applying integration by parts on the second term would yield,

$$\delta S = \left[\frac{\partial \mathcal{L}}{\partial \dot{\boldsymbol{u}}} \cdot \delta \boldsymbol{u} \right] \Bigg|_{t=t_1}^{t=t_2} + \int_{t_1}^{t_2} \left(\frac{\partial \mathcal{L}}{\partial \boldsymbol{u}} \cdot \delta \boldsymbol{u} - \frac{\partial}{\partial t} \frac{\partial \mathcal{L}}{\partial \dot{\boldsymbol{u}}} \cdot \delta \boldsymbol{u} + \frac{\partial \mathcal{L}}{\partial \boldsymbol{\varepsilon}} : \boldsymbol{\nabla} \delta \boldsymbol{\varepsilon} \right) dt \tag{3.2}$$

Since the displacement fields $\boldsymbol{u}(\boldsymbol{x}, t_1)$ and $\boldsymbol{u}(\boldsymbol{x}, t_2)$ are assumed to be prescribed at times t_1 and t_2, the variation $\delta \boldsymbol{u}$ vanishes and hence the first term at the right hand side. It should be noted that, even if the displacement field at times t_1 and t_2 are not known, the virtual displacement field $\delta \boldsymbol{u}$ can be selected as zero at t_1 and t_2. Then, incorporating the definition of Lagrangian given in (2.99), (2.100), and invoking the principle of stationary action given by (2.101), the virtual work formulation is obtained.

$$\delta S = \int_{t_1}^{t_2} dt \left[\iiint_{\Omega} \boldsymbol{f} \cdot \delta \boldsymbol{u} d\Omega + \oiint_{\partial \Omega} \bar{\boldsymbol{t}} \cdot \delta \boldsymbol{u} d\Gamma - \iiint_{\Omega} \boldsymbol{\sigma} : \delta \boldsymbol{\varepsilon} d\Omega - \iiint_{\Omega} \rho \ddot{\boldsymbol{u}} \cdot \delta \boldsymbol{u} \right] = 0 \tag{3.3}$$

Unless $t_1 = t_2$, the only possible way to satisfy the latter equality is that terms in brackets should vanish, yielding the weak form (W).

$$\boxed{\iiint_{\Omega} \delta \boldsymbol{\varepsilon} : \boldsymbol{\sigma} d\Omega + \iiint_{\Omega} \delta \boldsymbol{u} \cdot \rho \ddot{\boldsymbol{u}} d\Omega = \iiint_{\Omega} \delta \boldsymbol{u} \cdot \boldsymbol{f} d\Omega + \oiint_{\partial \Omega} \delta \boldsymbol{u} \cdot \bar{\boldsymbol{t}} d\Gamma} \tag{3.4}$$

The virtual displacement field $\delta \boldsymbol{u}$ does not even need to depend on time, though it is ambiguous from the Hamiltonian's formulation due to the second term involving the time derivative of the virtual displacement field. To clarify this, an alternative formulation might be implemented. Let us multiply the strong form (S) with the virtual displacement field $\delta \boldsymbol{u}$ and integrate it over the domain.

$$\iiint_{\boldsymbol{\Omega}} \delta \boldsymbol{u} \cdot \rho \ddot{\boldsymbol{u}} d\Omega = \iiint_{\boldsymbol{\Omega}} \delta \boldsymbol{u} \cdot \boldsymbol{\nabla} \cdot \boldsymbol{\sigma} d\Omega + \iiint_{\boldsymbol{\Omega}} \delta \boldsymbol{u} \cdot \boldsymbol{f} d\Omega \tag{3.5}$$

Applying integration by parts on the second term would then yield,

$$\iiint_{\boldsymbol{\Omega}} \delta \boldsymbol{u} \cdot \rho \ddot{\boldsymbol{u}} d\Omega = \iiint_{\boldsymbol{\Omega}} \boldsymbol{\nabla} \cdot [\delta \boldsymbol{u} \cdot \boldsymbol{\sigma}] d\Omega - \iiint_{\boldsymbol{\Omega}} \boldsymbol{\nabla} \delta \boldsymbol{u} : \boldsymbol{\sigma} d\Omega + \iiint_{\boldsymbol{\Omega}} \delta \boldsymbol{u} \cdot \boldsymbol{f} d\Omega \tag{3.6}$$

Introducing the Gauss Theorem on the first term at the right hand side

$$\iiint_{\boldsymbol{\Omega}} \delta \boldsymbol{u} \cdot \rho \ddot{\boldsymbol{u}} d\Omega = \oiint_{\boldsymbol{\partial \Omega}} \delta \boldsymbol{u} \cdot \boldsymbol{\sigma} \cdot \boldsymbol{n} d\Gamma - \iiint_{\boldsymbol{\Omega}} \boldsymbol{\nabla} \delta \boldsymbol{u} : \boldsymbol{\sigma} d\Omega + \iiint_{\boldsymbol{\Omega}} \delta \boldsymbol{u} \cdot \boldsymbol{f} d\Omega \tag{3.7}$$

Finally, recognizing $\boldsymbol{\sigma} \cdot \boldsymbol{n} = \bar{\boldsymbol{t}}$ and $\boldsymbol{\nabla}\delta\boldsymbol{u} = \delta\boldsymbol{\varepsilon}$, we obtain the weak formulation (W) identically.

$$\boxed{\iiint_{\boldsymbol{\Omega}} \delta\boldsymbol{\varepsilon} : \boldsymbol{\sigma} d\Omega + \iiint_{\boldsymbol{\Omega}} \delta\boldsymbol{u} \cdot \rho\ddot{\boldsymbol{u}} d\Omega = \iiint_{\boldsymbol{\Omega}} \delta\boldsymbol{u} \cdot \boldsymbol{f} d\Omega + \oiint_{\boldsymbol{\partial\Omega}} \delta\boldsymbol{u} \cdot \bar{\boldsymbol{t}} d\Gamma} \tag{3.8}$$

The immediate advantage of weak formulation (W) over strong formulation (S) is that the Natural (i.e. Neumann) boundary conditions are automatically satisfied explicitly. This property is especially pronounced in the modeling of seismic wave propagation as Earth's free surface boundary discards the boundary term out reducing the complexity of the problem considerably concerning complicated topographies that would be formidable to involve in the solution. In addition, it should be noticed that no assumption is made on the time dependency of the virtual displacement field. However, although there is a large family of functions that can be used as virtual or so-called weight functions, they must still satisfy certain properties that will be given in the discretization part. Let us describe the weak form of the wave equation in a form that is similar to the representation of the strong from (S). In what follows, $\mathscr{U}$ denotes the collection of kinematically admissible test function space, i.e. collection of test functions satisfying homogeneous essential boundary condition on $\boldsymbol{\Gamma}_{\boldsymbol{u}}$, that can be mathematically stated along with the square-integrability condition as

$$\mathscr{U} = \{\delta\boldsymbol{u}(\boldsymbol{x}) \in H^1(\boldsymbol{\Omega}) | \boldsymbol{\Omega} \mapsto \mathbb{R}^3;\ \delta\boldsymbol{u}(\boldsymbol{x}) = \boldsymbol{0} \text{ on } \boldsymbol{\Gamma}_{\boldsymbol{u}}\} \tag{3.9}$$

where $H^1(\boldsymbol{\Omega})$ denotes the Sobolev space of order one including all functions satisfying the square-integrability condition.

It is crucial to observe the equivalence between the strong form (S) given in Table 3.1 and the weak form (W) given in Table 3.2. They are different manifestations of a given problem where in the latter the problem is weakened by explicitly incorporating Natural boundary conditions, which are automatically satisfied under certain conditions on the selection of trial functions (convergence requirements). Moreover, the essential boundary conditions along with the initial conditions are also multiplied with the test function to fulfill the virtual work principle. However, for the sake of clarity, they are given explicitly in the statement of (W). In the following section, they will also be given in the bilinear form. In this part, Galerkin discretization on the weak form (W) will be described, which is known as Galerkin FEM in literature. In order to be able to have a clear treatment of the subject, let us first define function

Table 3.2: The weak formulation of the classical wave equation.

(W) *Weak form of the wave equation*

Given $\boldsymbol{f} : \boldsymbol{\Omega}\times]t_0,T[\mapsto \mathbb{R}^3$, $\bar{\boldsymbol{u}} : \boldsymbol{\Gamma_u}\times]t_0,T[\mapsto \mathbb{R}^3$, $\bar{\boldsymbol{t}} : \boldsymbol{\Gamma_t}\times]t_0,T[\mapsto \mathbb{R}^3$, $\boldsymbol{u}_0 : \boldsymbol{\Omega} \mapsto \mathbb{R}^3$ and $\boldsymbol{v}_0 : \boldsymbol{\Omega} \mapsto \mathbb{R}^3$, find $\boldsymbol{u}(\boldsymbol{x},t) : \bar{\boldsymbol{\Omega}} \times [t_0,T] \mapsto \mathbb{R}^3$ such that for all $\delta\boldsymbol{u} \in \mathscr{U}$ followings are satisfied.

1. Bilinear Form of Balance Equation

$$\iiint_{\boldsymbol{\Omega}} \delta\boldsymbol{\varepsilon} : \boldsymbol{\sigma} d\Omega + \iiint_{\boldsymbol{\Omega}} \delta\boldsymbol{u} \cdot \rho\ddot{\boldsymbol{u}} d\Omega = \iiint_{\boldsymbol{\Omega}} \delta\boldsymbol{u} \cdot \boldsymbol{f} d\Omega + \oiint_{\boldsymbol{\partial\Omega}} \delta\boldsymbol{u} \cdot \bar{\boldsymbol{t}} d\Gamma$$

2. Constitutive Equations

   Stress Field $\quad \boldsymbol{\sigma} = \partial_{\boldsymbol{\varepsilon}} \hat{\Psi}(\boldsymbol{\varepsilon})$

3. Boundary Conditions

   Displacement $\quad \boldsymbol{u} = \bar{\boldsymbol{u}} \quad$ on $\quad \boldsymbol{\Gamma_u}\times]t_0,T[$

4. Initial Conditions

   Displacement $\quad \boldsymbol{u}(\boldsymbol{x},t_0) = \boldsymbol{u}_0(\boldsymbol{x}) \quad$ in $\boldsymbol{\Omega}$

   Velocity $\quad \boldsymbol{v}(\boldsymbol{x},t_0) = \boldsymbol{v}_0(\boldsymbol{x}) \quad$ in $\boldsymbol{\Omega}$

spaces from which trial and weight functions are to be selected. Let $\mathscr{U}_t$ denote a set of trial functions and $\mathscr{W}$ denote a set of weight functions respectively. That is,

$$\mathscr{U}_t = \{\boldsymbol{u}(\boldsymbol{x},t) \in H^1\big(\overline{\boldsymbol{\Omega}}\big)\big|\ \overline{\boldsymbol{\Omega}} \times \mathcal{T} \mapsto \mathbb{R}^3;\ \boldsymbol{u}(\boldsymbol{x},t) = \bar{\boldsymbol{u}} \text{ on } \boldsymbol{\Gamma}_{\boldsymbol{u}} \times \mathcal{T}\} \tag{3.10}$$

$$\mathscr{W} = \{\boldsymbol{w}(\boldsymbol{x}) \in H^1\big(\overline{\boldsymbol{\Omega}}\big)\big|\ \overline{\boldsymbol{\Omega}} \mapsto \mathbb{R}^3;\ \boldsymbol{w}(\boldsymbol{x}) = \boldsymbol{0} \text{ on } \boldsymbol{\Gamma}_{\boldsymbol{u}}\} \tag{3.11}$$

where $\mathcal{T}$ denotes time interval $t \in [t_0, T]$. This definition of $\mathscr{W}$ guarantees that all weight functions in $\mathscr{W}$ are kinematically admissible, that is, satisfy homogeneous essential boundary conditions on $\boldsymbol{\Gamma}_{\boldsymbol{u}}$. Secondly, let us construct subspaces of these function spaces consisting of $\mathscr{U}_t^{\mathfrak{h}}$ and $\mathscr{W}^{\mathfrak{h}}$ that are finite approximations to functions in $\mathscr{U}_t$ and $\mathscr{W}$, representing the collection of trial and weight functions accompanying to each subdomain $\boldsymbol{\Omega}^e$ having boundaries $\boldsymbol{\Gamma}_{\boldsymbol{u}}^e$ and $\boldsymbol{\Gamma}_{\boldsymbol{t}}^e$ such that $\boldsymbol{\Omega} = \bigcup_{e=1}^{n_{el}} \boldsymbol{\Omega}^e$, $\boldsymbol{\Gamma}_{\boldsymbol{u}} = \bigcup_{e=1}^{n_{el}} \boldsymbol{\Gamma}_{\boldsymbol{u}}^e$, $\boldsymbol{\Gamma}_{\boldsymbol{t}} = \bigcup_{e=1}^{n_{el}} \boldsymbol{\Gamma}_{\boldsymbol{t}}^e$. $\mathfrak{h}$ in $\mathscr{U}_t^{\mathfrak{h}}$ and $\mathscr{W}^{\mathfrak{h}}$ denotes the characteristic length scale of mesh discretization of $\boldsymbol{\Omega}$. This construction of function spaces assures that all properties that $\mathscr{U}_t$, $\mathscr{W}$ have identically applies to $\mathscr{U}_t^{\mathfrak{h}}$, $\mathscr{W}^{\mathfrak{h}}$, respectively. That is, if an ansatz $\boldsymbol{u}^{\mathfrak{h}} = \boldsymbol{u}^e(\boldsymbol{x},t) \in \mathscr{U}_t$, then it is also contained in $\mathscr{U}_t^{\mathfrak{h}}$, i.e. $\boldsymbol{u}^e(\boldsymbol{x},t) \in \mathscr{U}_t^{\mathfrak{h}}$ implying that $\mathscr{U}_t^{\mathfrak{h}} \subset \mathscr{U}_t$. The argument also applies to weight functions $\boldsymbol{w}^{\mathfrak{h}} \in \mathscr{W}^{\mathfrak{h}}$. Having constructed all the necessary function spaces, we are now in a good position to establish the Galerkin FEM discretization scheme. The underlying principle of Galerkin FEM discretization is that identical basis functions are used to construct weight and trial functions by taking the advantage of the fact that the space $\mathscr{W}^{\mathfrak{h}} \subset \mathscr{W}$ consists of only the kinematically admissible functions. To illustrate this, let us assume that the approximate solution $\boldsymbol{u}^{\mathfrak{h}} = \boldsymbol{u}^e(\boldsymbol{x},t)$ for a given subdomain $\boldsymbol{\Omega}^e$ is additively decomposable into the following form.

$$\boldsymbol{u}^{\mathfrak{h}} = \boldsymbol{v}^{\mathfrak{h}} + \bar{\boldsymbol{u}}^{\mathfrak{h}} \tag{3.12}$$

where, $\boldsymbol{v}^h = \boldsymbol{v}^e(\boldsymbol{x},t) \in \mathscr{W}^{\mathfrak{h}}$ is the trial solution at an elemental level and $\bar{\boldsymbol{u}}^{\mathfrak{h}} = \bar{\boldsymbol{u}}^e(\boldsymbol{x},t) \in \mathscr{U}_t^{\mathfrak{h}}$ is the prescribed essential boundary condition on an element boundary. Since $\boldsymbol{v}^{\mathfrak{h}}$ belongs to space of weight functions $\mathscr{W}^h$, it vanishes at boundaries. Another thing to notice is that, although the function space $\mathscr{W}^{\mathfrak{h}}$ does not include time dependent functions, $\boldsymbol{v}^{\mathfrak{h}}$ is shown to be contained in $\mathscr{W}^{\mathfrak{h}}$. The reason is that, for each fixed time, $\boldsymbol{v}^{\mathfrak{h}}$ has a spatial distribution specific to that instant which can be represented by functions belonging to $\mathscr{W}^{\mathfrak{h}}$. An immediate consequence of such decomposition is that $\boldsymbol{u}^{\mathfrak{h}}$ and $\boldsymbol{v}^{\mathfrak{h}}$ can be selected from the same collection of functions

belonging to $\mathscr{W}^{\mathfrak{h}} \in \mathscr{W}$ up to $\bar{\boldsymbol{u}}^h$. Hence, selecting $\boldsymbol{v}^h = \delta\boldsymbol{u}^h$, and defining Galerkin functional as

$$\mathscr{G}_{int}(\delta\boldsymbol{u}, \boldsymbol{u}) = \mathscr{G}_{ext}(\delta\boldsymbol{u}) \tag{3.13}$$

where

$$\mathscr{G}_{int}(\delta\boldsymbol{u}, \boldsymbol{u}) \coloneqq \iiint_{\boldsymbol{\Omega}} \delta\boldsymbol{\varepsilon} : \boldsymbol{\sigma} d\Omega + \iiint_{\boldsymbol{\Omega}} \delta\boldsymbol{u} \cdot \rho\ddot{\boldsymbol{u}} d\Omega \tag{3.14}$$

$$\mathscr{G}_{ext}(\delta\boldsymbol{u}) \coloneqq \iiint_{\boldsymbol{\Omega}} \delta\boldsymbol{u} \cdot \boldsymbol{f} d\Omega + \oiint_{\boldsymbol{\partial\Omega}} \delta\boldsymbol{u} \cdot \bar{\boldsymbol{t}} d\Gamma \tag{3.15}$$

and introducing bilinear symmetric forms $B(\cdot,\cdot)$, $(\cdot,\cdot)$, $(\cdot,\cdot)_{\boldsymbol{\partial\Omega}}$ Galerkin Weak Form (G) is obtained.

(G) in Table 3.3 represents the spatially discretized weak form of the wave equation. In each subdomain, then, an approximate solution is sought on nodes by introducing shape functions $\mathcal{N}_{\mathfrak{n}} \in \mathscr{W}^{\mathfrak{h}}$ where $\mathfrak{n}$ denotes node number up to which an element subdomain is to be discretized.

$$\boldsymbol{u}^{\mathfrak{h}}(\boldsymbol{x}, t) = \sum_A \mathcal{N}_A(\boldsymbol{x}) \boldsymbol{d}_A(t) \qquad \text{and} \qquad \delta\boldsymbol{u}^{\mathfrak{h}}(\boldsymbol{x}) = \sum_A \mathcal{N}_A(\boldsymbol{x}) \boldsymbol{w}_A \tag{3.16a}$$

$$\boldsymbol{\nabla}\boldsymbol{u}^{\mathfrak{h}}(\boldsymbol{x}, t) = \sum_A \boldsymbol{d}_A(t) \otimes \partial_{\boldsymbol{x}} \mathcal{N}_A(\boldsymbol{x}) \qquad \text{and} \qquad \boldsymbol{\nabla}\delta\boldsymbol{u}^{\mathfrak{h}}(\boldsymbol{x}) = \sum_A \boldsymbol{w}_A \otimes \partial_{\boldsymbol{x}} \mathcal{N}_A(\boldsymbol{x}) \tag{3.16b}$$

where $\boldsymbol{d}(t)$ represents nodal solutions over an element domain, $\boldsymbol{w}$ represents arbitrary weighting coefficient vector at each node. In most engineering applications, Lagrange interpolation functions with C_0 continuity are employed as shape functions due to their practicality and due to the ease of satisfying convergence requirements of smoothness, continuity across element boundaries, and completeness. Generic algorithms to construct arbitrary order Lagrange interpolation functions are presented in detail in Hughes [85].

3.1 Spatial Discretization

In most engineering problems, the geometry of a given domain under consideration is often irregular in shape necessitating the construction of shape functions for each particular problem, which is not feasible. However, to overcome this problem, the

Table 3.3: The Galerkin Weak formulation of the classical wave equation.

(G) *Galerkin Weak form of the wave equation*

Given $\boldsymbol{f} : \boldsymbol{\Omega}\times]t_0,T[\mapsto \mathbb{R}^3$, $\bar{\boldsymbol{u}} : \boldsymbol{\Gamma_u}\times]t_0,T[\mapsto \mathbb{R}^3$, $\bar{\boldsymbol{t}} : \boldsymbol{\Gamma_t}\times]t_0,T[\mapsto \mathbb{R}^3$, $\boldsymbol{u}_0 : \boldsymbol{\Omega} \mapsto \mathbb{R}^3$ and $\boldsymbol{v}_0 : \boldsymbol{\Omega} \mapsto \mathbb{R}^3$, find $\boldsymbol{u}^{\mathfrak{h}}(\boldsymbol{x},t) = \delta\boldsymbol{u}^{\mathfrak{h}} + \bar{\boldsymbol{u}}^{\mathfrak{h}} : \bar{\boldsymbol{\Omega}}^e \times [t_0,T] \mapsto \mathbb{R}^3$, $\boldsymbol{u}^{\mathfrak{h}} \in \mathscr{U}_t^{\mathfrak{h}}$ such that for all $\delta\boldsymbol{u}^{\mathfrak{h}} \in \mathscr{W}^{\mathfrak{h}}$ followings are satisfied.

1. Bilinear Form of Balance Equation

$$\begin{aligned} \mathscr{G}_{int}\big(\delta\boldsymbol{u}^{\mathfrak{h}},\boldsymbol{u}^{\mathfrak{h}}\big) &= \mathscr{G}_{ext}\big(\delta\boldsymbol{u}^{\mathfrak{h}}\big) \\ B\big(\delta\boldsymbol{u}^{\mathfrak{h}},\boldsymbol{u}^{\mathfrak{h}}\big) + \big(\delta\boldsymbol{u}^{\mathfrak{h}},\rho\ddot{\boldsymbol{u}}^{\mathfrak{h}}\big) &= \big(\delta\boldsymbol{u}^{\mathfrak{h}},\boldsymbol{f}\big) + \big(\delta\boldsymbol{u}^{\mathfrak{h}},\bar{\boldsymbol{t}}\big) - B\big(\delta\boldsymbol{u}^{\mathfrak{h}},\bar{\boldsymbol{u}}^{\mathfrak{h}}\big) \\ &\quad - \big(\delta\boldsymbol{u}^{\mathfrak{h}},\rho\ddot{\bar{\boldsymbol{u}}}^{\mathfrak{h}}\big) \end{aligned}$$

2. Constitutive Equations

   Stress Field $\quad \boldsymbol{\sigma} = \partial_{\boldsymbol{\varepsilon}}\hat{\Psi}(\boldsymbol{\varepsilon})$

3. Boundary Conditions

   Displacement $\quad \boldsymbol{u} = \bar{\boldsymbol{u}} \quad$ on $\quad \boldsymbol{\Gamma_u}\times]t_0,T[$

4. Initial Conditions

   Displacement $\quad \boldsymbol{u}(\boldsymbol{x},t_0) = \boldsymbol{u}_0(\boldsymbol{x}) \quad$ in $\boldsymbol{\Omega}$

   Velocity $\quad \boldsymbol{v}(\boldsymbol{x},t_0) = \boldsymbol{v}_0(\boldsymbol{x}) \quad$ in $\boldsymbol{\Omega}$

domain mapping technique is utilized. That is, each element $\bar{\Omega}^e$ domain is bijectively mapped on to a reference element or so-called parent domain often denoted by $\square$. In this way, any element located in a given physical element can be mapped on to the parent domain eliminating the construction of shape functions for each particular physical element domain, as long as bijectivity is preserved. It is important to notice that the domain mapping technique is mathematically identical to the geometric mapping concept given in Chapter 2. In other words, physical elements are constructed via the deformation of parent elements, or vice versa, that is $\boldsymbol{x} : \square \to \bar{\Omega}^e$. That is, every point $(\xi, \eta, \zeta) \in \square$ is mapped on to $(x, y, z) \in \bar{\Omega}^e$ via

$$\boldsymbol{x}(\xi, \eta, \zeta) = \sum_A \mathcal{N}_A(\xi, \eta, \zeta) \boldsymbol{x}_A^e \tag{3.17}$$

where $\boldsymbol{x}_A = (x_A, y_A, z_A)$ is the global nodal coordinates of the Ath node of physical element, $\mathcal{N}_A(\xi, \eta, \zeta)$ is the shape function used in discretization step where $(\xi, \eta, \zeta) \in [-1, 1] \times [-1, 1] \times [-1, 1]$. 3.17, along with (3.16a) and (3.16b) constitutes the isoparametric formulation often involved in FEM. That is, the same basis functions are used to discretize the geometry and the solution. However, in SEM higher order Lagrange polynomials are used for the representative solution over an element, whereas the geometry is discretized with first or second order Lagrange polynomials in practice [44].

To be able to incorporate isoparametric elements into semi-discretized Galerkin weak formulation (G), the Jacobian matrix of the transformation is needed for each element represented by (3.17). More explicitly,

$$\boldsymbol{J} = \partial_{\boldsymbol{\xi}} \boldsymbol{x} = \sum_A (\partial_{\boldsymbol{\xi}} \mathcal{N}_A) \boldsymbol{x}_A \tag{3.18}$$

where $\boldsymbol{\xi}$, and $\boldsymbol{x}$ are the parent domain coordinate vector, and the global element coordinate vector respectively. The determinant of $\boldsymbol{J}$ gives the Jacobian of the transformation, namely $\det(\boldsymbol{J}) = J(\xi, \eta, \zeta)$, which is identical to (2.6). Then, infinitesimal small volume elements in (G) is given by $dxdydz = Jd\xi d\eta d\zeta$. In addition, the spatial derivative term in the virtual strain energy integral can also be written in terms of parent coordinates employing (3.17). To complete the isoparametric formulation, let us select element shape functions $\mathcal{N}(\boldsymbol{x}(\xi, \eta, \zeta))$ as Lagrange polynomials. For $n + 1$ sampling points over one coordinate line, say $\xi \in [-1, 1]$ defined on parent domain

$\square$, the Lagrange polynomials of order n can be written as

$$\ell_a^n(\xi) = \prod_{k=0,k\neq a}^{n} \frac{\xi - \xi_k}{\xi_a - \xi_k} = \frac{(\xi-\xi_0)(\xi-\xi_1)\dots(\xi-\xi_{a-1})(\xi-\xi_{a+1})\dots(\xi-\xi_n)}{(\xi-\xi_0)(\xi-\xi_1)\dots(\xi-\xi_{a-1})(\xi-\xi_{a+1})\dots(\xi-\xi_n)} \tag{3.19}$$

which yields Kronecker's delta function

$$\ell_a^n(\xi_b) = \delta_{ab} \tag{3.20}$$

which significantly simplifies the numerical integration step in combination with the Gauss-Lobatto-Legendre integration method in SEM. It is straightforward to generalize (3.19) to three dimensions. That is, for a given node A, corresponding shape function $\mathcal{N}_A$ can be written as

$$\mathcal{N}_A(\xi,\eta,\zeta) = \ell_a^{n_a}(\xi)\ell_b^{n_b}(\eta)\ell_c^{n_c}(\zeta) \tag{3.21}$$

where n_a, n_b, n_c, denotes the order or each Lagrange polynomial in each standard coordinate directions ξ, η, ζ. Discretization steps involved in both FEM and SEM are identical up to the selection of representation functions on the elements. The main difference between FEM and SEM is that, in the former isoparametric formulation is often used in practice, whereas in the latter higher order polynomials are used to represent the solution although the geometric discretization is identical to FEM. Having defined the shape functions, numerical integration schemes might be introduced as a next step.

3.2 Numerical Integration

3.2.1 Gauss Quadrature

To evaluate integral terms in (G), a numerical quadrature scheme is needed to be employed for a computer algorithm. In FEM literature, the Gauss Quadrature is one of the most utilized quadrature schemes due to its remarkable accuracy, and efficiency as it requires n points to exactly integrate a $2n-1$th order polynomial. The fundamental principle behind the Gauss Quadrature is to utilize the orthogonality of Legendre polynomials, which can be obtained from the monomial basis $\{1, x, x^2 \dots x^n\}$ via

Gram-Schmidt orthogonalization process. That is, for the n^{th} order Legendre polynomial,

$$\mathcal{L}_n = x^n - \frac{\int_{-1}^{1} x^n \mathcal{L}_0 dx}{\int_{-1}^{1} \mathcal{L}_0 \mathcal{L}_0 dx}\mathcal{L}_0 - \ldots - \frac{\int_{-1}^{1} x^n \mathcal{L}_{n-1} dx}{\int_{-1}^{1} \mathcal{L}_{n-1} \mathcal{L}_{n-1} dx}\mathcal{L}_{n-1} \tag{3.22}$$

Then, a polynomial of degree $2n-1$ can be represented by

$$P_{2n-1} = \mathcal{L}_n Q_{n-1} + R_{n-1} \tag{3.23}$$

where subscripts denote the order of polynomials, R represents the residual term, Q represents the quotient. Since $\mathcal{L}_n$ is an orthogonal polynomial, weighted integral of (3.23) over the standard domain $[-1, 1]$ would yield

$$\int_{-1}^{1} w P_{2n-1} dx = \int_{-1}^{1} w \mathcal{L}_n Q_{n-1} dx + \int_{-1}^{1} w R_{n-1} dx = \int_{-1}^{1} w R_{n-1} dx \tag{3.24}$$

where w is an arbitrary weight function. Furthermore, since the remainder term R_{n-1} is degree of $n-1$, one can choose n sampling points to construct R_{n-1} exactly by interpolation,

$$R_{n-1} = \sum_{r=1}^{n} R(x_r) p_r(x) \tag{3.25}$$

If, sampling points are selected to be roots of Legendre Polynomial $\mathcal{L}_n$ as well, then (3.23) reduces to

$$P_{2n-1}(x_r) = \mathcal{L}_n(x_r) Q_{n-1}(x_r) + R_{n-1}(x_r) = R_{n-1}(x_r) \tag{3.26}$$

Incorporating (3.26), (3.25) into (3.24) would then finally yield,

$$\begin{aligned} \int_{-1}^{1} w P_{2n-1} dx = \int_{-1}^{1} w R_{n-1} dx &= \int_{-1}^{1} w(x) \sum_{r=1}^{n} R(x_r) p_r(x) \\ &= \sum_{r=1}^{n} R(x_r) \int_{-1}^{1} w(x) p_r(x) dx \\ &= \sum_{r=1}^{n} w_r R(x_r) \end{aligned} \tag{3.27}$$

the Gauss Quadrature scheme proving that any polynomial of degree $2n-1$ can be exactly integrated by Gauss Quadrature using only n sampling points. Since the approximation functions used in the numerical solution of the wave equation are all

polynomials, no further errors are introduced into the solution. Moreover, generalization to three dimensions can be shown as follows.

$$\int_{-1}^{1}\int_{-1}^{1}\int_{-1}^{1} f(x,y,z)dx\,dy\,dz \approx \sum_{i}\sum_{j}\sum_{k} w_i w_j w_k f(x_i,y_j,z_k) \tag{3.28}$$

Noticing that all the terms inside integrals given by (G) are scalars, it would be useful to implement the Gauss Quadrature scheme on a general scalar-valued function. Let $f(\boldsymbol{x}(\xi,\eta,\zeta))$ be a scalar-valued function of position $\boldsymbol{x}$ over the domain $\boldsymbol{\Omega}^e$. Then, the volumetric integral of f might be approximated numerically as

$$\begin{aligned}\iiint_{\boldsymbol{\Omega}^e} f(\boldsymbol{x})dxdydz &= \int_{-1}^{1}\int_{-1}^{1}\int_{-1}^{1} f(\boldsymbol{x}(\xi,\eta,\zeta))J(\xi,\eta,\zeta)d\xi d\eta d\zeta \\ &\approx \sum_{a}\sum_{b}\sum_{c} f(\xi_a,\eta_b,\zeta_c)J(\xi_a,\eta_b,\zeta_c)\end{aligned} \tag{3.29}$$

or in a compact form by denoting $f(\xi_a,\eta_b,\zeta_c) = f^{abc}$, $J(\xi_a,\eta_b,\zeta_c) = J^{abc}$,

$$\boxed{\iiint_{\boldsymbol{\Omega}^e} f(\boldsymbol{x})d\Omega \approx \sum_{a}\sum_{b}\sum_{c} w_a w_b w_c f^{abc} J^{abc}} \tag{3.30}$$

3.3 Gauss-Lobatto-Legendre Quadrature

In SEM, Gauss-Lobatto-Legendre Quadrature is used as it admits the construction of diagonal mass matrix, which is not the case in FEM without introducing mass lumping techniques. Therefore, SEM gains very desirable property over FEM through the Gauss-Lobatto-Legendre scheme due to a remarkable reduction in the time complexity of the algorithm by eliminating the inversion step of the mass matrix. To achieve this, instead of Gauss points, the method introduces Gauss-Lobatto-Legendre (GLL) points that are the roots of the first derivative of the Legendre polynomials. In this way, the element end points are always included in the numerical integration step yielding a mass lumping scheme with the utilization of (3.20). To illustrate this, let us consider the second term of (G) in (3.14). Inserting (3.16a), (3.20), (3.28) into the second term of (3.14) yields the following.

$$\boxed{\iiint_{\boldsymbol{\Omega}^e} \rho\ddot{\boldsymbol{u}}\cdot\delta\boldsymbol{u}d\Omega \approx \sum_{a,b,c} w_a w_b w_c \rho(\xi_a,\eta_b,\zeta_c)J(\xi_a,\eta_b,\zeta_c)\sum_{i} w_i^{abc}\ddot{u}_i^{abc}(t)} \tag{3.31}$$

(3.31) emphasizes that the elemental mass matrices and consequently the global mass matrix are diagonal since the weighting coefficients w_i are arbitrary.

Armed with (3.16a), (3.16b), (3.30), (3.31), the complete discretization of (G) would be performed with FEM and SEM respectively. Detailed construction of elemental and global matrices can be found in [42], [44], [94]. Next, the temporal discretization of semi-discrete Galerkin Weak Form (G) via Newmark-β scheme will be briefly presented.

3.4 Temporal Discretization

Temporal discretization of semi-discretized Galerkin Weak Form (G) is done by introducing Newmark's β Scheme [95]. There are numerous numerical algorithms available for the semi-discrete equation of motion given by (G). For a detailed discussion of a substantial amount of such numerical algorithms, [85], [86] are referred. Newmark's β method is based on the first order Taylor's expansion of acceleration with the weighted averaged time derivative term.

$$\boldsymbol{a}(t+\Delta t) = \boldsymbol{a}(t) + \dot{\boldsymbol{a}}\Delta t + \dots \tag{3.32a}$$

$$\boldsymbol{v}(t+\Delta t) = \boldsymbol{v}(t) + \boldsymbol{a}\Delta t + \dot{\boldsymbol{a}}\frac{\Delta t^2}{2!} + \dots \tag{3.32b}$$

$$\boldsymbol{u}(t+\Delta t) = \boldsymbol{u}(t) + \boldsymbol{v}\Delta t + \boldsymbol{a}\frac{\Delta t^2}{2!} + \dot{\boldsymbol{a}}\frac{\Delta t^3}{3!} + \dots \tag{3.32c}$$

Truncating the second order terms and expressing the time derivative of acceleration as

$$\boldsymbol{a} \approx [\boldsymbol{a}(t+\Delta t) - \boldsymbol{a}(t)]/\Delta t \tag{3.33}$$

(3.32a), (3.32b) can be rewritten as

$$\boldsymbol{v}(t+\Delta t) = \boldsymbol{v}(t) + \boldsymbol{a}\Delta t + \frac{\Delta t}{2!}[\boldsymbol{a}(t+\Delta t) - \boldsymbol{a}(t)] \tag{3.34a}$$

$$\boldsymbol{u}(t+\Delta t) = \boldsymbol{u}(t) + \boldsymbol{v}\Delta t + \boldsymbol{a}\frac{\Delta t^2}{2!} + \frac{\Delta t^2}{3!}[\boldsymbol{a}(t+\Delta t) - \boldsymbol{a}(t)] \tag{3.34b}$$

Introducing parameters $\gamma \in [0,1]$ and $\beta \in [0, 0.5]$ to represent the derivative of acceleration as a weighted average of its current and past values, (3.34a), (3.34b) can be put into final form.

$$\boldsymbol{v}(t+\Delta t) = \boldsymbol{v}(t) + \Delta t[\gamma\boldsymbol{a}(t+\Delta t) + (1-\gamma)\boldsymbol{a}(t)] \tag{3.35a}$$

$$\boldsymbol{u}(t+\Delta t) = \boldsymbol{u}(t) + \boldsymbol{v}\Delta t + \frac{\Delta t^2}{2}[2\beta\boldsymbol{a}(t+\Delta t) + (1-2\beta\ )\boldsymbol{a}(t)] \tag{3.35b}$$

(3.35a), (3.35b) give the general Newmark's β scheme. Depending on the parameters γ and β, the method coincides with the other well-known numerical schemes. For instance, when $\gamma = 0.5$ and $\beta = 0$, the explicit central difference scheme would be obtained. On the other hand, if $\beta = 0.5$ is selected while keeping γ the same, the average constant acceleration method would be obtained. In that case, the resultant scheme is unconditionally stable allowing one to select larger time steps. However, since the semi-discrete equation of motion involves inversion of mass matrix requiring considerable computational effort, explicit Newmark's scheme, i.e. explicit central difference scheme with $\gamma = 0.5$, $\beta = 0$, would be useful since it eliminates the mass matrix inversion step.

The semi-discrete equation of motion with initial conditions $\boldsymbol{u}(\boldsymbol{x}, t_0) = \boldsymbol{u}_0$ and $\boldsymbol{v}(\boldsymbol{x}, t_0) = \boldsymbol{v}_0$

$$\boldsymbol{M}\boldsymbol{a} + \boldsymbol{C}\boldsymbol{v} + \boldsymbol{K}\boldsymbol{u} = \boldsymbol{F} \tag{3.36}$$

can be updated at each time step Δt via Newmark's β method in the form of a predictor-corrector algorithm. In (3.36), $\boldsymbol{M}$ denotes the global mass matrix, $\boldsymbol{C}$ denotes the absorbing boundary matrix, $\boldsymbol{K}$ denotes the global stiffness matrix, and $\boldsymbol{F}$ denotes the global force vector.

Table 3.4: The temporal discretization of the semi-discrete wave equation via Newmark's β method in the form of a predictor-corrector algorithm.

Implementation of the Newmark-β Method

Given initial conditions $\boldsymbol{u}_0$, $\boldsymbol{v}_0$, the predictor-corrector algorithm for the semi-discrete equation of motion can be constructed as follows.

1. Initial Acceleration

   $$\boldsymbol{a}_n = \boldsymbol{M}^{-1}[\boldsymbol{F}_n - \boldsymbol{C}\boldsymbol{v}_n - \boldsymbol{K}\boldsymbol{u}_n]$$

2. Predictor

   $$\tilde{\boldsymbol{u}} = \boldsymbol{u}_n + \boldsymbol{v}_n + \frac{\Delta t^2}{2}(1-2\beta)\boldsymbol{a}_n$$
   $$\tilde{\boldsymbol{v}} = \boldsymbol{v}_n + (1-\gamma)\Delta t\boldsymbol{a}_n$$

3. Corrector

   $$\boldsymbol{a}_{n+1} = \bar{\boldsymbol{M}}^{-1}\bar{\boldsymbol{F}}$$
   $$\boldsymbol{v}_{n+1} = \tilde{\boldsymbol{v}} + \Delta t\gamma\boldsymbol{a}_n$$
   $$\boldsymbol{u}_{n+1} = \tilde{\boldsymbol{u}} + \Delta t^2\beta\boldsymbol{a}_n$$
   where $\bar{\boldsymbol{M}} = \boldsymbol{M} + \gamma\Delta t\boldsymbol{C} + \beta\Delta t^2\boldsymbol{K}$ and $\bar{\boldsymbol{F}} = \boldsymbol{F} - \boldsymbol{C}\tilde{\boldsymbol{v}} - \boldsymbol{K}\tilde{\boldsymbol{u}}$

CHAPTER 4

NUMERICAL SIMULATION OF THE 2020 SAMOS EARTHQUAKE: AN APPLICATION OF THE SPECTRAL ELEMENT METHOD

4.1 General

This chapter presents deterministic ground motion simulations of the M_W 7.0 Samos Island (Aegean Sea) Earthquake that occurred on October 30th, 2020. The event exhibits significant ground motion amplifications at low frequencies ($0.5 - 1.5$ Hz) particularly in the Karşıyaka and Bayraklı districts due to the existence of soft soil deposits[96] and hence selected as the case study for the deterministic ground motion simulation with the spectral element method. Section 4.2 provides background information on the study area. Section 4.3 introduces the SPECFEM3D Cartesian Package used in numerical simulations. Earthquake source and path parameters are, then, given in Section 4.4, while shear wave velocity, β and compressional wave velocity α models incorporated in the model are described in Section 4.5, followed by the numerical details highlighted in Section 4.6. Finally, in Section 4.7, a comparison of synthetic acceleration records with the observed data is illustrated.

4.2 Background Information on the Samos 2020 Earthquake and the Study Area

On October 30th, 2020, an earthquake of M_W 7.0 with an east-west striking, north dipping normal fault mechanism [97] occurred on the northern coast of Samos Island in the Aegean Sea that severely affected both Greece and Turkey, causing various impacts on both countries. The earthquake led to a tsunami wave that had a fierce effect

on coastal areas near the epicenter, particularly on the northern coast of Samos Island in Greece and on the Sığacık Bay in Turkey [98]. Furthermore, ground shaking localization, and a variety of geotechnical phenomena, all of which led to the collapse of structures and consequently to 119 fatalities, were observed. On the Turkey side, the impacts of the earthquake were intensified in İzmir city due to basin and site effects, especially in Bayraklı District because of soft soil conditions leading to amplifying ground motions in the low-frequency range.

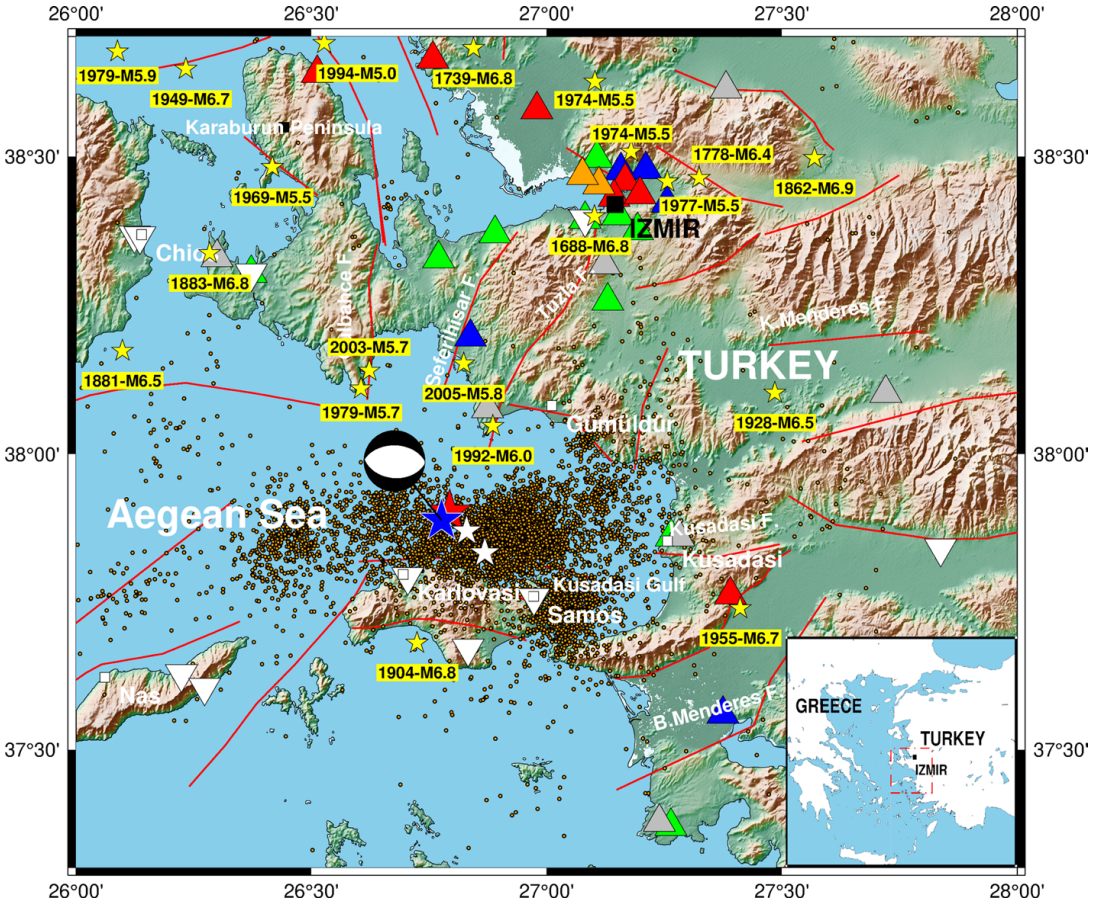

Figure 4.1: Seismicity of the region. The yellow stars represent the epicenter of historical major earthquakes, whereas the blue and red stars point to the location of the mainshock according to AFAD and KOERI, with white stars depicting the major sequential events. Seismic stations are represented as colored triangles with colors indicating the site class. The inverted triangles shown in white, on the other hand, indicate the geodetic stations. The figure is adapted from [96].

Samos Island and the west coast of Turkey have been repeatedly struck by destructive

earthquakes in both ancient and modern times. Early in the 20th century, on August 11, 1904, a M_W 6.8 earthquake hit the south coast of Samos, intensely damaging the Greek islands and annihilating a large number of settlements in western Anatolia [99]. Furthermore, between 1700 and 1799, around twelve major earthquakes occurred in and near Samos between the years 201–197 BC, 46–47 AD, and 1700–1799 [100]. Large earthquakes, in particular, struck the area on July 10, 1688, in 1739, and in 1788, all of which had disastrous effects on the city of Izmir [101]. More recently, buildings in the region suffered severe damage by sequential seismic events of moderate magnitude. Figure 4.1 illustrates the seismicity of the region highlighting the historical events.

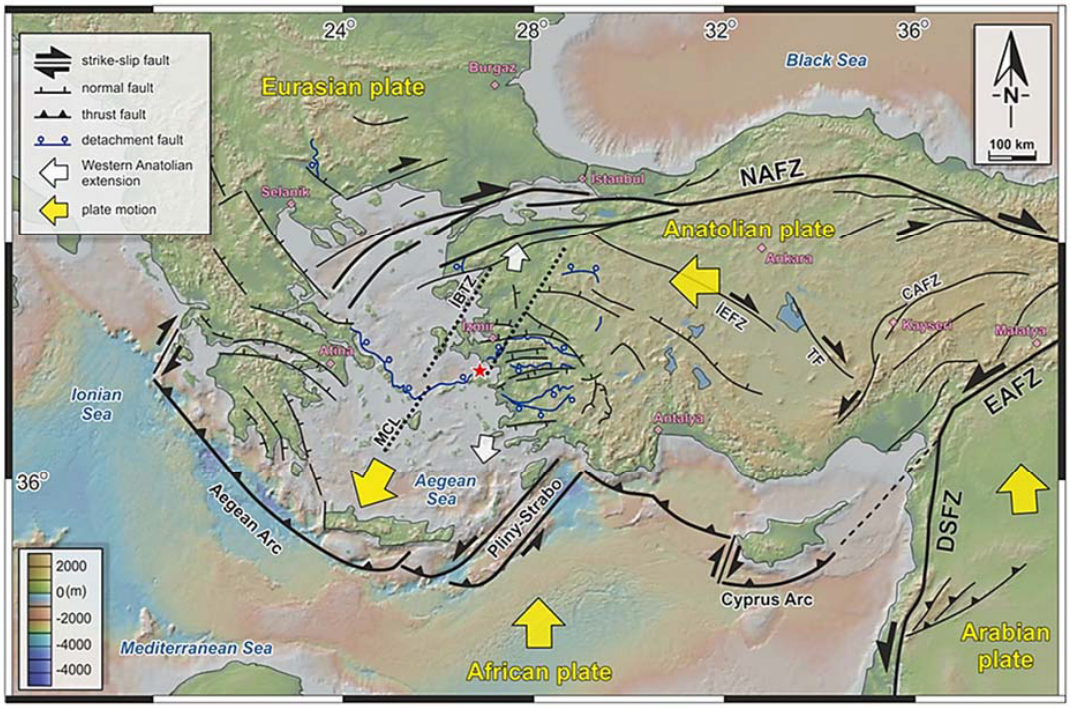

Figure 4.2: Regional tectonic setting. The escape of the Anatolian plate towards the Aegean due to squeezing action by the Arabian plate through the East Anatolian Fault Zone (EAFZ) and Dead Sea Fault Zone (DSFZ) and by the Eurasian plate through the North Anatolian Fault Zone (NAFZ), stretching of the Aegean and Western Anatolian crust triggered by the subducting eastern Mediterranean plate under the Aegean are the driving mechanisms of the seismicity that affects the region. Figure is adapted from [102].

The study area is located in the Aegean region exhibiting significant seismic activity

due to the tectonic setting of the region. The African, Arabian, and Eurasian plates squeeze the Anatolian plate through the Dead Sea Fault Zone (DSFZ), East Anatolian Fault Zone (EAFZ), and North Anatolian Fault Zone (NAFZ), respectively. This continuous motion between the plates leads to the escape of the Anatolian plate towards the Aegean. On the other hand, the subducting Mediterranean plate under the Aegean triggers the stretching of the Aegean and Western Anatolian crust. Figure 4.2 depicts the regional tectonic setting of the study area and illustrates the driving mechanisms of the seismicity that affects the region.

4.3 Introduction to SEM Software: The SPECFEM3D Cartesian Package

The SPECFEM3D Cartesian package [103] is a deterministic seismic wave propagation simulation software package (the main historical authors are Dimitri Komatitsch and Jeroen Tromp) well suited to perform local or regional ground motion simulations utilizing the spectral element method (SEM) fundamentals of which have already been given in the preceding chapter. It is capable of proper treatment of highly distorted mesh elements without sacrificing the accuracy of the model ([41], [104], [105], [106]) and has remarkable convergence properties as it exploits hp-convergence schemes. In addition to remarkable accuracy and convergence characteristics, its applicability to parallel computation on clusters of high-performance computers and GPU-accelerating graphics cards ([49], [107]) makes the package very efficient and considerably fast.

The geometry of the region under consideration, including topography, bathymetry, and 3D crustal model, can be handled as well by the SPECFEM3D package. To discretize the geometry, either the internal mesher or an external mesher (e.g., Gmsh [108], CUBIT [109]) can be used. However, to be able to use high-order elements than the conventional 8-node brick element and to handle finite fault sources, which is required for near-field studies, an external mesher is needed. Currently, the package supports up to 27-node hexahedral elements (HEX27) in simulations. Apart from geometry, anisotropy and material dissipation can also be employed to accommodate wave polarization and attenuation. Furthermore, in addition to viscoelastic and pure elastic materials, poroelastic materials can be utilized for the realistic modeling of

granular soils.

To handle absorbing boundaries to avoid numerical instabilities and to prevent synthetic records from distortion due to reflected waves from domain boundaries, the package offers both Clayton-Engquist absorbing boundary conditions [110] and Convolution Perfectly Matched Layers (C-PML) boundary conditions [111] to be utilized; where in the former the artificial dampers are used along boundary edges relating the surface tractions with the shear wave velocity, whereas in the latter complex coordinates are employed to stretch boundaries creating artificial absorbing layers along the domain edges.

Representation of coupled solid-fluid domains is, too, possible with the SPECFEM3D Cartesian package. Yet, it is restricted to modeling linear elastic compressible fluids and hence cannot handle non-linear and viscous fluid behavior. Furthermore, viscoplastic material models are also not readily available to implement realistic soil behavior on shallow layers that are significant to structural and geotechnical engineering applications.

Figure 4.3 illustrates the workflow of the SPECFEM3D package. The first step involves creating and discretizing the geometry. In the second step, partitioning of the discretized geometry is performed and distributed to processors for parallel processing. In this step, if an external mesher is used, the SCOTCH library [112], accommodating efficient mesh partitioning schemes, must be installed. On the other hand, if the internal mesher is used, it is sufficient to edit the number of processors in the `Mesh_par_file` for mesh partitioning. Once the mesh partitioning step is done, a database is constructed, which assigns the Gauss-Legendre-Lobatto (GLL) points and material properties to distributed mesh blocks and creates all the necessary data before the execution of the solver. Once the database creation is successful, the solver is ready to be run. Before running the solver, the earthquake source and stations on which the synthetic seismograms are to be recorded must be described in `CMTSOLUTION` or `FORCESOLUTION` file depending on the source type and in `STATIONS` file, respectively. If the solver successfully halts, synthetic records can be post-processed for visualization and interpretation regarding the success of the simulation. In the next section, parameters modified for numerical simulations will

be highlighted. For comprehensive reading, the SPECFEM3D Cartesian official manual [113] is referred to the reader.

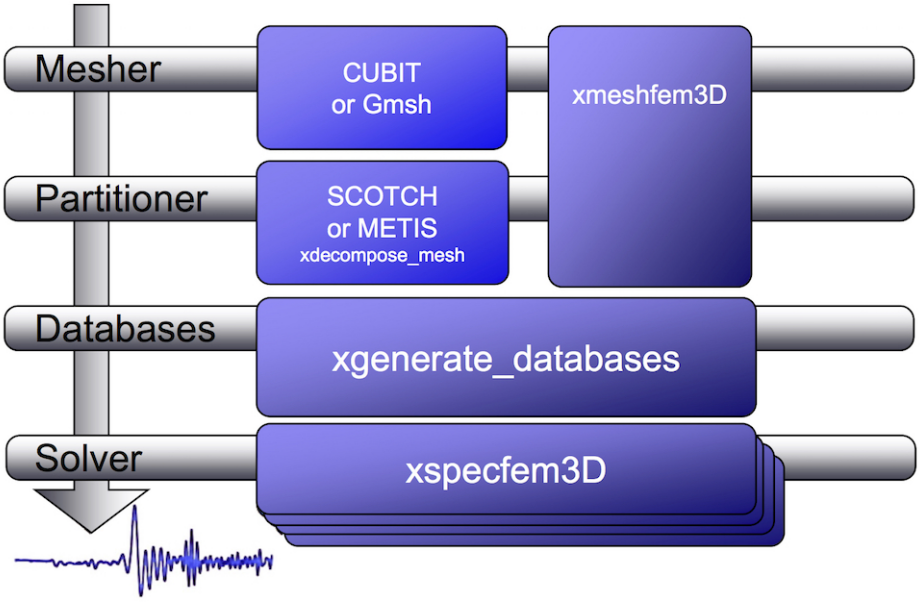

Figure 4.3: General workflow of the SPECFEM3D Cartesian package. In the first stage, the geometry is discretized either by utilizing the internal mesher by executing `xmeshfem3D` or using an external mesher. In the latter case, the mesh is decomposed and distributed to processors employed with the help of SCOTCH library, which provides efficient mesh partitioning schemes, executing `xdecompose_mesh` followed by database generation stage to assign GLL points and corresponding material properties to mesh blocks by `xgenerate_databases`. Once the database generation is done, the solver is run calling the executable `xspecfem3D`.

4.3.1 Parameter Configuration

Before running the solver `xspecfem3D`, the following input files are required.

a) `Par_file` to configure simulation parameters,

b) `CMTSOLUTION` or `FORCESOLUTION` file to represent earthquake source,

c) `STATIONS` file to record synthetic seismograms.

The file `Par_file` includes all necessary configuration parameters required to be set by the user. In this part, only the parameters modified for the simulations are presented. For thorough examination, the official manual is referred. Let us start with the `Par_file`.

`SIMULATION_TYPE` Controls the type of simulation. There are three flags available, 1 for forward simulations, 2 for inverse simulations, and 3 for adjoint simulations. Set to 1.

`UTM_PROJECTION_ZONE` UTM projection zone that the model occupies. For the region under interest, UTM projection zone is set to 35.

`SUPRESS_UTM_PROJECTION_ZONE` Boolean variable. False if the model is specified in geographical coordinates, true if the model is defined in cartesian coordinates instead. Set to `.false.` since the selected stations are given in geographical coordinates.

`NPROC` Number of processors assigned for parallel processing. Set to 12.

`NSTEP` Total number of time steps of the simulation. Set to 15000.

`DT` Duration of each time step determined by Courant's stability criterion. Set to $\Delta t = 7$ ms.

`NGNOD` Number of element nodes. Either HEX8 (brick element) or HEX27 (27-node hexahedral elements) are available. In the case of internal mesher, only HEX8 elements are supported. Set to HEX27

`MODEL` Velocity model to be incorporated. There are two options available to use an external tomographic model. One may set this flag either to `tomo` or to `default`. However, in the latter case, for each element in the mesh a uniqe negative identifier must be defined.

`ATTENUATION` Boolean variable to accommodate attenuation. Set to `.false.` to reduce memory requirements.

ANISOTROPY Boolean variable to incorporate anisotropy. Set to `.false.` to consider only linear isotropic elastic case.

TOMOGRAPHY_PATH Path to tomography files incorporated if an external model is used. Set to the directory in which `tomographyfile.xyz` resides.

USE_OLSEN_ATTENUATION Boolean variable to activate Olsen's attenuation that is adjusted in accordance with the shear wave speed. Set to `.false.`.

PML_CONDITIONS Boolean variable to switch C-PML boundary conditions on. Set to `.false.`.

PML_INSTEAD_OF_FREE_SURFACE Boolean variable to switch C-PML boundary conditions on the free surface. Set to `.false.`.

STACEY_ABSORBING_CONDITIONS Boolean variable to switch Clayton-Engquist absorbing boundary conditions on. Set to `.true.`.

STACEY_INSTEAD_OF_FREE_SURFACE Boolean variable to switch Clayton-Engquist absorbing boundary conditions on the top free surface. Set to `.false.`.

BOTTOM_FREE_SURFACE Boolean variable to switch Clayton-Engquist absorbing boundary conditions on the bottom free surface provided that `STACEY_ABSORBING_CONDITIONS` is set to `.true.`. Set to `.false.`.

USE_FORCE_POINT_SOURCE Boolean variable to switch force point source on. By default, moment-tensor source is read by the solver from the file `CMTSOLUTION`. Set to `.false.`.

USE_RICKER_TIME_FUNCTION Boolean variable to switch Ricker source time function on. Set to `.false.`.

GPU_MODE Boolean variable to enable GPU use. Set to `.true.`.

Table 4.1: Location, given in geographical coordinates, date, and the moment tensor solution of the source.

Moment Tensor Components (in dyn-cm)					
M_{rr}	$M_{\theta\theta}$	$M_{\phi\phi}$	$M_{r\theta}$	$M_{r\phi}$	$M_{\theta\phi}$
-3.47+E26	-3.69+E26	-2.18+E25	-1.38+E26	1.66+E25	-4.44+E25

Date	Centroid Time: 11:51:34.8 GMT 30 October 2020
Latitude	37.91°
Longitude	26.78°
Depth	12.0 km
Half Duration	1.8 s
Strike	276°
Dip	34°
Slip	-90°
M_W	7.0

4.4 Earthquake Source Model

The earthquake source in the model is selected as a point source as the source is sufficiently far from the stations with which comparisons are to be made. However, to be able to accurately simulate near-field effects of the event, a finite fault model will be implemented in future studies as recommended in Chapter 5. Table 4.1 highlights the Global Centroid-Moment-Tensor (GCMT) solution retrieved from the Harvard Catalogue www.globalcmt.org as a source to implement in simulations.

4.5 Compressional and Shear Wave Velocity Models

To be able to model basin effects observed in the region, a high-resolution seismic velocity profile of the region of interest up to engineering bedrock is often needed for accurate and reliable results. However, since the selected region is considerably large including the Aegean Sea, and due to inadequate velocity data in the literature for the

whole region, it could not be achieved to obtain a high-resolution profile. Table 4.2 lists stations used to construct velocity profile that are taken from AFAD database. The maximum available depth for both shear and compressional wave velocities is 32 m for all stations.

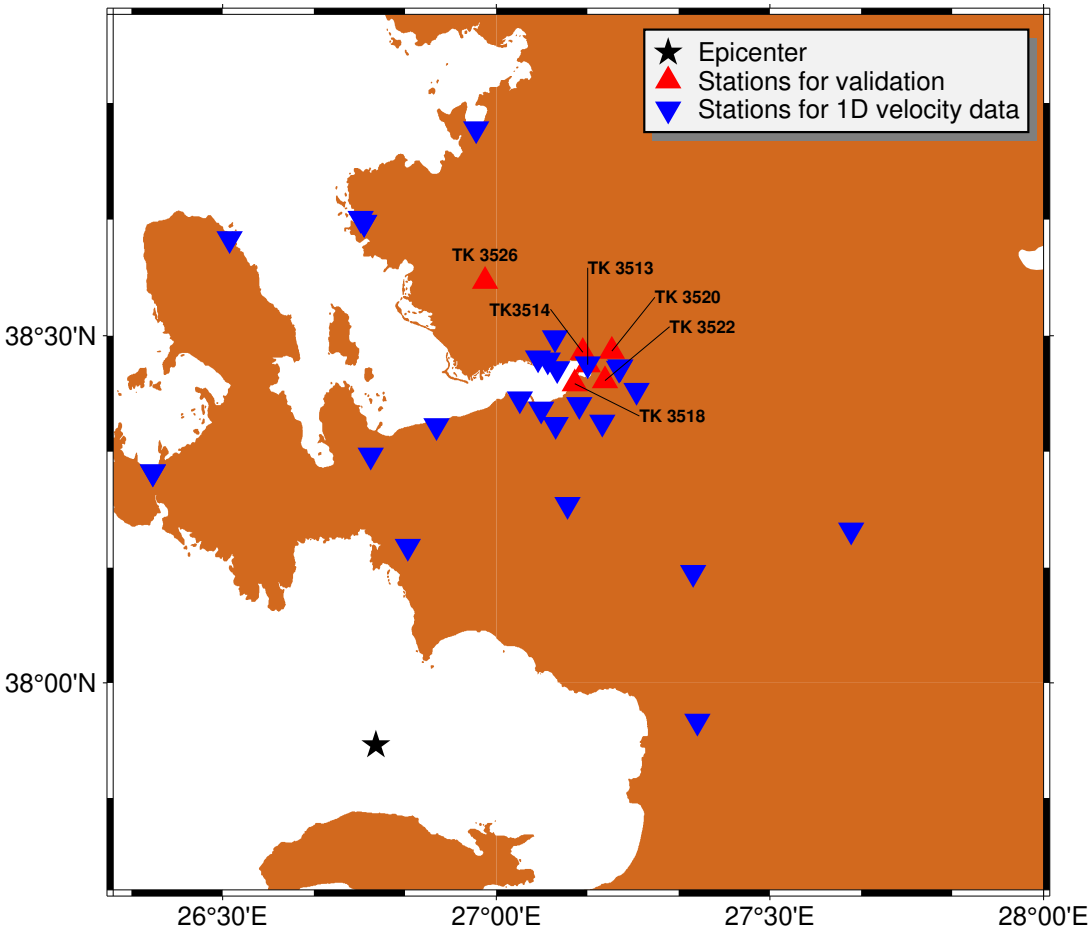

Figure 4.4: Stations used to construct velocity model. Triangles in red are the selected stations to compare synthetic seismograms with the observed recordings.

The first 32 m depth is hence modeled via scattered interpolation of the available velocity data to obtain a three-dimensional velocity profile of the study area. Regions that are outside of the interpolation range are modeled with a constant velocity as a continuation of the interpolated velocities. Extrapolation was also tested, however, yielded rather unrealistic and nonsensical results. Between $32 - 3000$ m, Preliminary Earth Model (PREM1D) [114] is integrated into the model by linearly interpolating velocities at depth 32 m up to 3000 m. Having obtained a homogeneous velocity profile, only PREM data is used until the final depth of 22000 m.

The water layer was attempted to incorporate in the model as well, yet in the meshing stage, the geometry of the region could not be modeled due to rugged topography necessitating very fine mesh sizes at rugged surfaces. Therefore, tomographic model is used to approximately include the sea layer.

Table 4.2: Station list located in İzmir city to construct the tomographic model. Retrieved from AFAD https://tadas.afad.gov.tr

Network	Code	Latitude	Longitude	Elevation (m)	V_{s30} (m/s)	District
TK	3501	38.459	27.167	15	196	Bayraklı
TK	3502	38.455	27.227	35	270	Bornova
TK	3503	39.074	26.889	3	193	Dikili
TK	3504	38.662	26.759	13	328	Foça
TK	3505	38.668	26.752	-	384	Foça
TK	3506	38.394	27.082	26	771	Konak
TK	3507	38.304	26.373	-	1030	Çeşme
TK	3508	39.088	27.375	71	558	Kınık
TK	3509	38.216	27.965	112	286	Ödemiş
TK	3510	38.409	27.043	3	313	Balçova
TK	3511	38.421	27.257	76	827	Bornova
TK	3512	38.401	27.152	79	468	Buca
TK	3513	38.458	27.167	2	196	Bayraklı
TK	3514	38.476	27.158	197	836	Bayraklı
TK	3515	38.465	27.094	4	171	Karşıyaka
TK	3516	38.371	26.891	17	460	Güzelbahçe
TK	3517	38.376	27.194	136	695	Buca
TK	3518	38.431	27.144	7	298	Konak
TK	3519	38.453	27.111	10	131	Karşıyaka
TK	3520	38.478	27.211	184	875	Bornova
TK	3521	38.468	27.0764	1	145	Karşıyaka
TK	3522	38.434	27.199	68	249	Bornova
TK	3523	38.328	26.771	76	414	Urla

TK	3524	38.497	27.107	64	459	Karşıyaka
TK	3525	38.372	27.108	106	745	Karabağlar
TK	3526	38.578	26.980	6	205	Menemen
TK	3527	38.639	26.513	60	207	Karaburun
TK	3528	38.304	26.373	17	532	Çeşme
TK	3529	37.944	27.368	15	306	Selçuk
TK	3530	38.453	27.224	35	270	Bornova
TK	3531	38.220	27.649	104	271	Bayındır
TK	3532	38.1591	27.360	39	328	Torbalı
TK	3533	38.257	27.130	127	415	Menderes
TK	3534	38.662	26.759	13	328	Foça
TK	3535	38.796	26.963	17	361	Aliağa
TK	3536	38.197	26.838	34	1141	Seferihisar
TK	3537	39.109	27.171	52	608	Bergama

4.6 Numerical Details of Simulations

The simulation region covers a volume of 139km $\times$ 133km $\times$ 22km ranging between longitudes 26.3E $-$ 28.0W and between latitudes 37.7N $-$ 39.0N. In the simulation step, the first attempt was made to be able to include the topography and bathymetry data in the model. Yet, due to mountainous shape of the region and rugged surfaces around coastal zones made the meshing process very challenging. Hence, topography could not be included in simulations as it requires very fine grids around those locations distorting the mesh quality. To be able to achieve a smooth meshing process, an external geometric data file is therefore needed to be constructed first, which will be done in the scope of the TUBITAK-MAG project (Project No. 221M169) during 2022-2025.

The second attempt was to include the fluid-solid coupling beneath the sea and near coastal zones. Due to the absence of bathymetry data, a constant water layer depth is used and the domain is decomposed into several parts. In this case, however, although

the meshing process was successful absorbing boundaries on each edge could not be incorporated into the model due to the inaccurate decomposition of small surfaces during the meshing process.

In the third step, the region is decomposed into three distinct layers given in Figure 4.6, the first layer ranging from $0m$ to $3000m$, the second layer ranging from $3000m$ to $15000m$, and finally the third layer ranging from $15000m$ to $22000m$. The decomposition is made in accordance with the velocity models included. For the first layer, a tomographic model, constructed with the AFAD database obtained from the stations shown in Figure 4.4 in combination with PREM1D is used, while the second and the third layers are modeled in accordance with the PREM1D only. Table 4.3. highlights the model parameters. In addition, the density of the top layer is selected as constant having a value of $\rho = 2600$ kg/m^3.

Table 4.3: Decomposition of the model into three subdomains.

Model Data						
Depth (km)	Domain	α (m/s)	β (m/s)	$\rho\,(kg/m^3)$	$Q_\kappa\,(-)$	$Q_\mu\,(-)$
0-3	elastic	`tomographyfile.xyz`				
3-15	elastic	5800	3200	2600	∞	∞
15-22	elastic	6800	3800	2900	∞	∞

In Table 4.3, the attenuation parameters Q_κ and Q_μ are numerically set to 9999 to simulate purely elastic wave propagation without attenuation.
In addition, `tomographyfile.xyz` file contains externally employed material parameters for each grid point given in cartesian coordinates. A total of $n_{el} = 535392$ spectral elements are employed in simulations with the minimum characteristic length size $\Delta h = 500$ m. Furthermore, the time step is selected as $\Delta t = 7$ms to maintain stability as per Courant stability criterion given by (4.2) and simulations were run through 15000 steps (105 seconds). The source is incorporated as a double-couple moment source obtained from Harvard Global CMT Catalog. The time rate of the source is modeled as a Gaussian wavelet with a half duration of $1.8s$. The mesh

stability is checked by controlling the spatial resolution with the following criterion.

$$N\Delta x = \frac{V_{\text{s}}}{f_{\text{max}}} = \lambda_{\text{min}} \tag{4.1}$$

where $N = 5$ is the number of grid points per wavelength determined by the order of Lagrange interpolant used to approximate the solution on elements, Δx is the distance between adjacent grid points in an element, V_s is the average shear wave velocity for an element, f_{max} is the maximum resolution desired to be resolved, and λ_{min} is the minimum wavelength to be resolved. Due to large memory requirements, the element size $\Delta h = (N-1)\Delta x$, where N is determined by the number of GLL points used, is selected first and in accordance with (4.1) f_{max} is 0.6 Hz. The Courant stability condition on the other hand is directly determined by the solver in accordance with the following equation.

$$C = \Delta t \left(\frac{V_{\text{s}}}{\Delta x} \right)_{max} \tag{4.2}$$

where C is the Courant number, which is taken as 0.3. In accordance with (4.2), the maximum allowable time step is given by the solver as $\Delta t = 0.0074$s, and hence Δt is selected as 0.007 s. The importance of the Courant stability condition is that it guarantees that waves do not propagate faster than the shear wave velocity in an element.

4.7 Numerical Results and Comparison with Observed Data

4.7.1 Strong Ground Motion Characteristics

Stations TK3506, TK3511 TK3512, TK3513, TK3514, TK3516, TK3517, TK3518, TK3519, TK3520, TK3521, TK3522, TK3523, TK3524, TK3526, TK3527, TK3528, TK3533, TK534, and finally TK3536 are incorporated in the simulations. Stations TK3513, TK3514, TK3518, TK3520, TK3522 and TK3526 are selected for comparison. Strong ground motion characteristics of the selected stations is highlighted in this subsection to have a better interpretation of the synthetic records.

Stations 3513 and 3514 are settled on soft soil deposits with an average shear wave velocity of $V_{\text{s30}} = 196$ m/s (site class D) for the upper 30 m depth and rock with an average shear wave velocity of $V_{\text{s30}} = 836$ m/s for the upper 30 m depth, respectively,

and are both close to Bayraklı district where the severest structural failures took place. Long-period amplification of up to 1.5 s is observed at station TK3513, while no comparable amplification is seen at station TK3514 located in the same district [98]. Similarly, Makra et al. [115] states that the geological interpretation of the existence of two overlaid basins with station TK3514 being located on top of the formations of the older basin and station TK3513 on top of the younger basin overlying the older basin, implies the possibility of the contribution of a greater structure to the amplification at frequencies lower than 0.5 Hz. In addition, Makra also adds that the difference between the maximum amplitudes for frequencies below 1.0 Hz indicates that the surface wave content is pronounced at station TK3513 due to diffraction at the discontinuities around the younger sedimentary basin. Similar to [98], in Gülerce et al. [116], it is shown that stations TK3513, TK3518, and TK3522 which are located within the basin exhibit low V_{s30} values (between 196-298 m/s) and have relatively long seismic bedrock depths conforming to the presence of thick basin fill. Rather complicated interaction between the site and basin amplification is revealed by the long period ground motion content of the strong ground motion records, in agreement with [115]. Stations TK3514 and TK3520, on the other hand, are located at the basin edge, exhibiting relatively high V_{s30} values, 836 m/s, and 875 m/s respectively. Furthermore, seismic bedrock depth is shallower than the stations within the basin. The presence of high energy content in long period (0.5-1.5 s) strong ground motions of the Samos earthquake is observed in all stations selected, regardless of the site class [98], [116]. Figure 4.7 shows the geological map of the İzmir Bay at which ground motion stations are located.

4.7.2 Station TK3513

Station TK 3513 is located in İzmir City Bayraklı District with an Rjb distance of 85.63 km implying that the point source approximation made in numerical simulations can be acceptable on synthetic records obtained from this station. Moreover, rather low V_{s30} velocity of the location suggests pronounced low frequency ground motions as it might be observed from Table 4.4 and from Figure 4.8. In Figure 4.8, the Fourier Amplitude Spectra of both synthetic and observed records, which are low-pass filtered with a cut-off frequency of $f_c = 0.6$ Hz, show an acceptable match in

pattern between $0.05-0.6$ Hz in both directions. On the other hand, the amplitudes of synthetic records obtained are greater in magnitude than the observed data. Furthermore, a rather crude form of the velocity model used in simulations would probably introduce additional errors in synthetic records. Moreover, when the time series pattern of recordings is observed, the real records are seemed to be delayed. This might be due to the poor representation of the water layer in the model as residual shear waves due to the non-zero velocity layer might introduce additional noise. The amplification due to soft soil conditions on site, on the other hand, can be observed as well from Figure 4.8. Finally, Table 4.5 highlights the misfit of both PGA and FAS data. To find the misfit in the frequency domain and between the PGA values in all stations, the misfit function by Karimzadeh [118] is incorporated as follows.

$$\text{Misfit}_{PGA} = \left| \frac{PGA_{\text{synth}}}{PGA_{\text{obs}}} \right| - 1 \quad \text{and} \quad \text{Misfit}_{FAS} = \frac{1}{n_f} \sum_{f} \left| \log\left(\frac{FAS_{\text{synth}(f)}}{FAS_{\text{obs}}(f)} \right) \right| \tag{4.3}$$

where n_f is the number of discrete frequencies employed.

Table 4.4: Station TK 3513

Station	ID	Latitude	Longitude	V_{s30} (m/s)	Rjb (km)	Province	District
TK	3513	38.456	27.167	196	85.63	İzmir	Bayraklı

Table 4.5: PGA and FAS misfits of synthetic and observed records at TK3513

PGA (m/s^2)		PGV (m/s)				
Real	Synthetic	Real	Synthetic	Misfit_{PGA}	Misfit_{FAS}	Direction
0.25	0.50	0.05	0.29	0.99	1.12	E-W
0.20	0.41	0.05	0.28	1.10	1.08	N-S

4.7.3 Station TK3514

Similar to Station TK 3513, Station TK 3514 is located in İzmir City Bayraklı District having Rjb distance of 86.77 km. However, when compared to TK 3513, it comprises

higherV_{s30} velocity and hence a stiffer soil profile. Therefore, low frequency ground motions are not as much pronounced as in the case of TK 3513, and can be observed from Table 4.6 and from Figure 4.9. In Figure 4.9, the low-pass filtered ($f_c = 0.6$ Hz) Fourier Amplitude Spectra of both synthetic and observed records are shown. However, in this case, amplitudes are almost three times lower than the ones observed in TK 3513, which might qualitatively indicate the stiffer soil condition on the site. The rather crude form of the velocity model used in simulations would probably introduce additional errors in synthetic records. Unlike in the case of TK3513, site amplification is not pronounced due to stiff soil conditions. Table 4.7 highlights the goodness of fit of PGA and FAS data.

Table 4.6: Station TK 3514

Station	ID	Latitude	Longitude	V_{s30} (m/s)	Rjb (km)	Province	District
TK	3514	38.4762	27.1581	836	86.77	İzmir	Bayraklı

Table 4.7: PGA and FAS misfits of synthetic and observed records at TK3514

PGA (m/s^2)		PGV (m/s)				
Real	Synthetic	Real	Synthetic	Misfit$_{PGA}$	Misfit$_{FAS}$	Direction
0.07	0.17	0.02	0.17	1.48	0.97	E-W
0.06	0.22	0.01	0.11	2.49	0.97	N-S

4.7.4 Station TK3518

Station TK 3518 is located in İzmir City Konak District having an Rjb distance of 81.97 km. It exhibits low V_{s30} velocity and has a softer soil condition similar to TK 3513. In Figure 4.10, the low-pass filtered ($f_c = 0.6$ Hz) Fourier Amplitude Spectra of both synthetic and observed records are shown. Amplitudes of synthetic records in both directions reach two to four times the amplitudes of real records suggesting that the resolved frequency range is not enough to capture the frequency range of the low frequency ground motions carrying high energy. In the E-W direction, the FAS of both the synthetic and real recordings show a very close match between the

$0.05 - 0.6$ Hz frequency range. In the N-S direction, however, simulated ground motions are four times higher than the real recordings. However, the amplification characteristic of the soft soil condition again is qualitatively observed at least in the E-W direction. Table 4.9 highlights the goodness of fit of PGA and FAS data.

Table 4.8: Station TK 3518

Station	ID	Latitude	Longitude	V_{s30} (m/s)	Rjb (km)	Province	District
TK	3518	38.4312	27.1435	298	81.97	İzmir	Konak

Table 4.9: PGA and FAS misfits of synthetic and observerd records at TK3518

PGA (m/s^2)		PGV (m/s)				
Real	Synthetic	Real	Synthetic	Misfit$_{PGA}$	Misfit$_{FAS}$	Direction
0.22	0.40	0.04	0.29	1.13	0.96	E-W
0.09	0.30	0.03	0.22	3.08	1.06	N-S

4.7.5 Station TK3520

Station TK 3520 is located in İzmir City Bornova District having an Rjb distance of 89.68 km comprising stiffer soil deposit. In Figure 4.11, the low-pass filtered ($f_c = 0.6$ Hz) Fourier Amplitude Spectra of both synthetic and observed records are shown and a close match is observed in the frequency domain. In addition, time series waveforms show also similar patterns. In the E-W direction, amplitudes of the simulated and observed ground motions are relatively close to each other. Hence, the same reasoning might be made similar to previous cases. Table 4.11 highlights the goodness of fit of PGA and FAS data.

4.7.6 Station TK3522

Station TK 3522 is located in İzmir City Bornova District having an Rjb distance of 85.32 km. Although located in the same district, it has a lower V_{s30} value and hence

Table 4.10: Station TK 3520

Station	ID	Latitude	Longitude	V_{s30} (m/s)	Rjb (km)	Province	District
TK	3520	38.478	27.2111	875	89.68	İzmir	Bornova

Table 4.11: PGA and FAS misfits of synthetic and observed records at TK3520

PGA (m/s^2)		PGV (m/s)				
Real	Synthetic	Real	Synthetic	Misfit$_{PGA}$	Misfit$_{FAS}$	Direction
0.11	0.18	0.04	0.11	0.63	0.97	E-W
0.08	0.15	0.02	0.17	1.00	0.98	N-S

a softer soil deposit suggesting a potential soil amplification in the low frequency range. When Figure 4.12 is observed, it is seen that the FAS of synthetic records yields larger amplitudes as the frequency gets lower. The closest match is observed between $0.1-0.6$ Hz range in the E-W, whereas in the N-S direction frequency range of $0.05-0.6$ Hz exhibits good agreement with each other. As in the case of stations located at regions having softer soil deposits, soil amplification is observed in the low frequency range. Table 4.13 highlights the goodness of fit of PGA and FAS data.

Table 4.12: Station TK 3522

Station	ID	Latitude	Longitude	V_{s30} (m/s)	Rjb (km)	Province	District
TK	3522	38.4357	27.1987	249	85.32	İzmir	Bornova

4.7.7 Station TK3526

Station TK 3526 is located in İzmir City Menemen District having an Rjb distance of 89.17 km. Unlike other selected stations, it is located outside the basin as shown in Figure 4.4 and has a lower V_{s30} value and hence a softer soil deposit. When Figure 4.13 is observed, it is seen that there is a close match between the FAS of synthetic

Table 4.13: PGA and FAS misfits of synthetic and observed records at TK3522

PGA (m/s^2)		PGV (m/s)				
Real	Synthetic	Real	Synthetic	Misfit$_{PGA}$	Misfit$_{FAS}$	Direction
0.17	0.35	0.04	0.21	1.03	1.05	E-W
0.13	0.35	0.04	0.22	1.57	0.92	N-S

recordings and the FAS of real recordings in both directions throughout the frequency range of $0.05 - 0.6$ Hz. This might be attributed to the location of the station as it does not reside in the Bornova Basin and is considerably far away from the epicenter. Table 4.15 highlights the goodness of fit of PGA and FAS data.

Table 4.14: Station TK 3526

Station	ID	Latitude	Longitude	V_{s30} (m/s)	Rjb (km)	Province	District
TK	3526	38.5782	26.9795	205	89.17	İzmir	Menemen

Table 4.15: PGA and FAS misfits of synthetic and observed records at TK3526

PGA (m/s^2)		PGV (m/s)				
Real	Synthetic	Real	Synthetic	Misfit$_{PGA}$	Misfit$_{FAS}$	Direction
0.19	0.30	0.05	0.05	0.59	0.97	E-W
0.22	0.40	0.25	0.26	0.82	0.97	N-S

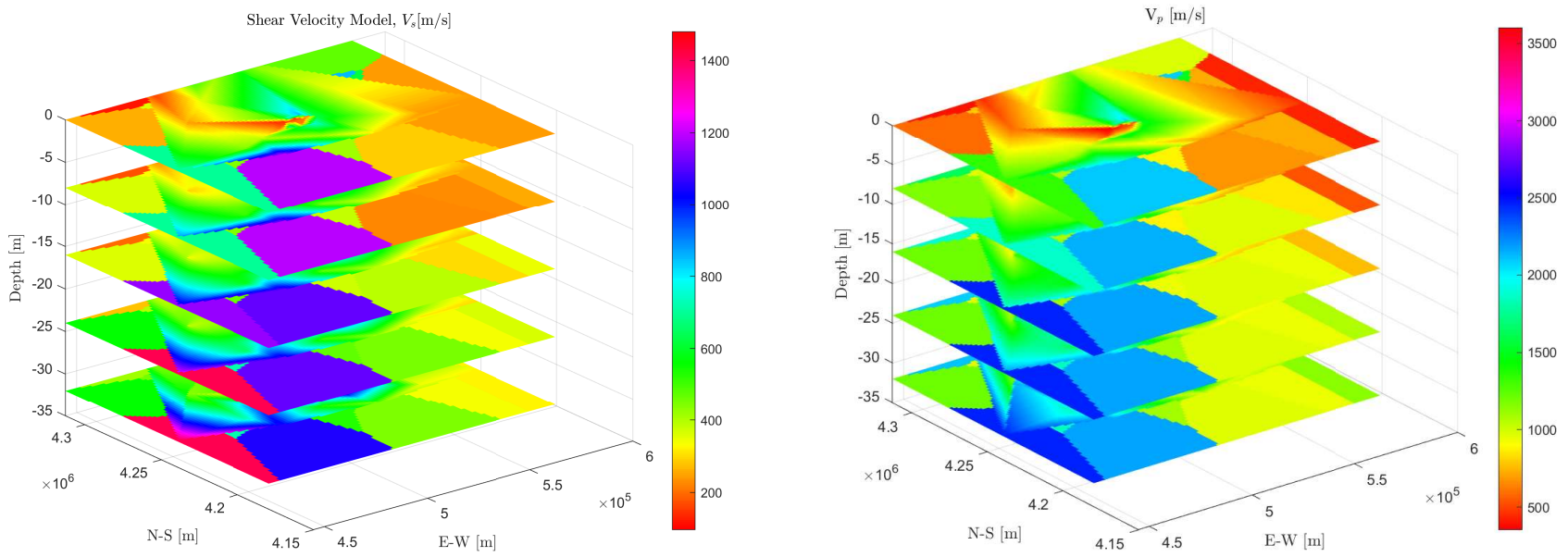

(a) Shear wave velocity (β) model

(b) Compressional wave velocity (α) model

Figure 4.5: Velocity model used in the simulations for the first 30 m depth. Both models are constructed with the interpolation of the dataset obtained from the AFAD database.

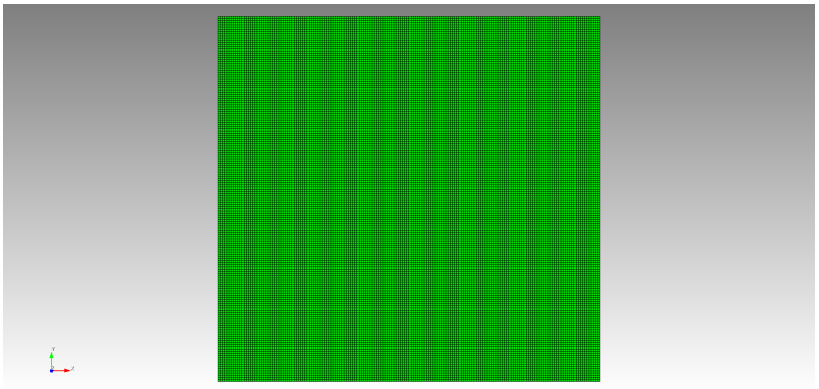

(a) Top view

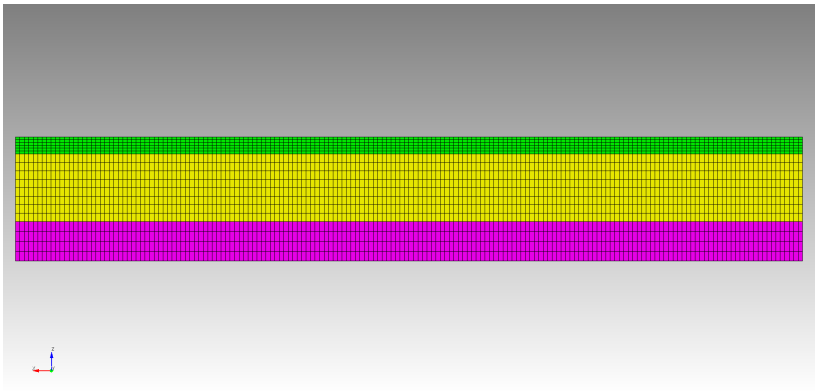

(b) Side view

Figure 4.6: Mesh used in the simulations. Geometry is decomposed into three rectangular prisms. The tomographic velocity model is incorporated into the top layer, while the PREM1D model is applied to bottom layers.

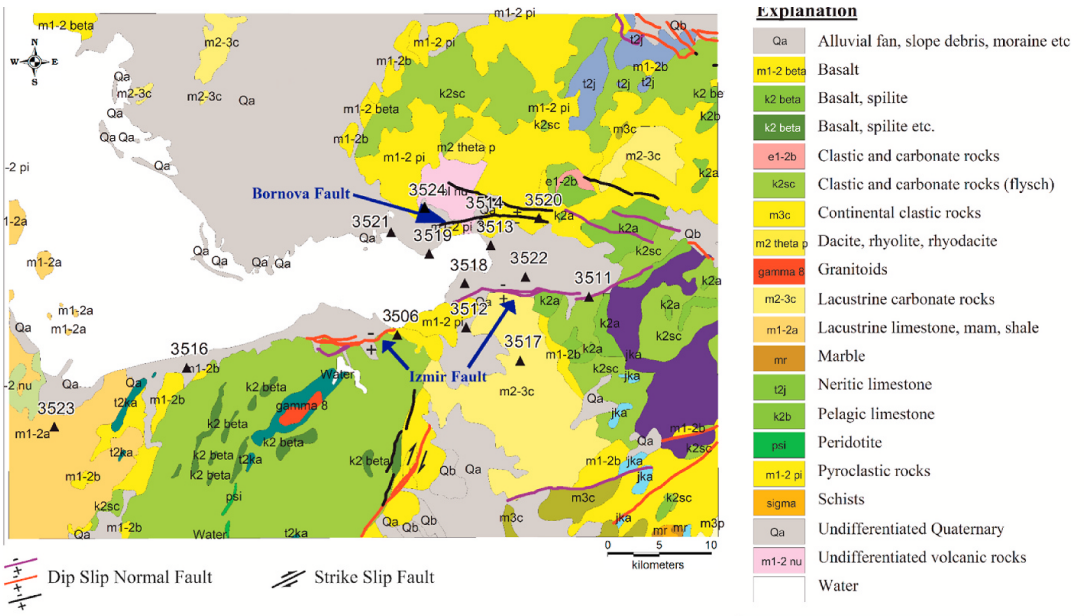

(a) Geological map of the İzmir Bay

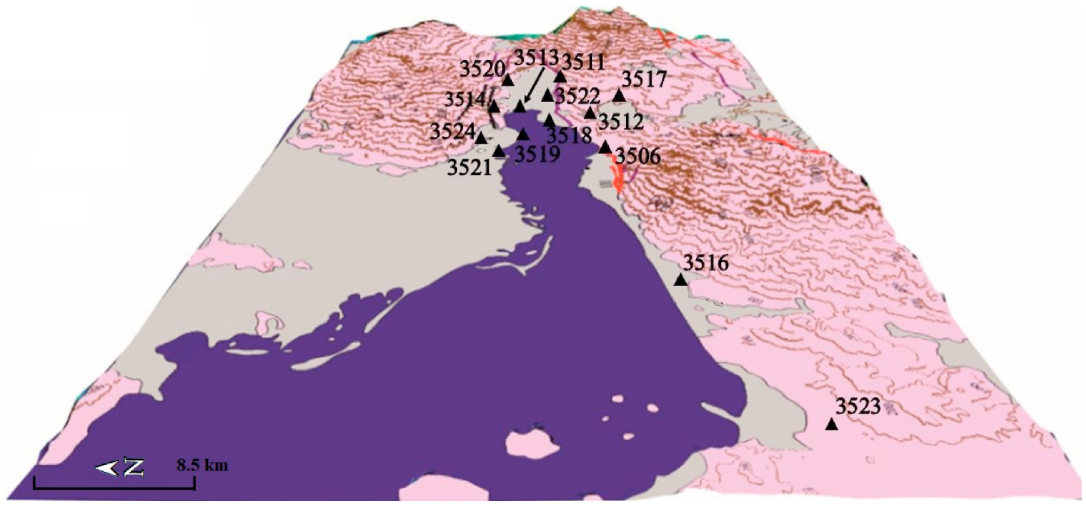

(b) Ground motion stations and 3D site characteristics at which they are located.

Figure 4.7: Close-up view of İzmir Bay illustrating the geological setting of the area. (a) depicts the geological map of the Bornova Basin and its surroundings.(b) shows the positions of ground motion stations located in the basin with color codes characterizing the site on which the stations are settled. The figure is adapted from [117].

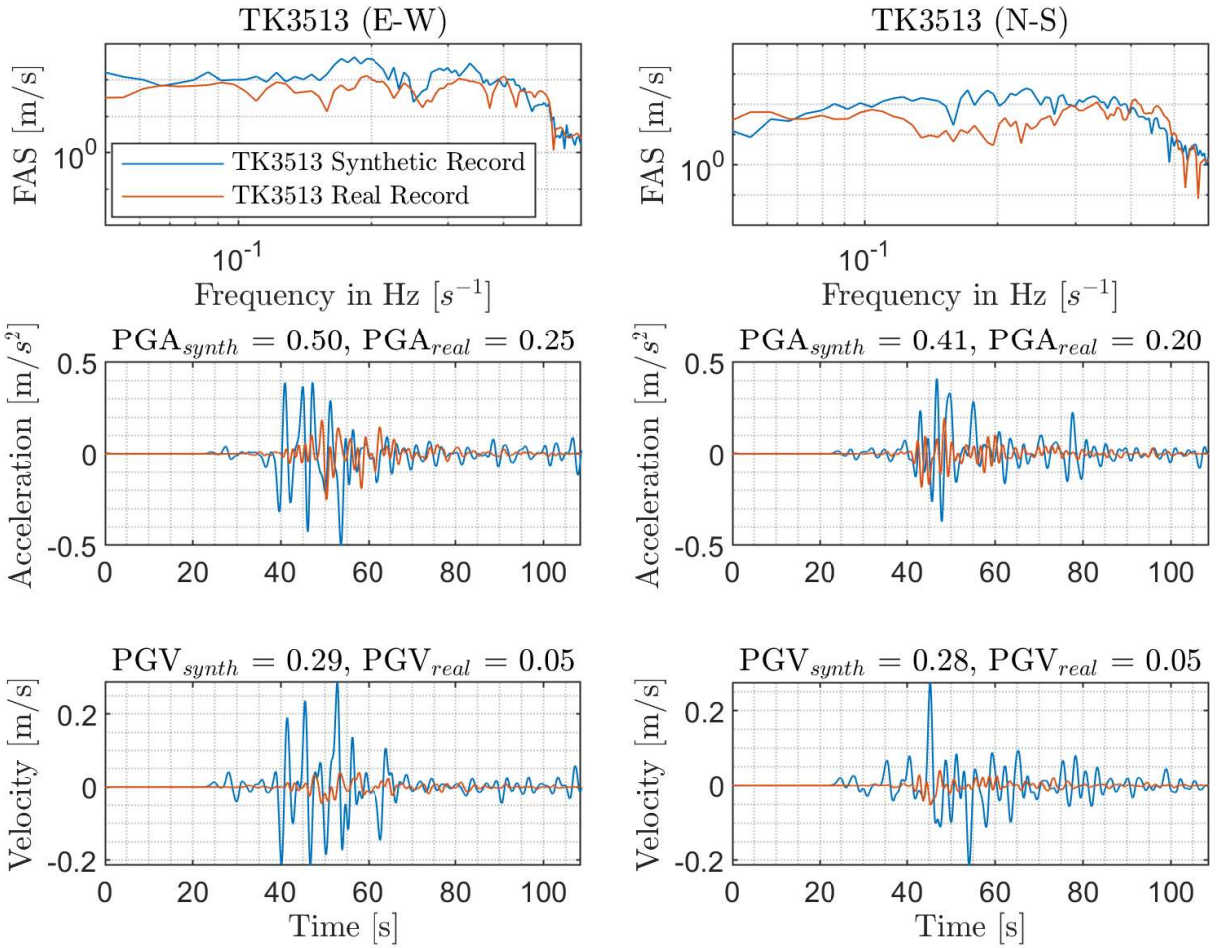

Figure 4.8: Synthetic and observed records at Station TK3513

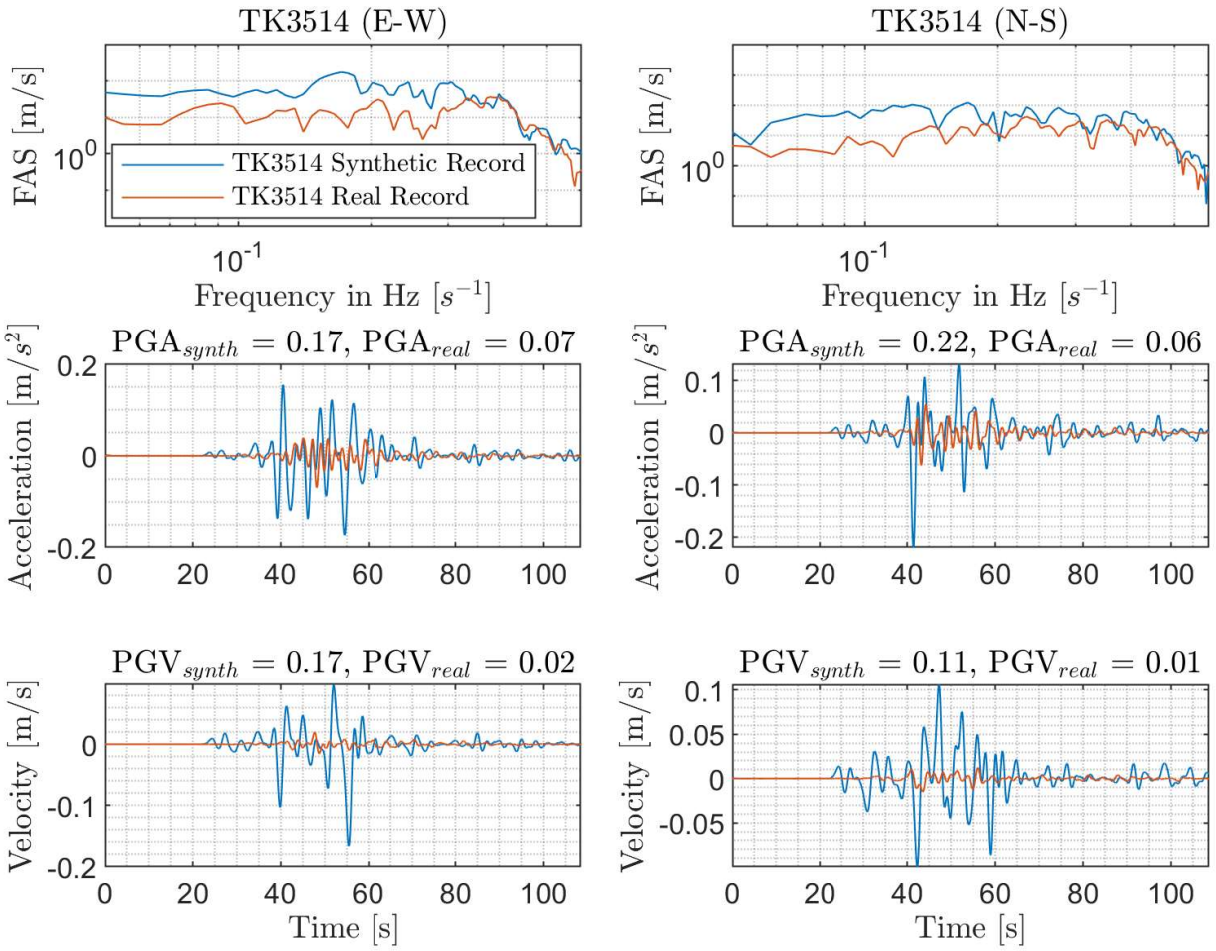

Figure 4.9: Synthetic and observed records at Station TK3514

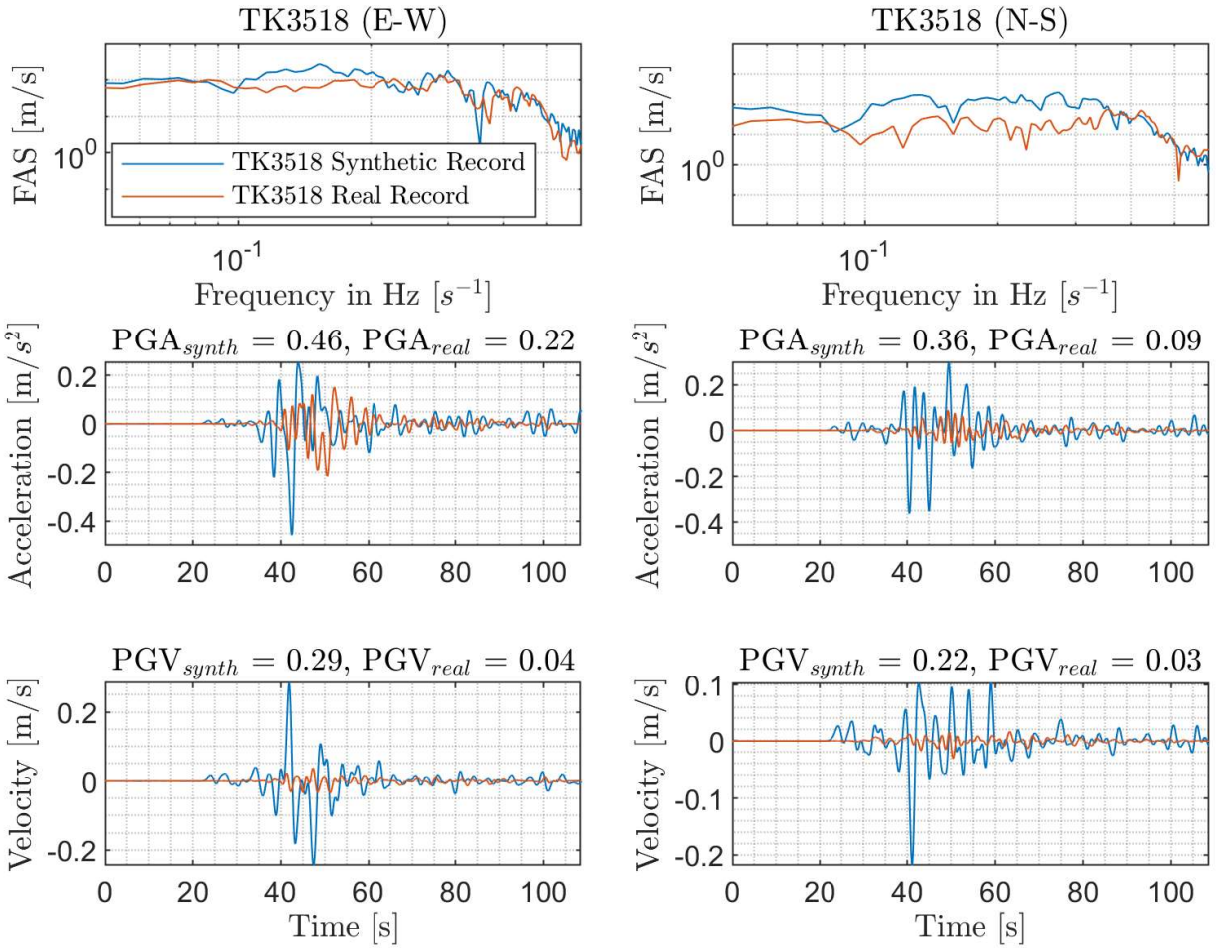

Figure 4.10: Synthetic and observed records at Station TK3518

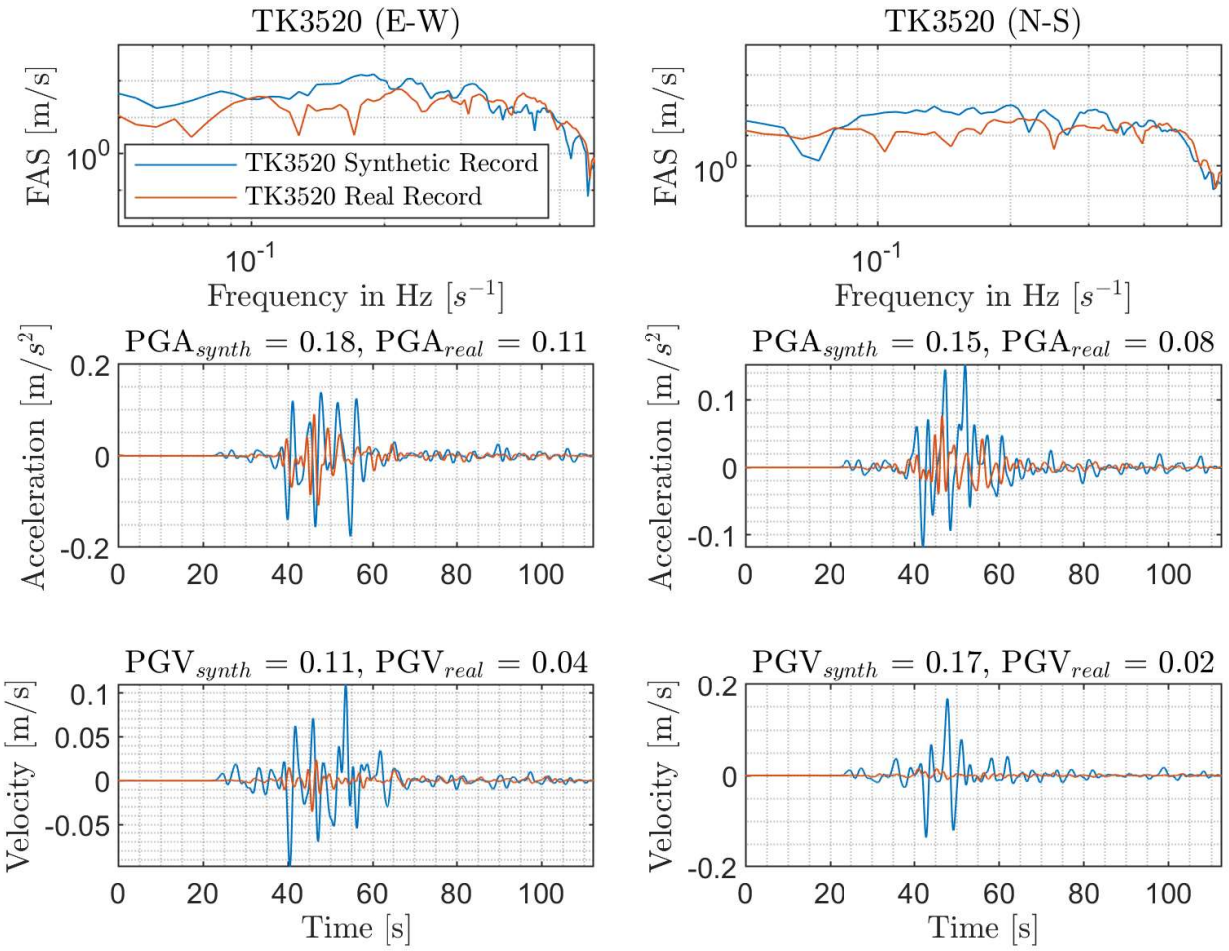

Figure 4.11: Synthetic and observed records of PGA at Station TK3520

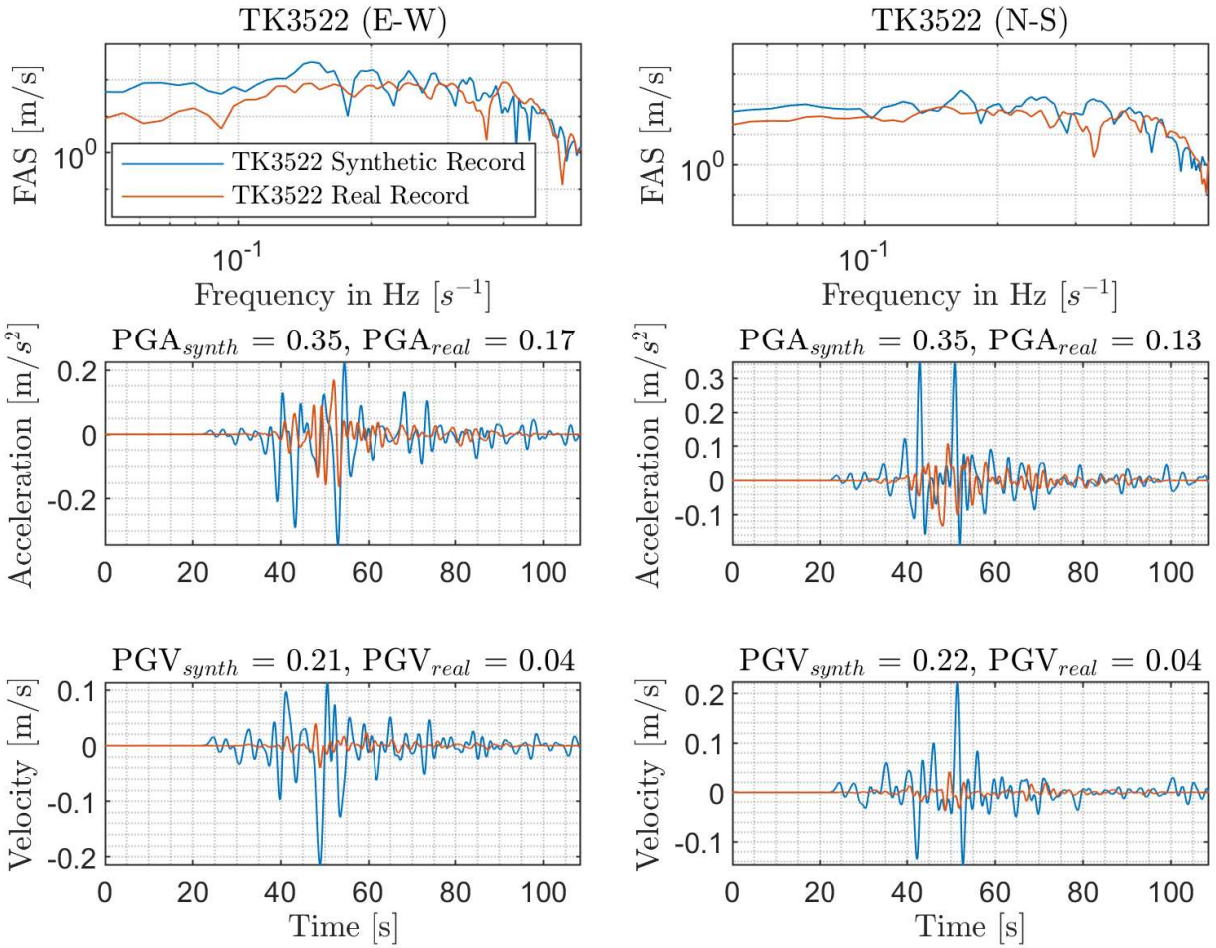

Figure 4.12: Synthetic and observed records of PGA at Station TK3522

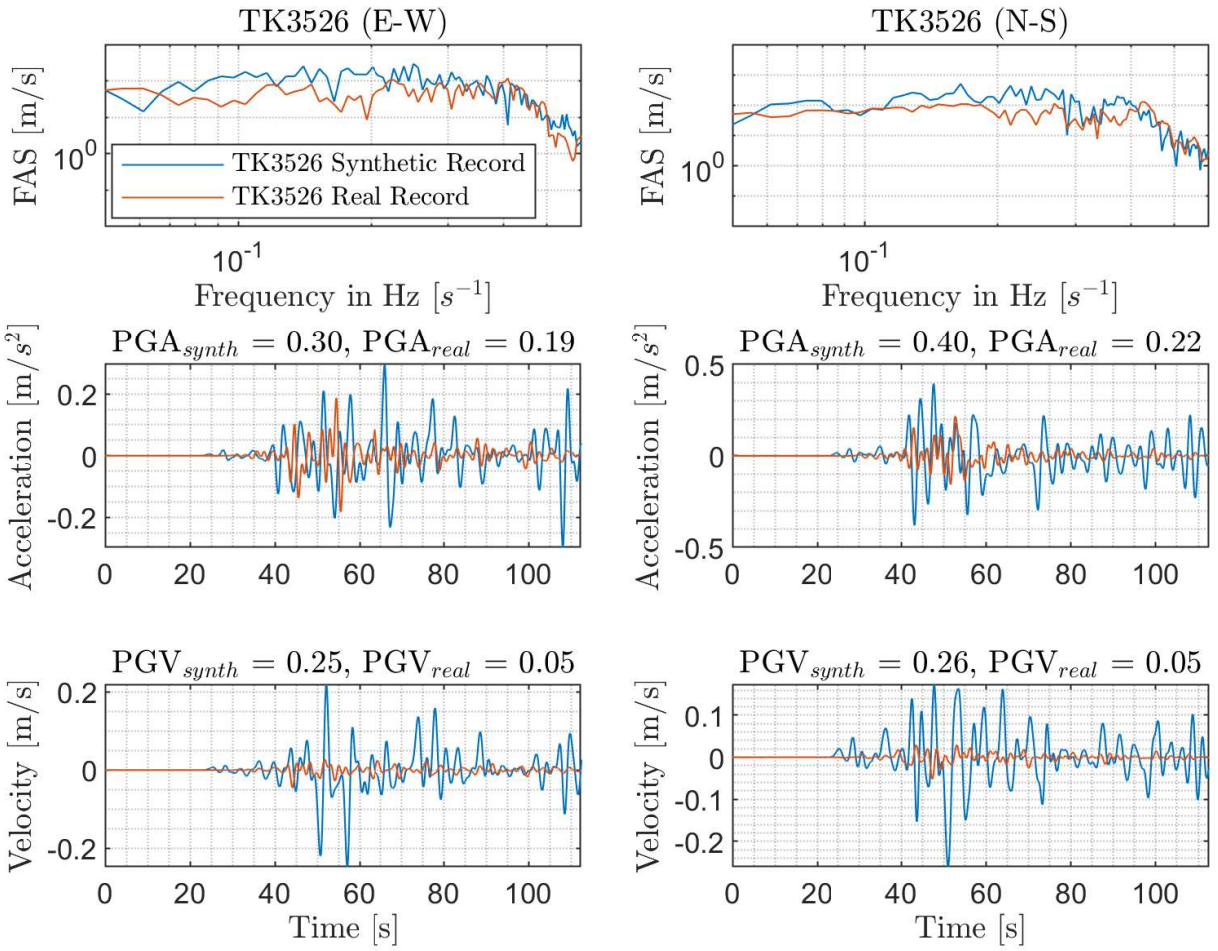

Figure 4.13: Synthetic and observed records of PGA at Station TK3526

CHAPTER 5

CONCLUDING REMARKS

5.1 Summary

In this thesis, low frequency ground motions of the 2020 Samos Earthquake at selected ground motion stations are simulated using the spectral element method. For this purpose, the mathematical derivation of the classical wave equation is derived first. Next, the spatiotemporal discretization scheme involved in finite element and spectral element methods is performed. Then, an initial velocity model of the region is constructed based on the 1D velocity profiles provided by AFAD. For the source model, the moment tensor solution of the Samos Earthquake is utilized with a Gaussian source time function since the event is located at far distances from the studied stations admitting point source model utilization. The comparisons of simulated and observed data are performed in terms of FAS, velocity, and acceleration time history

5.2 Main Findings

Based on the numerical results obtained in this study, the following main conclusions are derived.

- This study constitutes an initial attempt to use spectral elements to model the low frequency ground motions of a large earthquake in Turkey. There are stochastic models of this particular event, but this thesis is the first deterministic attempt to simulate the 2020 Samos Earthquake.
- Point source assumption of the earthquake source provides acceptable esti-

mates. However, the simulated spectral and time domain amplitudes overestimate the observations. In addition, the velocity model affects the accuracy of the results clearly.

- Stations located on softer soil conditions in the Bornova basin exhibit surface waves with longer period content. These waves could also be modeled in the simulations. The structural damage observed in several high-rise buildings can be attributed to surface waves. Thus it is important to model these waves, which is not possible to simulate with stochastic approaches.

- For all cases, the N-S component of simulated ground motions shows an acceptable match with the observed data, whereas amplitudes of U-D components deviate too much from each other. This discrepancy could be due to the issues with the P-wave velocities.

- It is observed that the numerical model could resolve the complete frequency range of $0 - 0.6$ Hz. Simulation of higher frequencies can also be possible in future studies with better-refined velocity models.

- At stations located on soft soils, site amplification effects are observed in both recorded and simulated data. It is particularly significant to capture the local site effects in simulated data.

- The poorest performance is observed at station TK3514 in terms of PGA misfit. This could be considered reasonable as TK3514 stays on a stiff soil deposit in which higher frequency ground motions are pronounced. Therefore, such a deviation is expected as the numerical model is only capable of resolving frequencies up to roughly 0.6 Hz.

- In all cases, FAS misfits are observed to be around the same order, slightly deviating from 1, between the discrete frequencies $0.05 - 0.6$ Hz, which conforms with qualitative inspection of FAS data presented in related figures.

- In all stations selected, the Joyner-Boore distance (Rjb) is computed to be sufficiently large to avoid errors that might be introduced by point source approximation employed in the model. However, in the future, simulation of finite fault models is necessary.

5.3 Future Work

The following articles highlight the assumptions made in this study and propose some points which should be investigated in a detailed manner in future studies.

- This study aimed to simulate only the low frequency portion of the recorded motions. The high frequency portions can be modeled with the stochastic approaches. In the future, it is important to provide broadband motions with a hybrid approach.

- The source model is assumed to be a point source due to large source-to-site distances at the sites in İzmir. However, it is important to model large events with finite fault models in the future to study the near-fault effects.

- The earth model here is an initial approximation based on 1D profiles at AFAD stations. Well-refined velocity models should be formed in the future in order to represent wave propagation better.

- All of the simulations herein are based on purely isotropic elastic materials. In order to be able to simulate the realistic behavior of soils, different material models are needed to be integrated into simulations in future studies.

- In addition, material dissipation due to viscoplastic behavior is not included in the simulations due to considerable memory requirements. Therefore, such dissipative material models are also needed for the purpose of accuracy. Poroelastic soil models would be integrated as well for realistic simulations in future studies.

- To be able to capture the regional geometry realistically, a geometric model constructed from bathymetry and topography data is required to capture topography and sea effects on propagated waves.

- In this thesis, strong motion data is used only for practical purposes to test the spectral element models. Broadband data around the earthquake could be employed in future studies.

- This thesis only involves a first order approximation to the ground motion simulation of the 2020 Samos Earthquake. Due to a lack of regional data and the significant memory requirements of such a large-scale event, it was challenging to include a wide range of phenomena reported during the event in the simulations. However, with the accumulation of regional data during the course of undergoing the TUBITAK-MAG project (Project No. 221M169), it would be possible to construct precise geometry, including the topography as well as the bathymetry, and tomographic model with higher resolution of the region, enabling us to perform higher order simulations.

REFERENCES

[1] F. Amador, "The causes of 1755 lisbon earthquake on kant," *Historia de las ciencias y de las técnicas*, vol. 2, pp. 485–496, 01 2004.

[2] I. Kant, *On the causes of earthquakes on the occasion of the calamity that befell the western countries of Europe towards the end of last year (1756)*, p. 327–336. The Cambridge Edition of the Works of Immanuel Kant, Cambridge: University Press, 2012.

[3] A. Ben-Menahem, "A concise history of mainstream seismology: Origins, legacy, and perspectives," *Bulletin of the Seismological Society of America*, vol. 85, pp. 1202–1225, 08 1995.

[4] M. Bohnoff, F. Bulut, G. Dresen, P. E. Malin, T. Eken, and M. Aktar, "An earthquake gap south of Istanbul," *Nature Communications*, vol. 4, p. 1999, 06 2013.

[5] M. A. Pelissier, H. Hoeber, N. van de Coevering, and I. F. Jones, *Classics of Elastic Wave Theory*. Society of Exploration Geophysicists, 2007. ISBN: 1560801429, doi: https://doi.org/10.1190/1.9781560801931.

[6] L. D. Landau and E. M. Lifshitz, *Mechanics: Volume 1*. Course of Theoretical Physics, Butterworth-Heinemann, 3rd ed., 1976. ISBN: 0750628969.

[7] L. Susskind and G. Hrabovsky, *Classical Mechanics: The Theoretical Minimum*. London: Penguin Books, 2014. ISBN: 0141976228.

[8] S. P. Timoshenko, *History of Strength of Materials*. New York: Dover Publications, 1983. ISBN: 0486611876.

[9] A. E. H. Love, *A Treatise on Mathematical Theory of Elasticity*. Cambridge: University Press, 1892. [Online]. Available: https://archive.org/details/atreatiseonmath03lovegoog.

[10] A. E. H. Love, *Some Problems of Geodynamics: Being an Essay to which the Adams Prize in the University of Cambridge was Adjudged in 1911*. Cambridge: University Press, 1911. [Online]. Available: https://archive.org/details/someproblemsofge00loveuoft.

[11] G. A. Maugin, *Continuum Mechanics through the Ages - From the Renaissance to the Twentieth Century: From Hydraulics to Plasticity*. Solid Mechanics and Its Applications, vol. 223, Switzerland: Springer Cham, 1st ed., 2016. ISBN: 3319265933.

[12] K. Aki and P. G. Richards, *Quantitative Seismology*. USA: University Science Books, 2nd ed., 2002. ISBN: 0935702962.

[13] J. Pujol, *Elastic Wave Propagation and Generation in Seismology*. Cambridge: University Press, 2003. ISBN: 0521817307.

[14] A. Ben-Menahem and S. J. Singh, *Seismic Waves and Sources*. New York: Dover Publications, 2nd ed., 2000. ISBN: 0486404617.

[15] T. Furumura and L. Chen, "Parallel simulation of strong ground motions during recent and historical damaging earthquakes in Tokyo, Japan," *Parallel Computing*, vol. 31, no. 2, pp. 149–165, 2005. Parallel Graphics and Visualization.

[16] P. Moczo, M. Lucká, J. Kristek, and M. Kristeková, "3D Displacement finite differences and a combined memory optimization," *Bulletin of the Seismological Society of America*, vol. 89, pp. 69–79, 02 1999.

[17] P. Moczo, J. Kristek, V. Vavryčuk, R. J. Archuleta, and L. Halada, "3D Heterogeneous Staggered-Grid Finite-Difference Modeling of Seismic Motion with Volume Harmonic and Arithmetic Averaging of Elastic Moduli and Densities," *Bulletin of the Seismological Society of America*, vol. 92, pp. 3042–3066, 12 2002.

[18] P. Moczo, J. O. Robertsson, and L. Eisner, "The Finite-Difference Time-Domain Method for Modeling of Seismic Wave Propagation," in *Advances in Wave Propagation in Heterogenous Earth* (R.-S. Wu, V. Maupin, and R. Dmowska, eds.), vol. 48 of *Advances in Geophysics*, pp. 421–516, Elsevier, 2007.

[19] P. Moczo, J. Kristek, and L. Halada, "3D Fourth-Order Staggered-Grid Finite-Difference Schemes: Stability and Grid Dispersion," *Bulletin of the Seismological Society of America*, vol. 90, pp. 587–603, 06 2000.

[20] A. Frankel and J. Vidale, "A three-dimensional simulation of seismic waves in the Santa Clara Valley, California, from a Loma Prieta aftershock," *Bulletin of the Seismological Society of America*, vol. 82, pp. 2045–2074, 10 1992.

[21] A. Frankel, "Three-dimensional simulations of ground motions in the San Bernardino Valley, California, for hypothetical earthquakes on the San Andreas fault," *Bulletin of the Seismological Society of America*, vol. 83, pp. 1020–1041, 08 1993.

[22] K. Yomogida and J. T. Etgen, "3-D wave propagation in the Los Angeles basin for the Whittier-Narrows earthquake," *Bulletin of the Seismological Society of America*, vol. 83, pp. 1325–1344, 10 1993.

[23] H. Aochi and F. Dupros, "MPI-OpenMP hybrid simulations using boundary integral equation and finite difference methods for earthquake dynamics and wave propagation: Application to the 2007 Niigata Chuetsu-Oki earthquake (Mw6.6)," *Procedia Computer Science*, vol. 4, pp. 1496–1505, 2011. Proceedings of the International Conference on Computational Science, ICCS 2011.

[24] H. Aochi, V. Durand, and J. Douglas, "Influence of Super-Shear Earthquake Rupture Models on Simulated Near-Source Ground Motion from the 1999 Izmit, Turkey, Earthquake," *Bulletin of the Seismological Society of America*, vol. 101, pp. 726–741, 04 2011.

[25] J. Virieux, "P-SV wave propagation in heterogeneous media: Velocity-stress finite-difference method," *GEOPHYSICS*, vol. 51, no. 4, pp. 889–901, 1986.

[26] I. Oprsal and J. Zahradnik, "Three-dimensional finite difference method and hybrid modeling of earthquake ground motion," *Journal of Geophysical Research: Solid Earth*, vol. 107, no. B8, pp. ESE 2–1–ESE 2–16, 2002.

[27] T. Sato, R. W. Graves, and P. G. Somerville, "Three-dimensional finite-difference simulations of long-period strong motions in the Tokyo metropolitan area during the 1990 Odawara earthquake (MJ 5.1) and the great 1923 Kanto

earthquake (MS 8.2) in Japan," *Bulletin of the Seismological Society of America*, vol. 89, pp. 579–607, 06 1999.

[28] S. Aoi, R. Honda, N. Morikawa, H. Sekiguchi, H. Suzuki, Y. Hayakawa, T. Kunugi, and H. Fujiwara, "Three-dimensional finite difference simulation of long-period ground motions for the 2003 Tokachi-oki, Japan, earthquake," *Journal of Geophysical Research: Solid Earth*, vol. 113, no. B7, 2008.

[29] S. Aoi and H. Fujiwara, "3D finite-difference method using discontinuous grids," *Bulletin of the Seismological Society of America*, vol. 89, pp. 918–930, 08 1999.

[30] R. W. Graves, "Three-dimensional finite-difference modeling of the San Andreas fault: Source parameterization and ground-motion levels," *Bulletin of the Seismological Society of America*, vol. 88, pp. 881–897, 08 1998.

[31] G. Tanırcan, "Ground motion simulation for Istanbul with a three dimensional velocity model," *Journal of the Faculty of Engineering and Architecture of Gazi University*, vol. 27, pp. 27–35, 11 2011.

[32] K. Şeşetyan, E. Çaktı, and R. Madariaga, "Engineering Implications of Source Parameters and 3D Wave Propagation Modeling for the 2004 Parkfield, California, Earthquake," *Bulletin of the Seismological Society of America*, vol. 105, pp. 1739–1755, 05 2015.

[33] J. Bielak, O. Ghattas, and E. Kim, "Parallel octree-based finite element method for large-scale earthquake ground motion simulation," *Computer Modeling in Engineering and Sciences*, vol. 10, no. 2, p. 99, 2005.

[34] V. Etienne, E. Chaljub, J. Virieux, and N. Glinsky, "An hp-adaptive discontinuous Galerkin finite-element method for 3-D elastic wave modelling," *Geophysical Journal International*, vol. 183, pp. 941–962, 11 2010.

[35] X. Li, J. Bielak, and O. Ghattas, "Three-dimensional earthquake site response on a CM-2," in *Proceedings of the Tenth World Conference on Earthquake Engineering*, pp. 959–964, 1992.

[36] T. Toshinawa and T. Ohmachi, "Love-wave propagation in a three-dimensional sedimentary basin," *Bulletin of the Seismological Society of America*, vol. 82, pp. 1661–1677, 08 1992.

[37] H. Bao, J. Bielak, O. Ghattas, L. F. Kallivokas, D. R. O'Hallaron, J. R. Shewchuk, and J. Xu, "Large-scale simulation of elastic wave propagation in heterogeneous media on parallel computers," *Computer Methods in Applied Mechanics and Engineering*, vol. 152, no. 1, pp. 85–102, 1998. Containing papers presented at the Symposium on Advances in Computational Mechanics.

[38] P. Moczo, J. Kristek, M. Galis, P. Pazak, and M. Balazovjech, "The finite-difference and finite-element modeling of seismic wave propagation and earthquake motion," *Acta physica slovaca*, vol. 57, no. 2, 2007.

[39] G. Cohen, P. Joly, and N. Tordjman, "Higher-order finite elements with mass-lumping for the 1D wave equation," *Finite Elements in Analysis and Design*, vol. 16, no. 3, pp. 329–336, 1994. Special Issue Selection of Papers Presented at ICOSAHOM'92.

[40] E. Priolo, J. M. Carcione, and G. Seriani, "Numerical simulation of interface waves by high-order spectral modeling techniques," *The Journal of the Acoustical Society of America*, vol. 95, no. 2, pp. 681–693, 1994.

[41] G. Seriani and E. Priolo, "Spectral element method for acoustic wave simulation in heterogeneous media," *Finite Elements in Analysis and Design*, vol. 16, no. 3, pp. 337–348, 1994. Special Issue Selection of Papers Presented at ICOSAHOM'92.

[42] D. Komatitsch and J.-P. Vilotte, "The spectral element method: An efficient tool to simulate the seismic response of 2D and 3D geological structures," *Bulletin of the Seismological Society of America*, vol. 88, pp. 368–392, 04 1998.

[43] D. Komatitsch and J. Tromp, "Spectral-element simulations of global seismic wave propagation—I. Validation," *Geophysical Journal International*, vol. 149, pp. 390–412, 05 2002.

[44] D. Komatitsch, J.-P. Vilotte, R. Vai, J. M. Castillo-Covarrubias, and F. J. Sánchez-Sesma, "The spectral element method for elastic wave equations—application to 2-D and 3-D seismic problems," *International Journal for Numerical Methods in Engineering*, vol. 45, no. 9, pp. 1139–1164, 1999.

[45] D. Komatitsch, F. Coutel, and P. Mora, "Tensorial formulation of the wave equation for modelling curved interfaces," *Geophysical Journal International*, vol. 127, pp. 156–168, 10 1996.

[46] D. Komatitsch, G. Erlebacher, D. Göddeke, and D. Michéa, "High-order finite-element seismic wave propagation modeling with MPI on a large GPU cluster," *Journal of Computational Physics*, vol. 229, no. 20, pp. 7692–7714, 2010.

[47] D. Komatitsch, Q. Liu, J. Tromp, P. Süss, C. Stidham, and J. H. Shaw, "Simulations of Ground Motion in the Los Angeles Basin Based upon the Spectral-Element Method," *Bulletin of the Seismological Society of America*, vol. 94, pp. 187–206, 02 2004.

[48] D. Komatitsch, C. Barnes, and J. Tromp, "Wave propagation near a fluid-solid interface: A spectral-element approach," *GEOPHYSICS*, vol. 65, no. 2, pp. 623–631, 2000.

[49] D. Michéa and D. Komatitsch, "Accelerating a three-dimensional finite-difference wave propagation code using GPU graphics cards," *Geophysical Journal International*, vol. 182, pp. 389–402, 07 2010.

[50] F. Di Michele, J. May, D. Pera, V. Kastelic, M. Carafa, C. Smerzini, I. Mazzieri, B. Rubino, P. F. Antonietti, A. Quarteroni, R. Aloisio, and P. Marcati, "Spectral element numerical simulation of the 2009 L'Aquila earthquake on a detailed reconstructed domain," *Geophysical Journal International*, vol. 230, pp. 29–49, 02 2022.

[51] E. Casarotti, M. Stupazzini, S. J. Lee, D. Komatitsch, A. Piersanti, and J. Tromp, "CUBIT and Seismic Wave Propagation Based Upon the Spectral-Element Method: An Advanced Unstructured Mesher for Complex 3D Geological Media ," in *Proceedings of the 16th International Meshing Roundtable*

(M. L. Brewer and D. Marcum, eds.), (Berlin, Heidelberg), pp. 579–597, Springer Berlin Heidelberg, 2008.

[52] E. Chaljub, D. Komatitsch, J.-P. Vilotte, Y. Capdeville, B. Valette, and G. Festa, "Spectral-element analysis in seismology," in *Advances in Wave Propagation in Heterogenous Earth* (R.-S. Wu, V. Maupin, and R. Dmowska, eds.), vol. 48 of *Advances in Geophysics*, pp. 365–419, Elsevier, 2007.

[53] H. Kawase, "Time-domain response of a semi-circular canyon for incident SV, P, and Rayleigh waves calculated by the discrete wavenumber boundary element method," *Bulletin of the Seismological Society of America*, vol. 78, pp. 1415–1437, 08 1988.

[54] J. E. Luco, H. L. Wong, and F. C. P. De Barros, "Three-dimensional response of a cylindrical canyon in a layered half-space," *Earthquake Engineering & Structural Dynamics*, vol. 19, no. 6, pp. 799–817, 1990.

[55] H. A. Pedersen, F. J. Sánchez-Sesma, and M. Campillo, "Three-dimensional scattering by two-dimensional topographies," *Bulletin of the Seismological Society of America*, vol. 84, pp. 1169–1183, 08 1994.

[56] M. Bouchon and K. Aki, "Discrete wave-number representation of seismic-source wave fields," *Bulletin of the Seismological Society of America*, vol. 67, pp. 259–277, 04 1977.

[57] M. Bouchon, "A simple method to calculate Green's functions for elastic layered media," *Bulletin of the Seismological Society of America*, vol. 71, pp. 959–971, 08 1981.

[58] Y. Hisada, "An efficient method for computing Green's functions for a layered half-space with sources and receivers at close depths," *Bulletin of the Seismological Society of America*, vol. 84, pp. 1456–1472, 10 1994.

[59] X. Chen and H. Zhang, "An Efficient Method for Computing Green's Functions for a Layered Half-Space at Large Epicentral Distances," *Bulletin of the Seismological Society of America*, vol. 91, pp. 858–869, 08 2001.

[60] S. H. Hartzell, "Earthquake aftershocks as Green's functions," *Geophysical Research Letters*, vol. 5, no. 1, pp. 1–4, 1978.

[61] K. Irikura, "Prediction of strong acceleration motion using empirical Green's function," in *Proc. 7th Japan Earthq. Eng. Symp*, vol. 151, pp. 151–156, 1986.

[62] E. Ozmen, S. Karimzadeh, and A. Askan, "Broadband ground motion simulation within the city of Düzce (Turkey) and building response simulation," *Pure and Applied Geophysics*, vol. 177, no. 5, pp. 2353–2373, 2020.

[63] A. Sahin, R. Sisman, A. Askan, and M. Hori, "Development of integrated earthquake simulation system for Istanbul," *Earth, Planets and Space*, vol. 68, no. 1, pp. 1–21, 2016.

[64] G. F. Roach, *Green's Functions*. Cambridge: University Press, 2nd ed., 1982. ISBN: 0521282888.

[65] A. Erdélyi, *Tables of Integral Transforms: Based, in part, on notes left by Harry Bateman*, vol. 1. New York: McGraw-Hill, 1954. ISBN: 0070195498.

[66] K. Watanabe, *Integral Transform Techniques for Green's Function*. Lecture Notes in Applied and Computational Mechanics, vol. 76, Switzerland: Springer International Pub., 2nd ed., 2015. ISBN: 3319174556, doi: https://doi.org/10.1007/978-3-319-17455-6.

[67] J. D. Achenbach, *Elastic Wave Propagation and Generation in Seismology*. North-Holland Series in Applied Mathematics and Mechanics, vol. 16, New York: American Elsevier Pub. Co., 1973. ISBN: 0444104658.

[68] J. R. S. Rayleigh, *The Theory of Sound, Vol. I.* London: Macmillan and Co., 1877. [Online]. Available: https://archive.org/details/theorysound06raylgoog.

[69] J. R. S. Rayleigh, *The Theory of Sound, Vol. II*. London: Macmillan and Co., 1896. [Online]. Available: https://archive.org/details/theoryofsound02raylrich.

[70] R. Feynman, R. Leighton, and M. Sands, *The Feynman Lectures on Physics, Vol. I: The New Millennium Edition: Mainly Mechanics, Radiation, and Heat*. New York: Basic Books, 2011. ISBN: 0465024148.

[71] R. Feynman, R. Leighton, and M. Sands, *The Feynman Lectures on Physics,*

Vol II: The New Millennium Edition: Mainly Electromagnetism and Matter. New York: Basic Books, 2011. ISBN: 0465024162.

[72] C. Lanczos, *The Variational Principles of Mechanics*. University of Toronto Press, 2nd ed., 1949. ISBN: 1487581770.

[73] H. L. F. Helmholtz, *On the Sensations of Tone as a Physiological Basis for the Theory of Music*. London: Longmans, Green and Co., 3rd ed., 1895. [Online]. Available: https://archive.org/details/onsensationsofto00helmrich.

[74] C. Truesdell and R. Toupin, *The Classical Field Theories*, pp. 226–858. Berlin, Heidelberg: Springer Berlin Heidelberg, 1960. ISBN: 3642459436, doi: https://doi.org/10.1007/978-3-642-45943-6_2.

[75] C. Truesdell and W. Noll, *The Non-Linear Field Theories of Mechanics*, pp. 1–579. Berlin, Heidelberg: Springer Berlin Heidelberg, 2004. ISBN: 3662103883, doi: https://doi.org/10.1007/978-3-662-10388-3_1.

[76] M. E. Gurtin, E. Fried, and L. Anand, *The Mechanics and Thermodynamics of Continua*. Cambridge: University Press, 2010. ISBN: 0521405980.

[77] P. Chadwick, *Continuum Mechanics: Concise Theory and Problems*. New York: Dover Publications, 1999. ISBN: 0486401804.

[78] G. A. Maugin, *Continuum Mechanics Through the Eighteenth and Nineteenth Centuries: Historical Perspectives from John Bernouilli (1727) to Ernst Hellinger (1914)*. Solid Mechanics and Its Applications, vol. 214, Switzerland: Springer International Pub., 1st ed., 2014. ISBN: 3319053745.

[79] G. A. Holzapfel, *Nonlinear Solid Mechanics: A Continuum Approach for Engineering*. New York: Wiley, 2000. ISBN: 0471823198.

[80] G. Grioli and C. Truesdell, *Non-linear Continuum Theories: Lectrues given at a Summer School of the Centro Internazionale Matematico Estivo (C.I.M.E.) held in Bressanone (Bolzano), Italy, May 31-June 9, 1965*. C.I.M.E. Summer Schools, vol. 36, Berlin, Heidelberg: Springer Berlin Heidelberg, 1st ed., 2011. ISBN: 3642110337.

[81] J. C. Simo and T. J. R. Hughes, *Computational Inelasticity*. Interdisciplinary Applied Mathematics, vol. 7, New York: Springer-Verlag New York, Inc., 1st ed., 1998. ISBN: 0387975209.

[82] N. S. Ottosen and M. Ristinmaa, *The Mechanics of Constitutive Modeling*. London: Elsevier, 2005. ISBN: 008044606X.

[83] E. Lieb and J. Yngvason, "A Guide To Entropy And The Second Law Of Thermodynamics," *Notices of the American Mathematical Society*, vol. 45, pp. 571–581, 06 1998.

[84] P. Grinfeld, *Introduction to Tensor Analysis and the Calculus of Moving Surfaces*. New York: Springer New York, NY, 2013. ISBN: 1461478669.

[85] T. J. R. Hughes, *The Finite Element Method: Linear Static and Dynamic Finite Element Analysis*. New York: Dover Publications, 2000. ISBN: 0486411818.

[86] K.-J. Bathe, *Finite Element Procedures*. New Jersey: Prentice Hall, 1996. ISBN: 0133014584.

[87] O. Zienkiewicz, R. Taylor, and J. Zhu, eds., *The Finite Element Method: Its Basis and Fundamentals*. Oxford: Butterworth-Heinemann, 7th ed., 2013. ISBN: 1856176330.

[88] M. Hori, *Introduction to Computational Earthquake Engineering*. London: Imperial College Press, 2006. ISBN: 1860946216.

[89] B. D. Coleman and M. E. Gurtin, "Thermodynamics with Internal State Variables," *The Journal of Chemical Physics*, vol. 47, no. 2, pp. 597–613, 1967.

[90] M. Planck, *Treatise on Thermodynamics*. London: Longmans, Green and Co., 1903. [Online]. Available: https://archive.org/details/treatiseonthermo00planrich.

[91] I. M. Gelfand and S. V. Fomin, *Calculus of Variations*. New York: Dover Publications, 2000. ISBN: 0486414485.

[92] R. Haberman, *Elementary Applied Partial Differential Equations: With Fourier Series and Boundary Value Problems*. New Jersey: Prentice-Hall, 1983. ISBN: 0132528339.

[93] G. G. Stokes, "On the dynamical theory of diffraction," *Transactions of the Cambridge Philosophical Society*, vol. 9, pp. 1–48, 1849. [Online]. Available: https://archive.org/details/transactionsofca09camb.

[94] D. Komatitsch and J. Tromp, "Introduction to the spectral element method for three-dimensional seismic wave propagation," *Geophysical Journal International*, vol. 139, pp. 806–822, 12 1999.

[95] N. M. Newmark, "A method of computation for structural dynamics," *Journal of the engineering mechanics division*, vol. 85, no. 3, pp. 67–94, 1959.

[96] A. Akinci, D. Cheloni, and A. A. Dindar, "The 30 October 2020, M7.0 Samos Island (Eastern Aegean Sea) Earthquake: effects of source rupture, path and local-site conditions on the observed and simulated ground motions," *Bulletin of Earthquake Engineering*, vol. 19, pp. 4745–4771, 9 2021.

[97] A. Kiratzi, C. Papazachos, A. Özacar, A. Pinar, C. Kkallas, and E. Sopaci, "Characteristics of the 2020 Samos earthquake (Aegean Sea) using seismic data," *Bulletin of Earthquake Engineering*, vol. 19, pp. 4773–4804, 9 2021.

[98] A. Askan, Z. Gülerce, Z. Roumelioti, D. Sotiriadis, N. S. Melis, A. Altindal, B. Akbaş, E. Sopaci, S. Karimzadeh, I. Kalogeras, N. Theodoulidis, K. Konstantinidou, A. A. Özacar, Ö. Kale, and B. Margaris, "The Samos Island (Aegean Sea) M7.0 earthquake: analysis and engineering implications of strong motion data," *Bulletin of Earthquake Engineering*, 11 2021.

[99] K. Makropoulos, G. Kaviris, and V. Kouskouna, "An updated and extended earthquake catalogue for Greece and adjacent areas since 1900," vol. 12, no. 5, pp. 1425–1430, 2012.

[100] S. Stiros, J. Laborel, F. Laborel-Deguen, S. Papageorgiou, J. Evin, and P. Pirazzoli, "Seismic coastal uplift in a region of subsidence: Holocene raised shorelines of Samos Island, Aegean Sea, Greece," *Marine Geology*, vol. 170, no. 1, pp. 41–58, 2000.

[101] N. Ambraseys, *Earthquakes in the Mediterranean and Middle East: A Multidisciplinary Study of Seismicity up to 1900*. Cambridge: University Press, 2009. ISBN: 0521872928.

[102] K. Cetin, G. Mylonakis, A. Sextos, J. Stewart, B. Akbaş, M. Akgün, S. Akkar, M. Aksel, A. Al-Suhaily, A. Altindal, S. Altun, E. Altunel, A. Askan, B. Ay, S. Aydın, A. Baba, E. Eseller-Bayat, B. Binici, E. Çakır, and K. Ziotopoulou, "Seismological and Engineering Effects of the M 7.0 Samos Island (Aegean Sea) Earthquake," tech. rep., 12 2020. doi: 10.18118/G6H088.

[103] D. Komatitsch, J.-P. Vilotte, J. Tromp, J.-P. Ampuero, K. Bai, P. Basini, C. Blitz, E. Bozdag, E. Casarotti, J. Charles, M. Chen, P. Galvez, D. Goddeke, V. Hjorleifsdottir, J. Labarta, N. Le Goff, P. Le Loher, M. Lefebvre, Q. Liu, Y. Luo, A. Maggi, F. Magnoni, R. Martin, R. Matzen, D. McRitchie, M. Meschede, P. Messmer, D. Michea, S. Nadh Somala, T. Nissen-Meyer, D. Peter, M. Rietmann, E. de Andrade, B. Savage, B. Schuberth, A. Sieminski, L. Strand, C. Tape, Z. Xie, and H. Zhu, "SPECFEM3D Cartesian." [software] Downloaded: February 2021, https://geodynamics.org.

[104] Y. Maday and A. T. Patera, "Spectral-element methods for the incompressible Navier-Stokes equations," in *State of the art survey in computational mechanics*, pp. 71–143, 1989. A. K. Noor and J. T. Oden editors.

[105] G. C. Cohen, *High-Order Numerical Methods for Transient Wave Equations*. Scientific Computation, Springer Berlin, Heidelberg, 1st ed., 2002.

[106] M. Ainsworth and H. A. Wajid, "Dispersive and Dissipative Behavior of the Spectral Element Method," *SIAM Journal on Numerical Analysis*, vol. 47, no. 5, pp. 3910–3937, 2009.

[107] D. Komatitsch, "Fluid-solid coupling on a cluster of GPU graphics cards for seismic wave propagation," *C. R. Acad. Sci., Ser. IIb Mec.*, vol. 339, pp. 125–135, 2011.

[108] C. Geuzaine and J.-F. Remacle, "Gmsh: A 3-D Finite Element Mesh Generator with Built-in Pre- and Post-Processing Facilities," *International Journal for Numerical Methods in Engineering*, vol. 79, pp. 1309 – 1331, 09 2009.

[109] Coreform Cubit (Version 2021.5) [software]. OREM, UT: Coreform LLC. Retrieved from https://coreform.com.

[110] R. Clayton and B. Engquist, "Absorbing boundary conditions for acoustic and elastic wave equations," *Bulletin of the seismological society of America*, vol. 67, no. 6, pp. 1529–1540, 1977.

[111] Z. Xie, R. Matzen, P. Cristini, D. Komatitsch, and R. Martin, "A perfectly matched layer for fluid-solid problems: Application to ocean-acoustics simulations with solid ocean bottoms," *The Journal of the Acoustical Society of America*, vol. 140, no. 1, pp. 165–175, 2016.

[112] F. Pellegrini and J. Roman, "Scotch: A software package for static mapping by dual recursive bipartitioning of process and architecture graphs," in *High-Performance Computing and Networking* (H. Liddell, A. Colbrook, B. Hertzberger, and P. Sloot, eds.), (Berlin, Heidelberg), pp. 493–498, Springer Berlin Heidelberg, 1996.

[113] SPECFEM Development Team, *SPECFEM3D Cartesian User Manual Version 3.0*. Computational Infrastructure for Geodynamics (CIG). Downloaded: February 2021, https://geodynamics.org.

[114] A. M. Dziewonski and D. L. Anderson, "Preliminary reference Earth model," *Physics of the Earth and Planetary Interiors*, vol. 25, no. 4, pp. 297–356, 1981.

[115] K. Makra, E. Rovithis, E. Riga, D. Raptakis, and K. Pitilakis, "Amplification features and observed damages in İzmir (Turkey) due to 2020 Samos (Aegean Sea) earthquake: identifying basin effects and design requirements," *Bulletin of Earthquake Engineering*, 10 2021.

[116] Z. Gülerce, B. Akbaş, A. A. Özacar, E. Sopacı, F. M. Önder, B. Uzel, G. Can, E. Cakir, M. Ilgaç, B. Söylemez, N. Saltoğlu, A. Askan, K. O. Cetin, and B. Unutmaz, "Predictive performance of current ground motion models for recorded strong motions in 2020 Samos Earthquake," *Soil Dynamics and Earthquake Engineering*, vol. 152, p. 107053, 2022.

[117] K. O. Cetin, S. Altun, A. Askan, M. Akgün, A. Sezer, C. Kıncal, Özkan Cevdet Özdağ, Y. İpek, B. Unutmaz, Z. Gülerce, A. A. Özacar, M. Ilgaç, G. Can, E. Cakir, B. Söylemez, A. El-Sayeed, M. Zarzour, İrem Bozyiğit, Çağlar Tuna, D. Köksal, S. Karimzadeh, B. Uzel, and E. Karaali, "The site

effects in Izmir Bay of October 30 2020, M7.0 Samos Earthquake," *Soil Dynamics and Earthquake Engineering*, vol. 152, p. 107051, 2022.

[118] S. Karimzadeh, A. Askan, and A. Yakut, "Assessment of Simulated Ground Motions in Earthquake Engineering Practice: A Case Study for Duzce (Turkey)," vol. 174, no. 9, pp. 3589–3607, 2017.